Wrocław University of Technology
Centre of Advanced Materials and Nanotechnology

Materials Science-Poland

Vol. 28 • No. 3 • 2010

Oficyna Wydawnicza Politechniki Wrocławskiej

Materials Science-Poland is an interdisciplinary journal devoted to experimental and theoretical research into the synthesis, structure, properties and applications of materials.

Among the materials of interest are:

- glasses and ceramics
- sol-gel materials
- photoactive materials (including materials for nonlinear optics)
- laser materials
- photonic crystals
- semiconductor micro- and nanostructures
- piezo-, pyro- and ferroelectric materials
- high-T_c superconductors
- magnetic materials
- molecular materials (including polymers) for use in electronics and photonics
- novel solid phases
- other novel and unconventional materials

The broad spectrum of the areas of interest reflects the interdisciplinary nature of materials research. Papers covering the modelling of materials, their synthesis and characterisation, physicochemical aspects of their fabrication, properties and applications are welcome. In addition to regular papers, the journal features issues containing conference papers, as well as special issues on key topics in materials science.

Materials Science-Poland is published under the auspices of the Centre of Advanced Materials and Nanotechnology of the Wrocław University of Technology, in collaboration with the Institute of Low Temperatures and Structural Research of the Polish Academy of Sciences and the Wrocław University of Economics.

All accepted manuscripts are placed on the Web page of the journal and are available at the address: http://MaterialsScience.pwr.wroc.pl

All published papers are placed on the Web page of the journal and are **freely accessible** at the address: http://MaterialsScience.pwr.wroc.pl

Materials Science-Poland is abstracted/indexed in: Chemical Abstracts, Materials Science Citation Index, Science Citation Index Expanded, Scopus.

Editorial Office

Daniel Davies
Marek Łata

Printed in Poland

Drukarnia Oficyny Wydawniczej Politechniki Wrocławskiej
Zam. nr 91/2011.

Materials Science-Poland, *Vol. 28*, *No. 3*, *2010*

Synthesis and properties of magnetic nanoparticles coated with biocompatible compounds

M. RĂCUCIU[1*], D.E. CREANGĂ[2], A. AIRINEI[3], D. CHICEA[1], V. BĂDESCU[4]

[1]Lucian Blaga University, Faculty of Science, Dr.Ratiu Street, No. 5–7, Sibiu, 550024, Romania

[2]Al. I. Cuza University, Faculty of Physics, 11A Blvd. Copou, 700506, Iasi, Romania

[3]P. Poni Institute of Macromolecular Chemistry Iasi, Romania

[4] National Institute of R&D for Technical Physics, 47 Blvd. D. Mangeron, Iasi, Romania

Syntheses and characterization of two types of systems of magnetic nanoparticles functionalized with biocompatible molecules have been presented. Two colloidal suspensions of iron oxide nanoparticles fabricated by the same co-precipitation method were obtained; the nanoparticles with perchloric acid ($HClO_4$) and with citric acid ($C_6H_8O_7$), were coated and dispersed in water. The structure at nanometric level of functionalized magnetic nanoparticles was analyzed, using data obtained from magnetic, rheological and structural measurements. Magnetic properties were discussed based on magnetization measurements. Fourier transform infrared absorption spectra have been recorded to obtain additional information on the composition of functionalized magnetic nanoparticles. To assess the optical properties of highly diluted suspensions, UV-VIS absorbance spectra were recorded. Light scattering anisotropy on functionalized magnetic nanoparticles was investigated as well. The dimensional distribution of the nanoparticles physical diameter was comparatively presented using the box-plot statistical method applied to the data provided by transmission electron microscopy.

Keywords: *magnetic nanoparticles; magnetic properties; TEM analysis; FTIR spectra; UV–VIS absorbance; light scattering anisotropy*

1. Introduction

Colloidal suspensions of magnetic particles have been studied since the early 1900s but interest of scientists increased in the 1960s with the production of stable concentrated suspensions of magnetic nanoparticles [1, 2]. Systems of magnetic nanoparticles led to a significant number of commercial applications [3, 4]. Recent development of a large variety of functionalized magnetic nanoparticles resulted in

*Corresponding author, e-mail: mracuciu@yahoo.com

new biomedical and clinic applications. A major drawback for a lot of applications remains the lack of well-defined and characterized nanoparticles. Growing attention is paid to iron oxide nanoparticles (especially magnetite – Fe_3O_4) embedded in a biocompatible compound. Magnetic fluids consist of colloidal suspensions of ferromagnetic monodomain nanosized particles in various carrier liquids [3]. To avoid agglomeration of magnetic nanoparticles due to attractive van der Waals forces, the particles need to be coated with different complex agents that provide enhanced stability due to steric hidrance or combined electrostatic and steric stabilization. Synthetic and natural polyacids (e.g., dimercaptosuccinic acid, citric acid, tartaric acid, aspartic acid, glutamic acid) are the mostly used coating agents [5–7]. Among various methods for producing magnetic nanoparticles, chemical routes have the advantages of being relatively simple and providing good control over properties of the particles. Water based magnetic fluids hold great potential for biological applications, considering their influence in plant growth [8–11].

2. Experimental

Systems of magnetic nanoparticles were fabricated by alkaline hydrolysis of highly concentrated solutions of Fe^{2+} and Fe^{3+} salts following the preparation protocol proposed in [12]. Solutions of ferric and ferrous salts were prepared in 2 M HCl solvent since the acidic conditions prevent formation of iron hydroxides. 5.0 cm^3 of 2 M stock $FeCl_2$ solution and 20.0 cm^3 of 1 M stock $FeCl_3$ solution were added during magnetic mixing under continuous pouring of 250 cm^3 of 1 M NH_4OH solution.

The suspensions were finally washed with deionized water to reach approximately pH of 6.5. After washing, to the magnetic particles precipitate 5 cm^3 of 25% solution of perchloric acid (PA sample) or citric acid (CA sample) were added, the resulted dark suspension being further stirred for 1 h. The microstructural features of the two aqueous suspensions of the magnetic nanoparticles were analyzed by means of physical tests. The rheological properties such as density, dynamic viscosity and surface tension were measured using standard methods.

To obtain the profile of the nanoparticle dimensions, the magnetic measurements and transmission electron microscopy were chosen as main investigation methods. Using a Tesla device with the resolution of 1.0 nm, the transmission electron microscopy (TEM) images were obtained for 10^4 dilutions in distilled water of the samples, followed by the deposition on collodion sheet. Magnetization and magnetic susceptibility measurements were performed following the Gouy method at constant normal ambient temperature. Magnetic field intensity was measured by means Walker Scientific MG 50D Gaussmeter with a Hall probe and for sample weighting measurement an electronic balance ACULAB-200 with 10^{-4}g accuracy was used.

Infrared absorption spectra (FT-IR) have been recorded aiming to get some information upon the coated magnetic nanoparticles composition, using a Bruker Vertex 70

infrared spectrometer and magnetic nanoparticles dispersions in KBr after previous thermal treatment at 100 °C up to constant weight. To assess the optical properties of the highly diluted suspensions of magnetic nanoparticles, UV-VIS absorbance spectra were recorded with a CINTRA 5 spectrophotometer in a double beam mode, using a 1 cm quartz cell filled against deionized water as a reference solvent.

A typical light scattering procedure, with collimated laser beams was used to detec the far field [13–15], in assessing the light scattering properties of nanoparticles forming magnetic suspensions. A simple experimental setup was assembled, consisting of a He–Ne laser, a cuvette, a sensitive detector, a data acquisition system and a computer. The cuvette-detector distance D was 2.5 m and x was modified gradually, changing the angle accordingly. The detector was a photoresistor and had the dimension d of 5 mm which makes an angular opening of 0.002 rad or 0.1273°. For light scattering anisotropy studies, the initial magnetic nanoparticles suspensions were diluted at the volume ratio of 3.0×10^{-6}, using deionized water right before the light scattering analysis, in order to reduce the magnetic nanoparticles agglomeration rate that actually begins during dilution.

The light intensity that can be measured using a detector is proportional with the integral F of the phase function over the polar angle interval $[\theta_1, \theta_2]$ covered by the detector. The function F was fit on the experimental data using a program written for this purpose. Details of the experimental procedure are presented in [16].

3. Results and discussions

TEM images of PA and CA samples are shown in Fig. 1. The analyses of all TEM measurements resulted in physical diameter distribution histograms (Fig. 2), the mean of particles diameter being given in Table 1.

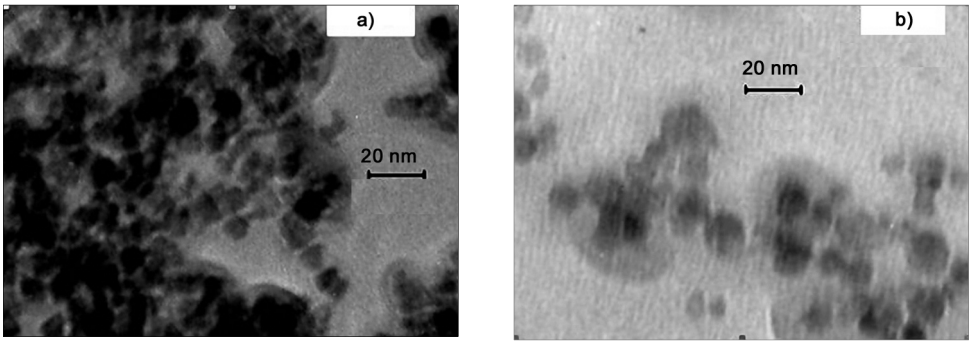

Fig. 1. TEM images of two systems of the functionalized magnetic nanoparticles analyzed in this study: a) CA sample, b) PA sample

Magnetization curves obtained for the functionalized magnetic nanoparticles samples are presented in Fig. 3. Considering the Langevin equation at high field and ex-

trapolating to $1/H = 0$, the magnetization (M) versus $1/H$ curves, the saturation magnetization was obtained. Also, the initial susceptibility χ_0 was determined from the slope of the magnetization versus magnetic filed curves at low field. Using magnetization measurements data and assuming a spherical particle shape, the magnetic diameters (d_M) were calculated according to Langevin's equation. The results are presented in Table 1.

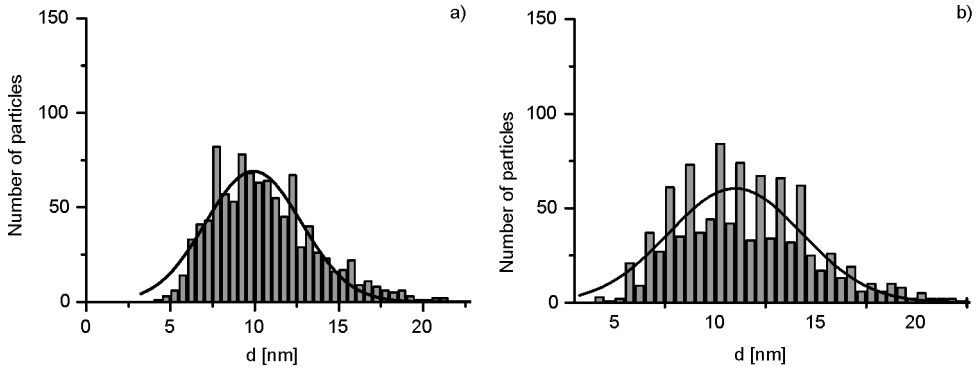

Fig. 2. Histogram of distributions of diameters of functionalized nanoparticles: a) PA, b) CA

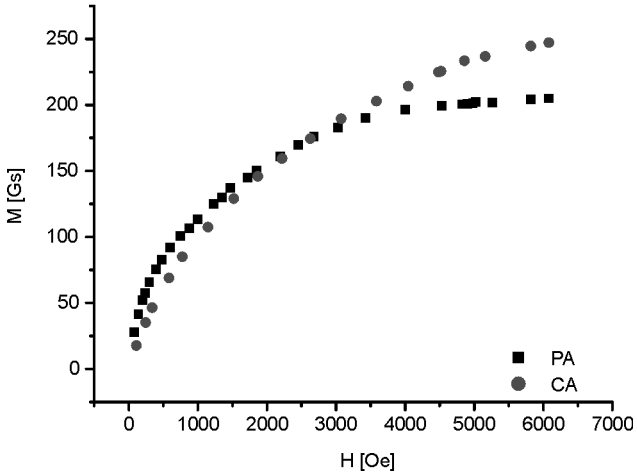

Fig. 3. Magnetization curves of the functionalized magnetic nanoparticles in aqueous suspensions

Table 1. The data for dimensional analysis and magnetic properties

Sample	ΦM [%]	d_{TEM} [nm]	d_M [nm]	M_S [Gs]	χ_0
PA	3.82	10.552	7.112	229.5	0.170
CA	4.67	11.448	6.014	280.5	0.107

Differences evidenced between d_{TEM} and d_M values can be assigned to the surfactant shell of the magnetite core. For these two types of coated magnetic nanoparticles, the thicknesses of the organic surface layers of 1.72 nm in the PA sample and of 2.71 nm in the CA sample have been calculated. Also, we can see that high magnetization value was revealed for the aqueous suspension of magnetic nanoparticles coated with citric acid. The results of measurements of the physical parameters as well as the volume fraction Φ, determined from the density measurements, are presented in Table 2.

Table 2. Rheological properties and volume fraction data

Sample	Φ [%]	Density [kg/m^3]	Surface tension $\times 10^3$ [N/m]	Viscosity $\times 10^3$ kg/(m·s)
PA	4.56	1088	86.7	1.8
CA	5.05	1089	77.1	2.7

Further analysis was carried out based on FTIR spectra (4000 cm^{-1}–500 cm^{-1}). In the magnetic nanoparticles coated with perchloric acid (PA sample) the FTIR spectra show a triple band at 1087 cm^{-1}, 1111 cm^{-1}, 1147 cm^{-1}and a double band at, 626 cm^{-1} and 637 cm^{-1} which confirms the presence of iron perchlorate in the solid phase of the PA coated magnetic nanoparticles system. The narrow but intense absorption of perchlorate ions at about 630 cm^{-1} seems to be overlapped onto weaker vibrations of the iron oxide skeleton situated in the same region.

Also, the 1400 cm^{-1} band could be assigned to the ferrophase complex vibrations. An intense band at 1610 cm^{-1} may be assigned to the deformation vibrations of water molecules trapped onto the magnetite colloidal particles. The low intensity and bifurcated bands at 3599 cm^{-1} and 3435cm^{-1} corresponding to OH symmetrical and asymmetrical stretchings can reveal the presence of free water traces. An intense absorption region beyond 600 cm^{-1} associated with stretching and torsional vibration modes of magnetite can also be seen.

In the CA sample, IR spectrum revealed the bands of iron citrate. An intense band at 3450 cm^{-1} confirms the presence of water traces while the absorption at 3200–3400 cm^{-1} suggests the presence of non-dissociated OH groups of citric acid. At 1600 cm^{-1}, an intense band is visible that may be assigned to the symmetric stretching of OH from COOH group, revealing the binding of a citric acid radical to the magnetite surface. Also, the neighbour band at 1400 cm^{-1} can be assigned to the asymmetric stretching of CO from COOH group. Low-intensity bands between 400 cm^{-1} and 600 cm^{-1} can be associated with stretching and torsional vibration modes of magnetite. Thus, we can say that the citric acid binds chemically to the magnetite surface by carboxylate chemisorptions, citrate ions resulting this way.

To assess the optical properties of highly diluted magnetite nanoparticles suspension (10^{-3} volume fraction), UV-VIS absorbance spectra were recorded on spectrophotometer in a double beam mode, with deionized water as reference solvent (Fig. 4).

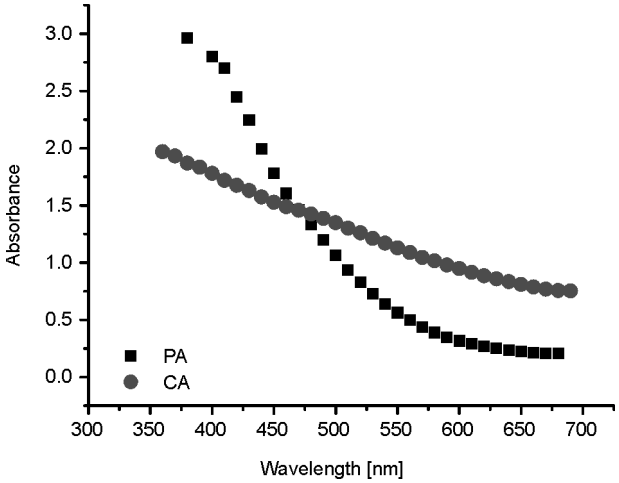

Fig. 4. UV-VIS absorbance spectra of the diluted suspensions of systems of magnetic nanoparticles

The PA sample exhibits an increased absorbance toward shorter wavelengths in comparison to the CA sample, while for longer wavelengths the CA sample exhibits an increased absorbance in comparison to PA sample.

For light scattering anisotropy study, two types of diluted magnetic nanoparticles suspensions (PA and CA) having the volume ratio of 3.0×10^{-6}, hence an optical depth around 1, to avoid multiple scattering, were used. For each sample, the light intensity was measured at various polar angles. The results of the fit that is the C and g values, the anisotropy parameter together with the errors in determining them with respect to the fit are presented in Table 3.

Table 3. The results of the light scattering anisotropy measurement on the magnetic nanoparticles systems analyzed in this study

Sample	Mean size [nm]	C [a.u.]	ΔC [a.u.]	g	Δg
PA	10.552	233.61	0.03	0.99108	10^{-5}
CA	11.448	304.23	0.01	0.98219	5×10^{-6}

Figure 5 presents the plot of the experimental data and of the F function calculated with the C and g values from the fit for CA sample. The light scattering anisotropy parameter was measured for both magnetic nanoparticles suspensions analyzed in this

study. Examining the data in Table 3,I we notice that the anisotropy parameter *g* of PA sample (0.99108) is higher than that for CA sample (0.98219).

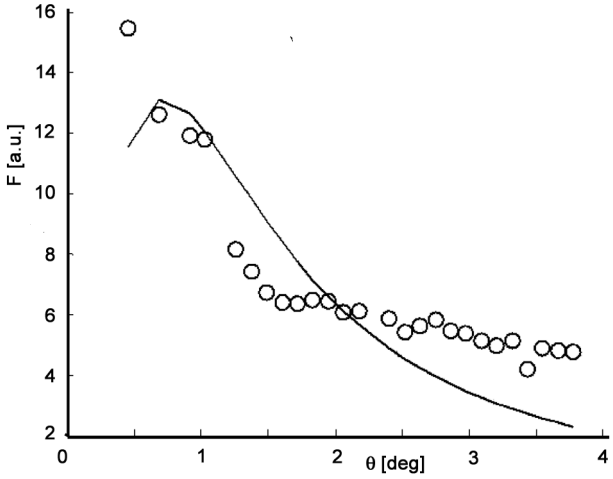

Fig. 5. The plot of the experimental data (circles) and of the calculated *F* function (solid line) for CA sample in function of θ

Considering the significance of the *g* parameter, one can conclude that bigger particles scatter light more isotropic than smaller ones. The size of the scattering centres is smaller than the wavelength and thus the light diffusion may be described by the Rayleigh scattering rather than by the Mie scattering [17, 18]. This might explain the mismatch of the curve to the experimental data. A better match can be found on bigger scattering centers, which can be treated in terms of the Mie scattering, better described by the Henyey Greenstein phase function. In this paper, the experimental results of the light scattering anisotropy have been presented, without any theoretical explanation on the difference in the *g* parameter.

4. Conclusions

Physical characterization of two samples of aqueous suspensions of magnetic nanoparticles stabilized with citric acid (CA) and perchloric acid (PA), synthesized by the same protocols was discussed. The highest viscosity and volume fraction were evidenced for the magnetic nanoparticles coated with citric acid. The high magnetization value and small magnetic diameter of coated nanoparticles were found for the sample based on citric acid coating. The IR spectra confirmed the presence of iron perchlorate in the solid phase of the PA sample and the presence of citric acid at the magnetite surface in the CA samples. The anisotropy parameter *g* of the PA sample was higher than that of the CA sample.

References

[1] PAPEL S.S., US Patent, 3 (1965), 572.
[2] KHALAFALLA S.E., REIMERS G.W., IEEE Trans. Magn., 16 (1980), 178.
[3] ROSENSWEIG R.E., *Ferrohydrodynamics*, Cambridge University Press, New York, 1985.
[4] SCHERER C., FIGUEIREDO NETO A.M., Brazil. J. Phys., 35 (2005), 718.
[5] MENDENHALL G.D., GENG Y., HWANG J., J. Colloid Interface Sci., 184 (1996), 519.
[6] FAUCONNIER N., BÉE A., ROGER J., PONS J.N., J. Molecular Liquids, 83 (1999), 233.
[7] SOUSA M.H., RUBIM J.C., SOBRINHO P.G., TOURINHO F.A., J. Magn. Magn. Mater., 225 (2001), 67.
[8] CORNEANU G.C., CORNEANU M., MARINESCU G., BADEA E., BĂBEANU C., BICA D., COJOCARU L., Abstracts book of 8th Int. Conf. Magn. Fluids, Timisoara, 1998, p. 447.
[9] PAVEL A., TRIFAN M., BARA I.I., CREANGA D.E., COTAE C., J. Magn. Magn. Mater., 201 (1999), 443.
[10] RĂCUCIU M., CREANGĂ D., J. Magn. Magn. Mater., 311 (2007), 288.
[11] RĂCUCIU M., CREANGĂ D., J. Magn. Magn. Mater., 311 (2007), 291.
[12] ENZEL P., ADELMAN N.B., BECKMAN K.J., CAMPBELL D.J., ELLIS A.B., LISENSKY G.C., J. Chem. Educ., 76 (1999), 943.
[13] HAMMER M., SCHWEITZER D., MICHEL B., THAMM E., KOLB A., Appl. Opt., 37 (1998), 7410.
[14] HAMMER M., YAROSLAVSKY A.N., SCHWEITZER D., Phys. Med.Biol., 46 (2001), N65.
[15] STEENBERGEN W., KOLKMAN R., DE MUL F., J. Opt. Soc. Am. A, 16 (1999), 2959.
[16] CHICEA D., RĂCUCIU M., J. Opt. Adv. Mater., 9 (2007), 3843.
[17] GOODMAN J.W., *Series Topics in Applied Physics*, Vol. 9, J.C. Dainty (Ed.), Springer, Berlin, 1984.
[18] BRIERS J.D., Physiol. Meas., 22 (2001), R35.

Received 21 January 2008

Materials Science-Poland, *Vol. 28*, *No. 3*, *2010*

Fast and easy preparation of a novel highly acidic sulfonic-functionalized SBA-1 cubic mesoporous catalyst and its application in the esterification of palmitic acid

A. ABBASI[1], A. R. MAHJOUB[1*], A. R. BADIEI[2]

[1]Dept. of Chem., School of Basic Sciences,Tarbiat Modares University,Tehran, 14115-175, Iran

[2]School of Chemistry, University College of Science, University of Tehran, Tehran, Iran

Propylsulfonic acid-functionalized cubic mesoporous silica was prepared through in situ oxidization of mercaptopropyl groups with H_2O_2 during co-condensation of tetraethyl orthosilicate and 3-mercapto-propyl trimethoxysilane under strong acidic conditions. The materials obtained with 5–20 mol % loadings of sulfonic acid groups had surface areas of up to 1300 m^2/g and pore sizes of around 2.5 nm. Next, the catalytic activity of this material was investigated in esterification of palmitic acid as a compound model in the process of biodiesel production. Methyl ester production by this new nanoporous catalyst shows a very remarkable yield during a mild liquid phase reaction.

Keywords: *cubic mesoporous silica; SBA-1; esterification; biodiesel; palmitic acid*

1. Introduction

The discovery of an ordered M41S family of mesoporous materials has stimulated extensive research, due to the potential use of these materials as prospective catalysts, adsorbents, and templates for the syntheses of nanostructures [1, 2]. To further explore possible applications of these materials, much research work has been devoted to the synthesis of organically hybrid well defined pore structures, highly accessible functional groups, and controlled surface reactivity [3, 4]. Grafting of functional organosilanes by using surface hydroxyl groups as anchor points has been widely used [5, 6].

Generally speaking, it is accepted that a cubic mesostructure is more advantageous for catalytic applications than a hexagonal one, since three dimensional pore arrangements of cubic mesostructures are more resistant to pore blocking and allow faster diffusion of reactants. Therefore, organofunctionalized mesoporous silicas with cubic

*Corresponding author, e-mail: mahjouba@modares.ac.ir

mesostructures would be more desirable than those with hexagonal mesostructures, such as MCM-41. For the first time, Huo et al. [7–9] reported a successful synthesis of SBA-1 (cubic *Pm*3*n*) through the $S^+X^-I^+$ route, where S, X, and I correspond to surfactant, halide, and inorganic species, respectively. In this approach, acidic conditions were imposed, and a surfactant having a large head group, namely cetyltriethylammonium bromide (CTEABr) was used. So far, only a few functionalized SBA-1 mesoporous materials have been reported due to their poor structural stability under hydrothermal conditions. On the other hand, addition of organosilanes in strongly acidic conditions during the direct synthesis of organofunctionalized SBA-1 mesoporous materials is gives better results [10].

Sulfonic functionalized mesoporous materials have received exceptional attention because of their many practical applications, such as heterogeneous acid catalysis, toxic mercury ion trapping, biomolecule immobilization, and as a support material for metallic nanoparticles [11]. Acid catalysts increase the reaction rates of esterification and transesterification processes. Fatty acid methyl esters are products of trans-esterification of vegetable oils and fats with methanol in the presence of an acid or basic catalyst. These products are defined as biodiesels. There is a growing worldwide interest in biofuels as an alternative to diesel fuels, especially in environmentally conscious countries.

Many researchers tried to develop vegetable oil-based derivatives that have properties and performance similar to those of petroleum based diesel fuel. Biodiesel (monoalkyl esters) is one such alternative fuel which is obtained by the transesterification of triglyceride oil with monohydric alcohols. It has been reported that biodiesel obtained from canola and soybean oil is a very good substitute for diesel fuel [12]. Despite its environmental benefits, a high cost of biodiesel production is the major obstacle to its commercialization. The transesterification of waste cooking oil is an effective way to reduce the cost of raw materials and to solve the problem of waste oil disposal. Unlike virgin oils, waste oils contain high quantities of free fatty acids (FFA) and water. Free fatty acid and water can limit the effectiveness of alkali-catalyzed processes. Also free fatty acids react with an alkali catalyst and produce soaps and water. Therefore, saponification not only consumes the catalyst, but the resulting soaps can also cause the formation of emulsions. Both the aforementioned problems make the production of biodiesels more expensive. For this reason, acid catalysts, especially heterogeneous catalysts, have attracted much more attention in regard to esterification reactions and biodiesel production.

This joint study focuses on synthesizing a novel organoacid functionalized mesoporous catalyst with remarkable hydrothermal stability, in order to catalyze the esterification of palmitic acid.

2. Experimental

Template preparation. Cetyltriethylammonium bromide (CTEAB) was prepared by mixing 1-bromohexadecane (98%, Merck) and triethylamine (99%, Merck) in ab-

solute ethanol under reflux conditions for 24 h. The ethanol is then removed with a rotary evaporator until a white, viscous paste is obtained. The resulting gel is recrystallised by a minimum addition of chloroform, and then ethyl acetate, until the whole solid precipitates [13].

Sulfonic acid-functionalized SBA-1 preparation. Sulfonic acid-functionalized mesoporous silica materials were prepared by one-pot co-condensation of tetraethoxysilane (TEOS) and MPTMS in the presence of CTEAB under acidic conditions, along with a direct reaction with H_2O_2 at room temperature. The final molar composition of the initial gel was as follows: TEOS: *y* MPTMS: 0.2 CTEAB: (30–40) HCl: 700 H_2O: (0–2) H_2O_2

In a typical procedure, 8 g of TEOS was first placed in a beaker with 12.5 cm^3 of 12 M HCl and 100 cm^3 of water, and was subsequently hydrolyzed at room temperature under stirring for an appropriate duration. Then, 1.5 g of CTEAB was added to a prehydrolyzed mixture and the stirring was continued. The mixture became a slightly viscous solution; appropriate quantities of MPTMS and aqueous solution of H_2O_2 (30 wt. %) were slowly added to the solution. Stirring of the mixture was maintained at a constant temperature for 3 h. The solution was then transferred to a Teflon lined autoclave for about 1 h at 100 °C, and finally the solid was filtered, washed and dried at 100 °C overnight. The MPTMS/H_2O_2 molar ratio was 1/10, and the MPTMS/(TEOS + MPTMS) ratio was varied from 0 to 0.20, or 0–20%. The resultant samples are referred to as SBA-1-SO_3H-*x*-*T*, where *T* stands for the prehydrolysis time of TEOS in minutes and *x* is the MPTMS/(TEOS + MPTMS) molar percentage.

For example, SBA-1-SO_3H-10-30 represents the sample prepared with TEOS prehydrolysis for 30 min and such that MPTMS/(TEOS + MPTMS) = 10 mol %. For comparison, samples were also prepared without TEOS prehydrolysis. They are labelled as SBA-1-SO_3H-*x*-0. Another sample containing 10 mol % of MPTMS was prepared with TEOS prehydrolysis in the absence of H_2O_2 and is denoted SBA-1-SH -10-*T*. The thiol groups in SBA-1-SH-10-*T* were post-oxidized to sulfonic acid groups with a 15fold excess of aqueous solution of H_2O_2 (30 wt. %) at room temperature for 4 h. The solids were then acidified with aqueous solution of 2M HCl, followed by filtration, washing with water and ethanol, and finally drying at 100 °C. The post-oxidized sample was defined as SBA-1-SO_3H-10-P. A hexagonal MCM-41 sample was synthesized as described in literature [2]. The resultant MCM-41 was functionalized and post-oxidized in the same way, and was named as MCM-41-SO_3H-10-P.

Template extraction. Resultant samples were extracted in a Soxhlet extraction apparatus, with ethanol as the extraction solvent, in order to remove templates. FTIR was used to monitor the removal of templates. All characterizations and catalytic tests confirmed the samples were template-free.

Catalyst characterization. N_2 sorption isotherms were measured using a Belsorp-18 (Bel Japan Inc.,) at liquid nitrogen temperature. Before taking the measurements,

the samples were degassed at 150 °C for 4 h. The specific surface areas were evaluated using the Brunauer–Emmett–Teller (BET) method in the p/p_0 range of 0.05–0.3. Pore size distribution curves were calculated from the adsorption branch of the isotherms and by applying the Barrett–Joyner–Halenda (BJH) method. The pore volume was taken at the $p/p_0 = 0.990$ point. X-ray powder diffraction (XRD) patterns were obtained on a Philips X'Pert diffractometer using CuK_α radiation (1.5418 Å).

Thermogravimetric (TG) analyses were carried out on a Shimadzu DTG 60 thermogravimetric analyzer with the heating rate of 10 °C/min in an air flow of 50 cm^3/min. Fourier transform infrared (FTIR) spectra were taken on a Bruker Equinox 55 spectrometer, with the resolution of 2 cm^{-1}, using the KBr method. The content of sulfonic acid centres in the materials was determined by ion-exchange with sodium cations followed by acid titration [11]. Aqueous solutions of sodium chloride (NaCl, 2 M) were used as the exchange agents. In a typical experiment, 0.20 g of solid, treated at 150 °C for 5 h, was added to 20 cm^3 of aqueous solution containing the corresponding salt. The resultant suspension was equilibrated for 4 h, then filtered and washed with a small amount of water. Finally, the filtrate was titrated potentiometrically by dropwise addition of aqueous solution of 0.01 M NaOH.

Catalytic reactions. The catalysts were heat treated at 200 °C for 6 h in order to remove adsorbed water in the materials. Then, esterification of palmitic acid with methanol was carried out in a two-necked flask of 50 cm^3 with a reflux condenser placed in a hot plate with a magnetic stirrer. In a typical experiment, 0.02 mol of palmitic acid and 0.2 mol of methanol were mixed under vigorous stirring and heated to 50 °C. Then, 0.1 g of the treated catalyst was added into the reaction mixture. Reaction rates were determined during the reaction intervals. Quantitative analysis was based on the methyl ester products and the corresponding standard methyl palmitate (from Supelco). In all cases, the liquid products were extracted from the reaction mixture at appropriate reaction intervals with a filtering syringe, and analyzed using a Agilent 5890 gas chromatograph (GC) equipped with a 30 m × 0.53 mm HP-5 capillary column and an FID detector.

3. Results and discussion

Powder X-ray diffraction analyses were performed on all the MPTMS functionalized materials. The X-ray diffraction patterns of functionalized SBA-1 samples contain three reflections, which correspond to the (200), (210), and (211) reflections belonging to the space group *pm*3*n*: such patterns are characteristic of materials having ordered cubic arrays of a cage-like channel structure (illustrated in Fig. 1).

N_2 adsorption-desorption isotherms of the sulfonic acid functionalized materials are shown in Fig. 2. The samples prepared with prehydrolysis of TEOS exhibit characteristic type IV isotherms with apparent hysteresis loops, which are typical of

mesoporous materials, according to the IUPAC classification. Pore diameter increases with the prehydrolysis time in the initial gel.

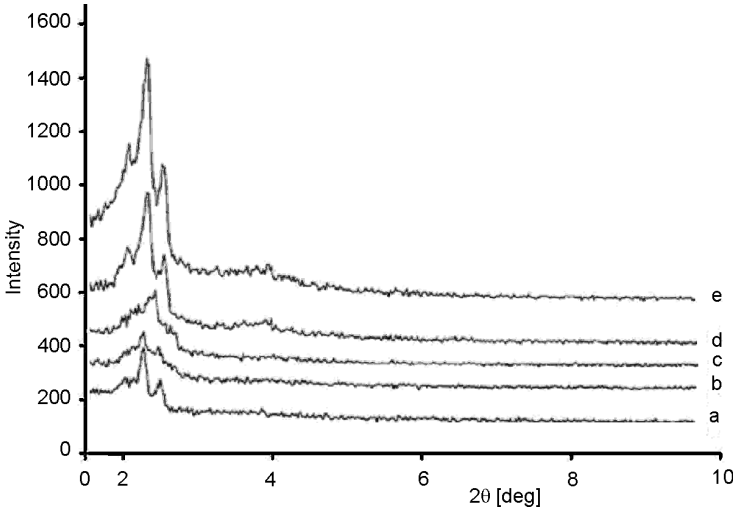

Fig. 1. XRD patterns of template extracted of: a) SBA-1-SO_3H-10-0, b) SBA-1-SO_3H-15-0, c) SBA-1-SO_3H-20-0, d) SBA-1-SO_3H-10-30, e) SBA-1-SO_3H-10-60

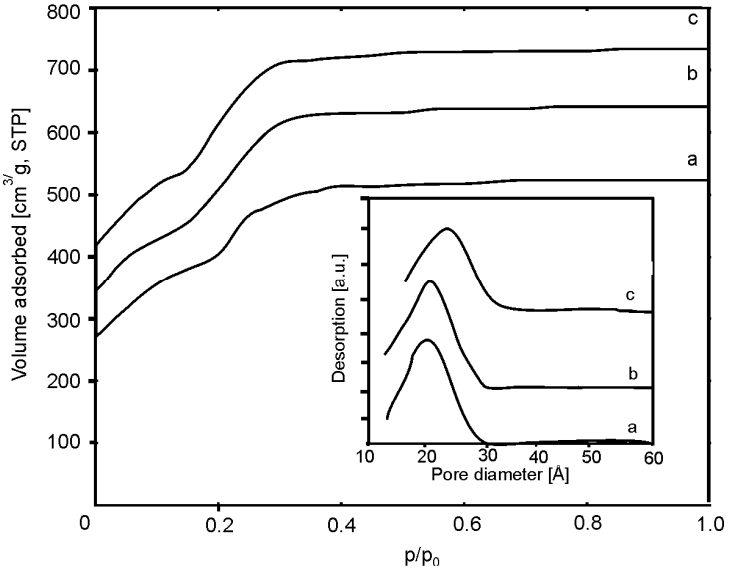

Fig. 2. N_2 adsorption isotherms of: a) SBA-1-SO_3H-10-0, b) SBA-1-SO_3H-10-30 and c) SBA-1-SO_3H-10-60

Basic physicochemical and textural properties of the functionalized materials are presented in Table 1. A_{BET} is the BET surface area, V_p – total pore volume and D_p

– the BJH pore size All samples prepared by co-condensation of TEOS and MPTMS show high surface areas and the BJH pore sizes are around 2.1–2.5 nm. The surface area and the pore volume decrease as the MPTMS content is increased from 5 to 20 mol % in the synthesis mixture. Conversely, the samples prepared without TEOS prehydrolysis exhibit lower surface areas, smaller pore volumes, and smaller average pore sizes than their counterparts synthesized with TEOS prehydrolysis.

Table 1. Textural properties of silica materials

Sample	A_{BET}[1] [m^2/g]	V_p[2] [cm^3/g]	D_p[3] [nm]
SBA-1-SO_3H-10-30	1140	1.06	2.2
SBA-1-SO_3H-10-60	1170	0.97	2.3
SBA-1-SO_3H-10-180	1290	1.14	2.5
SBA-1-SO_3H-10-0	1050	0.95	2.1
SBA-1-SO_3H-10-PO	1018	0.98	2.1
SBA-1-SO_3H-5-0	1103	0.99	2.1
SBA-1-SO_3H-15-0	1037	0.85	2.1

The sulfur content in the MPTMS functionalized materials was analyzed by TG and elemental analyses (EA), and the results are given in Table 2. It can be seen that MPTMS in the initial mixture was mostly incorporated into the silica materials. The acid capacities of the materials prepared in the presence of H_2O_2 increased with the MPTMS content in the initial mixture. The numerical values for the acid capacity are very close to those obtained from EA or TG analyses which is further confirmation that complete oxidation of thiol groups had occurred. By contrast, the SBA-1-SO_3H -10-P sample obtained by post-oxidation shows lower values for acid capacity than those obtained from EA or TG analyses: this is attributed to incomplete oxidation of the thiol groups.

Table 2. Sulfur contents and acid capacities of functionalized SBA-1 materials with MPTMS

Sample	S content [mmol/g]			Acid capacity [mmol/g]
	Calc	by EA	by TG	
SBA-1-SO_3H-10-30	1.4	1.28	1.30	1.2
SBA-1-SO_3H-10-60	1.4	1.32	1.30	1.21
SBA-1-SO_3H-10-180	1.4	1.32	1.33	1.25
SBA-1-SO_3H-10-0	1.4	1.20	1.13	1.10
SBA-1-SO_3H-10-PO	1.4	1.10	1.11	0.91
SBA-1-SO_3H-5-0	0.75	0.77	0.58	0.68
SBA-1-SO_3H-15-0	1.9	1.5	1.45	1.3

Esterification of palmitic acid with methanol was used to test the catalytic activities of propylsulfonic acid functionalized catalyst in liquid phase reactions expressed

by ester yield. The catalytic performance of the SBA-1-SO_3H-10-60 catalyst during esterification at 50 °C, expressed as a function of the reaction time, is shown in Fig. 3. The methyl ester content increases very rapidly and almost linearly with the reaction time in the first 150 min. Then, the reaction rate slows down as the reaction time prolongs. After 4 h, a conversion of around 85% is obtained.

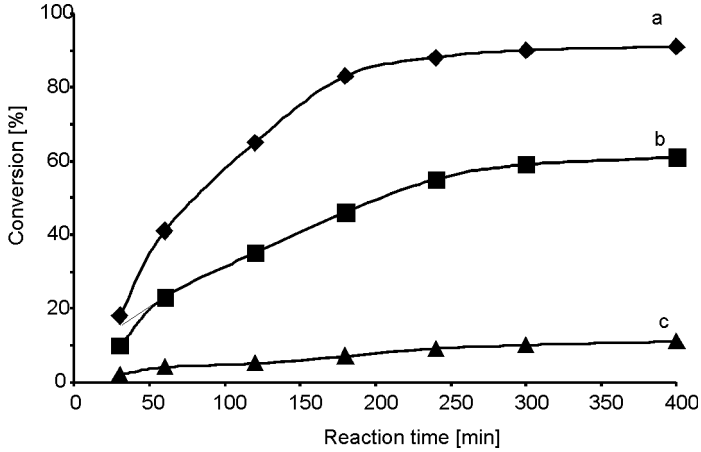

Fig. 3. Catalytic esterification of palmitic acid with methanol in function of reaction time at 50 °C over sulfonic acid-functionalized silica SBA-1 (a), in comparison to the results over MCM-41-SO_3H-10-P (b) and pure silica (c)

Figure 3 also shows that esterification in a homogeneous system without solid catalysts or over pure silica was very weak. Even after 4 h, conversion was lower than 10%. The catalytic activity of MCM-41-SO_3H-10-P is also shown in Fig. 3. As one can see, the acidified cubic SBA-1 catalyst delivers better activity in comparison with hexagonal MCM-41.

4. Conclusions

Novel functionalized cubic SBA-1 silica materials with various loadings of propylsulfonic acid groups were fabricated by a simple co-condensation of TEOS and MPTMS under acidic conditions at room temperature. Samples prepared with TEOS prehydrolysis showed higher surface areas and pore volumes than those prepared without TEOS prehydrolysis. Thiol groups could be completely in situ oxidized into sulfonic acid groups in the synthesis procedure, when H_2O_2 was also added in the synthesis mixture.

Esterification of palmitic acid with methanol was used to confirm and quantify catalytic activity. This catalytic reaction opens up a new synthesis route which facilitates use of inexpensive waste oils, having high free fatty acid contents, for the pro-

duction of biofuels in mild conditions. Furthermore, the yield is high in comparison with conventional base catalysts.

Acknowledgement

Thanks are expressed to the Tarbiat Modarres University for providing financial support for the research.

References

[1] KRESGE C.T., LEONOWICZ M.E., ROTH W.J., VARTULI J.C., BECK J.S., Nature, 359 (1992), 710.
[2] BECK J.S., VARTULI J.C., ROTH W.J., LEONOWICZ M.E., KRESGE C.T., SCHMITT K.D., CHU C.T., OLSON D.H., SHEPPARD E.W., MCCULLEN S.B., HIGGINS J.B., SHLENKER J.L., J. Am. Chem. Soc., 114 (1992), 10834.
[3] SHIN H.J., RYOO R., LIU Z., TERASAKI O., J. Am. Chem. Soc., 123 (2001), 1246.
[4] YANG C.M., LIU P.H., HO Y.FO., CHIU C.Y., CHAO K.J., Chem. Mater., 15 (2003), 275.
[5] STEIN A., MELDE B.J., SCHRODEN R.C., Adv. Mater., 12 (2000), 1403 and references therein.
[6] WRIGHT A.P., DAVIS M.E., Chem. Rev., 102 (2002), 3589.
[7] HUO Q., MARGOLESE D.I., CIESLA U., DEMUTH D.G., FENG P., GIER T.E., SIEGER P., FIROUZI A., CHMELKA B.F., SCHUTH F., STUCKY G.D., Chem. Mater., 6 (1994), 1176.
[8] HUO Q., LEON R., PETROFF P.M., STUCKY G.D., Science, 268 (1995), 1324.
[9] HUO Q., MARGOLESE D.I., STUCKY G.D., Chem. Mater., 8 (1996), 1147.
[10] KAO M., WU J.D., CHENG C.C., CHIANG A.S.T., Microporous Mesoporous Mater., 88 (2006), 319.
[11] MARGOLESE D., MELERO J.A., CHRISTIANSEN S.C., CHMELKA B.F., STUCKY G.D., Chem. Mater., 12 (2000), 2448.
[12] FREEDMAN B., BUTTERFIELD R.O., PRYDE E.H., J. Am. Oil Chem. Soc., 63 (1986), 1375.
[13] KIM M.J., RYOO R., Chem. Mater., 11 (1999), 487.

Received 27 January 2008
Revised 19 March 2008

Materials Science-Poland, *Vol. 28*, *No. 3*, *2010*

A study on the synthesis, characterization and photocatalytic activity of TiO_2 derived nanostructures

B. ZIELIŃSKA*, E. BOROWIAK-PALEN, R. J. KALENCZUK

Institute of Chemical and Environment Engineering, West Pomeranian University of Technology, Szczecin, Pułaskiego 10, 70-322, Szczecin, Poland

Syntheses of TiO_2 derived nanostructures have been conducted at 210 °C by hydrothermal reaction of commercial TiO_2-P25 (Degussa, Germany) in 10 M NaOH aqueous solution. High purity of the as-produced material was confirmed by scanning and transmission electron microscope analyses. The crystallographic structure, as well as the optical and vibronic properties of this material were examined by X-ray diffraction, diffuse reflectance (DR) UV-Vis, resonance Raman spectroscopic methods, respectively. Detailed analysis of the phase composition revealed that the rod-like structures are made up of sodium tetratitanate ($Na_2Ti_4O_9$). It was also observed that acid treatment of the material (hydrothermal reaction) led to a decrease in the diameters of the nanorods. Finally, the photocatalytic activity of the investigated nanostructures was examined, by observing the reaction photocatalytic decolourisation of two organic dyes (Reactive Red 198 and Reactive Black 5) under UV-light irradiation.

Keywords: *nanostructures; oxides; chemical synthesis;*

1. Introduction

Over recent decades, syntheses and characterization of one-dimensional (1D) nanostructures such as nanotubes, nanorods and nanofibres have received significant attention, due to their unusual physical and chemical properties and wide range of potential applications [1–3]. The most outstanding example of a 1D nanostructure is the carbon nanotube [4–6]. However, other one dimensional nanomaterials including metals, oxides or nitrides have also been intensively studied [3, 7–10]. It was noticed that 1D oxidic nanostructures can offer many remarkable advantages which lead to new technological applications, particularly in nanoelectronics and nanophotonics [11].

*Corresponding author, e-mail: bzielinska@zut.edu.pl

Among 1D oxidic nanomaterials, TiO_2 is one of the most interesting. Recently, a large number of synthesis experiments of TiO_2 derived nanotubes, nanorods and nanowires have been reported. Various methods for preparation of those materials have been tested such as combining sol-gel processing with electrophoretic deposition, spin-on processes, anodic oxidative hydrolysis, sonochemical synthesis and pyrolysis routes [12–14]. Nevertheless, one of the most promising and simple methods for synthesizing TiO_2 derived nanostructures is hydrothermal treatment of titania powders of various crystallographic structures (rutile, anatase, and brookite) in a strongly alkaline aqueous solution of NaOH. These methods do not require any templates and the obtained nanostructures have smaller diameter of ca. 10 nm, and high crystallinity [15, 16]. At first, TiO_2-derived nanotubes with a diameter of about 8 nm were obtained by hydrothermal treatment of rutile powders in 10 M NaOH solution at 110 °C [15].

In spite of many studies on the structures and proposed formation mechanisms of the products of the alkaline hydrothermal treatment, it is still a controversial and constantly debated topic among the research community. At first, it was believed that the products of the hydrothermal synthesis with NaOH are nanotubes and nanorods of anatase [1–15]. Afterwards, it was reported that nanotubes of $H_2Ti_3O_7$ are formed and that NaOH acts only as a catalyst [17]. Later, Yang et al. [18] found that the produced nanotubes are $Na_2Ti_2O_4(OH)_2$ but not TiO_2. Next, Sun et al. [19] argued that TiO_2 derived nanotubes are titanates of $Na_xH_{2-x}Ti_3O_7$ type. Additionally, it was also reported that thermal behaviour of TiO_2 derived nanotubes and nanorods are different. Such nanotubes are usually unstable at higher temperatures (above 500 °C) and break down into anatase particles, whereas nanorods converted to the metastable TiO_2 B phase keep their morphology [20, 21].

In the present study, TiO_2-derived nanostructures were produced by a hydrothermal reaction using 10M NaOH aqueous solution and TiO_2-P25 (Degussa, Germany) as precursors. The reaction was carried out at 210 °C. Crystallographic composition, optical and vibronic properties of the product were also investigated. Furthermore, the effect of acid treatment on the morphology of the material was investigated. Finally, the photocatalytic activity of the investigated nanostructures was examined, by observing the photocatalytic decolourisation of two organic dyes (Reactive Red 198 and Reactive Black 5) under UV-light irradiation.

2. Experimental

Materials. Commercial titanium dioxide with a crystalline structure of ca. 20% rutile and ca. 80% anatase and primary particle size of ca. 25 nm (TiO_2–P25, Degussa, Germany) and sodium hydroxide (NaOH, Sigma-Aldrich) were used as the starting materials for the synthesis of the TiO_2-derived nanostructures.

Reactive Red 198 (RR198) and Reactive Black 5 (RB5), produced by Boruta Color Company (Poland), were chosen as the model contaminants for the photocatalytic

decolourisation tests for the produced materials. RR198 and RB5 are water soluble azodyes. Their molecular formulae are presented in Fig. 1. Both dyes exhibit absorption maxima in the spectral range of visible light (RR198-518 nm and RB5-597 nm). Moreover, the light resistances of RR198 and RB5 are 4–5 (ISO Blue Wool Scale). This parameter was estimated by the Boruta Color company, and it is defined according to an eight-unit scale, and corresponds to the amount of dye present in a final product.

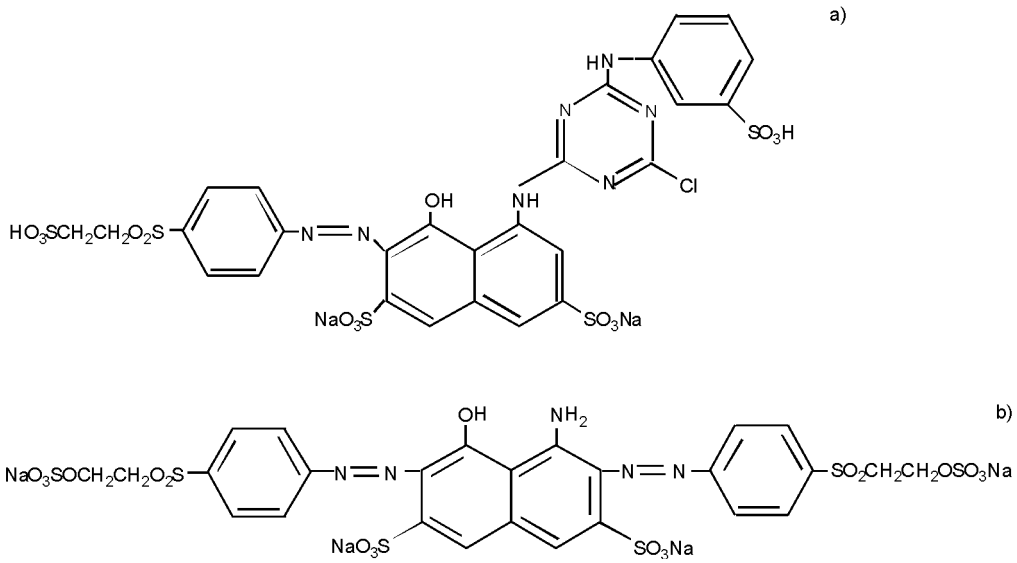

Fig. 1. The molecular formulas of RR198 (a) and RB5 (b)

Preparation of TiO_2 derived nanomaterials. As the first step in the preparation of the nanostructured materials, TiO_2-P25 (2 g) was added to 10 M NaOH aqueous solution (50 cm^3). Afterwards, the as-obtained mixture was kept at 210 °C in a 70 cm^3 autoclave. The annealing time was fixed at 24 h, throughout which the required temperature was maintained. Subsequently, the product of the hydrothermal reaction was washed with distilled water until the pH of the supernatant reached the value of 7. Next, one batch of the obtained powder was collected and dried at 70 °C for 24 h. The sample prepared in the manner described above shall henceforth be referred to, and was labelled as S1. The remaining powder was treated with 0.1 M HCl aqueous solution and was dispersed in an ultrasound bath. Afterwards, this batch was treated repeatedly with distilled water until pH of the supernatant was about 7. Finally, it was dried at 70 °C for 24 h. That sample shall henceforth be referred to, and was labelled as S2.

Experimental procedures and techniques. The morphology of the prepared samples was observed via scanning electron microscopy (SEM, DSM 962, Zeiss, Germany). The crystalline structures of the samples were characterized by X-ray diffrac-

tion (XRD) analysis (X'Pert PRO Philips diffractometer) using a CoK_α radiation. The optical properties of the materials were investigated by means of the diffuse reflectance (DR) UV-Vis technique, using a Jasco (Japan) spectrometer. Additionally, the vibronic properties of the photocatalysts were examined based on their FTIR response. The measurements were performed using a Jasco FTIR 430 (Japan) spectrometer equipped with a diffuse reflectance accessory (Harrick, USA). Resonance Raman analysis was performed using a resonance Renishaw Raman inVia microscope with the laser radiation of the wavelength of 785 nm. And finally, the BET surface areas and mean pore diameters of the catalysts were measured by nitrogen gas adsorption using a Micrometrics ASAP 2010 apparatus.

Determination of photocatalytic activity. The photocatalytic activity of the prepared nanostructure materials was examined by observing the decolourization of the organic dyes when they undergo photocatalytic reaction. The photocatalytic reactions were carried out in an open glass reactor containing 20 cm^3 of a model solution of RR198 or RB5 (initial concentration: 30 mg/dm^3) and 10 mg of the produced materials. At first, the solution was mixed in an ultrasonic bath for half an hour. The solution was subsequently irradiated for 2 h using an 60 W lamp. Next, it was filtered through a 0.45 μm membrane filter. The changes in the concentrations of the dyes were measured using a UV-vis spectrophotometer (Jasco V-530, Japan) at fixed wavelengths of 518 nm (RR198) and 597 nm (RB5).

3. Results and discussion

3.1. Characteristics of the produced materials

Figure 2 shows the SEM images, at two different levels of magnification, of the raw material (pristine TiO_2-P25, images a), b)), and the S1 and S2 samples (images c)–f)). The pristine TiO_2-P25 sample consists of granular crystals with an average diameter of about 25 nm. As is clearly observed, the morphologies of the S1 and S2 samples are clearly different from that of the TiO_2-P25 sample. The S1 sample is composed of rod-like structures. The S2 sample exhibits a similar morphology. It is clearly observed that the mean diameter of S2 nanoparticles is smaller than that of S1 nanoparticles. The rod length distributions of the samples are shown as histograms in Fig. 3: histogram a corresponds to the S1 sample, and histogram b corresponds to the S2 sample. It can be seen that the length of the rods ranges from 1.2 μm to 5.3 μm and from 1.7 μm to 3.2 μm for S1 and S2, respectively. This suggests that acid treatment of S1 leads to an overall reduction in the rod lengths.

The morphology of S2 was studied in greater detail using TEM (data not shown here). One can observe that the S2 sample consists of nanorod particles having an average diameter of 35 nm (ranging from 20 nm to 50 nm). Additionally, the produced nanorods are basically layer-structured, with the layer spacing of 0.96 nm. This value

is higher than those obtained by Meg (0.67 nm) [22], Pavasupree and Yu (0.80 nm) [20, 2] or Tahir (0.32 nm) [24].

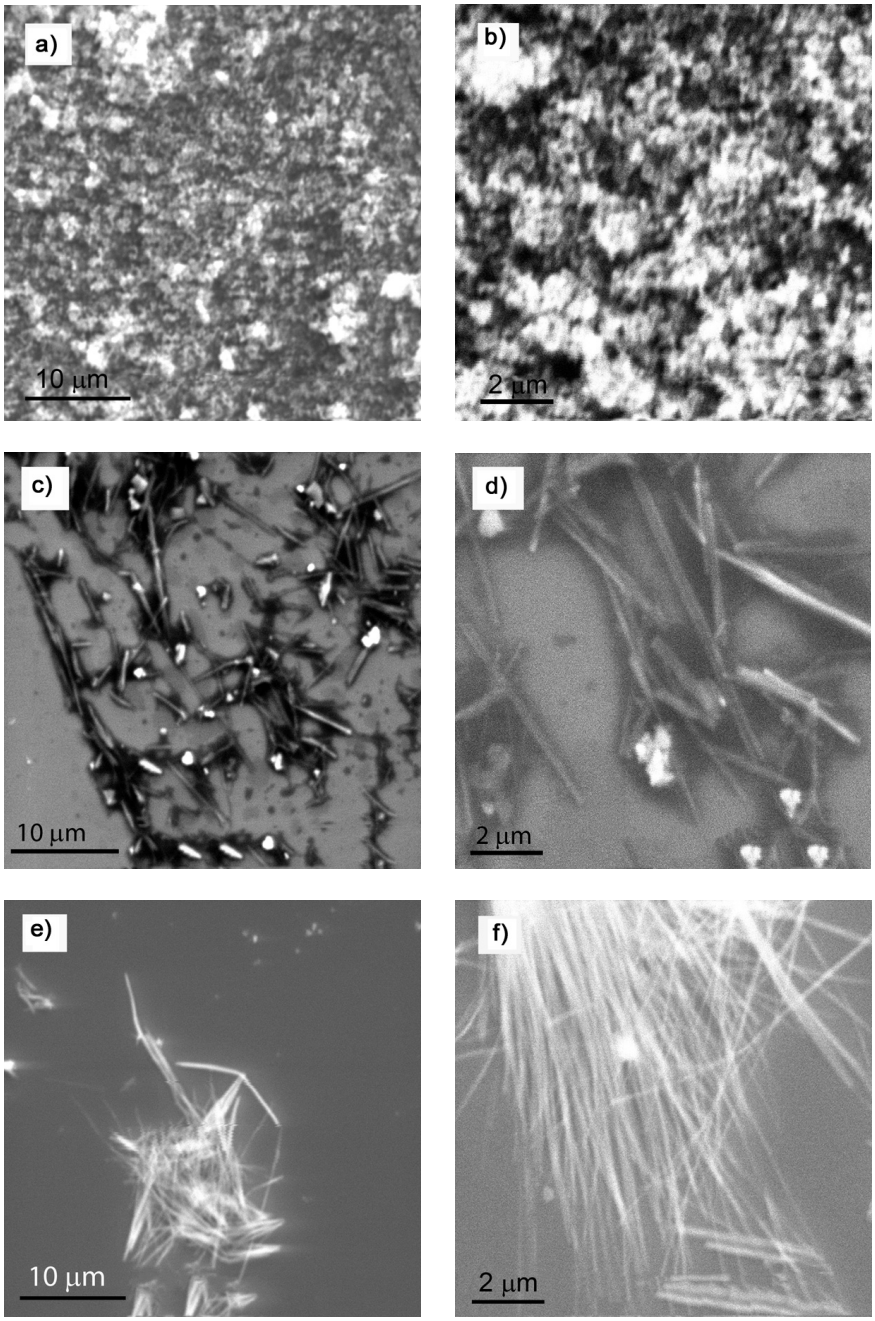

Fig. 2. SEM images of: pristine TiO_2-P25 (a, b), S1 (c, d) and S2 (e, f)

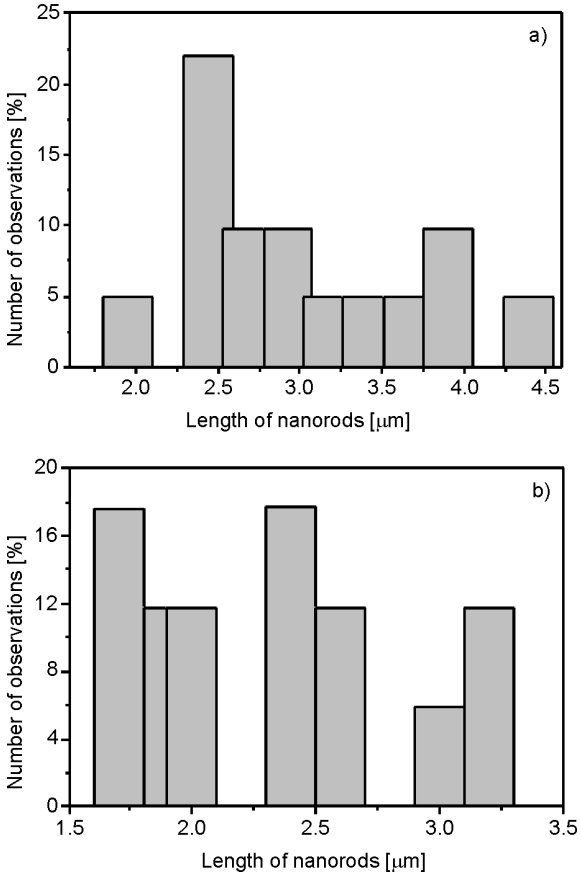

Fig. 3. Distribution of nanorods' lengths: a) S1 and b) S2

The XRD pattern of the pristine TiO_2-P25 sample is presented in Fig. 4a. TiO_2-P25 is a mixture of two different forms of titanium dioxide, such as anatase (marked by the symbol ●, JCPDS card No. 21-1272) and rutile (marked by the symbol ■, JCPDS card No. 34-180). For comparison, Fig. 4b presents the XRD patterns of the samples produced after the hydrothermal reaction and after acid treatment (patterns: 1 – S1, 2 – S2). Detailed phase analysis reveals that S1 is composed of sodium tetra-titanate ($Na_2Ti_4O_9$ marked in Fig. 4b by the symbol ▲, JCPDS card No. 33-1294). One can also observe that S2 (pattern b) is a mixture of sodium titanate (Na_2TiO_3 marked by the symbol ♦, JCPDS card No. 11-0291) and hydrogen pentatitanate ($H_2Ti_5O_{11}\cdot H_2O$ – marked by the symbol ∗, JCPDS card No. 00-044-0131). It is known that K^+ or Na^+ ions in tetratitanates (such as $K_2Ti_4O_9$ or $Na_2Ti_4O_9$) can be exchanged by H^+ ions in HCl aqueous solutions [2]. Therefore, the resulting sample contains hydrogen tetra-titanate $H_2Ti_4O_9$. Here, the interesting point is that during the acid treatment of S1, only partial substitution of sodium by hydrogen atoms, forming $H_2Ti_5O_{11}\cdot H_2O$ occurred. The formation of the additional form of sodium titanate (Na_2TiO_3) is detected.

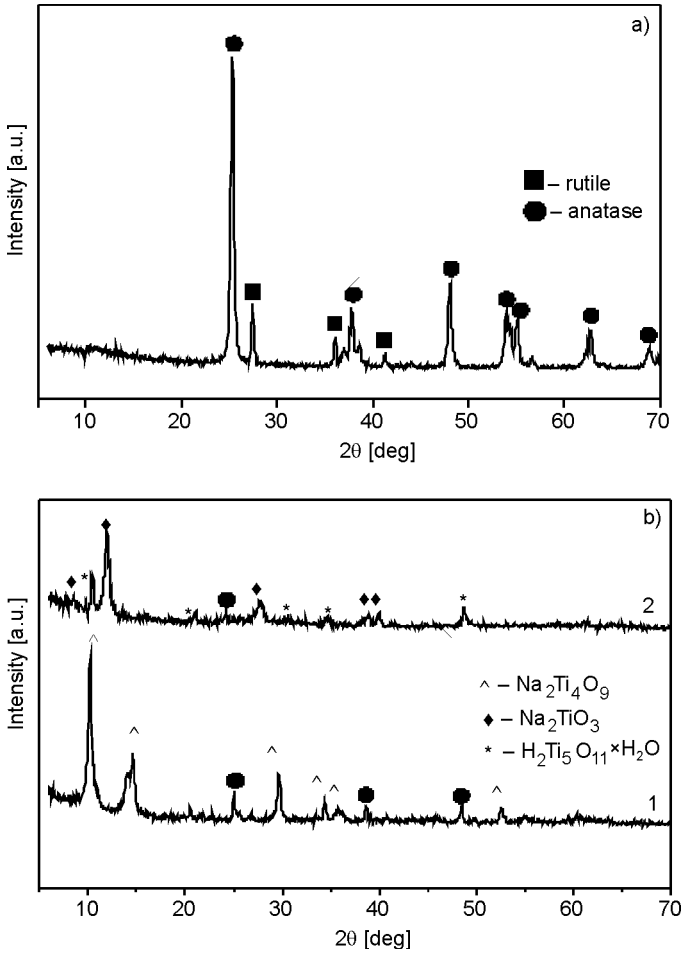

Fig. 4. Diffractograms of the materials: a) pristine TiO_2-P25, b) S1 and S2

The question of what product materials result when NaOH undergoes hydrothermal reaction with different titanium dioxide precursors is the subject of intensive discussions. In many papers, authors argued that TiO_2-derived nanotubes and nanorods are composed of sodium trititanate ($Na_2Ti_3O_7$) and hydrogen trititanate ($H_2Ti_3O_7$) [21, 25, 26]. It is worth pointing out that the nanorod structures of sodium tetratitanate ($Na_2Ti_4O_9$) and hydrogen pentatitanate ($H_2Ti_5O_{11}$), as the main products of hydrothermal reaction of titanium dioxide in NaOH solution have not been described much in the state-of-the-art literature. Furthermore, the presence of anatase phase of TiO_2 can be observed in the diffraction peaks of both the S1 and the S2 samples. It indicates that a small amount of an anatase-type of TiO_2 still remains in the product materials.

Figure 5 shows the FTIR spectra of the pristine TiO_2-P25 sample (spectrum a) and the samples produced after hydrothermal reaction and acid treatment (spectra: b-S1, c-S2).

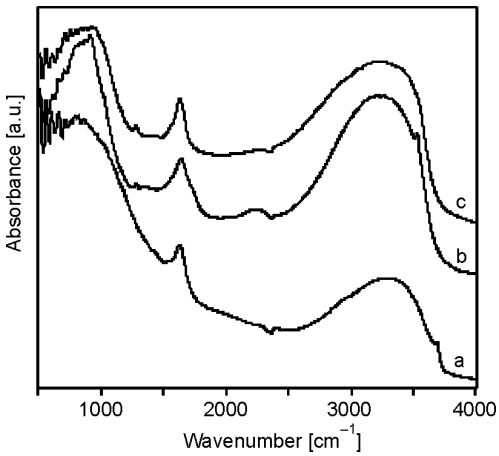

Fig. 5. The FTIR/DRS spectra of: a) pristine TiO_2-P25, b) S1 and c) S2

Absorption bands at about 1000 cm^{-1}, 1640 cm^{-1}, and a very broad band in the 3600–2600 cm^{-1} range were detected in the FTIR spectrum of pristine TiO_2-P25. The band at 1000 cm^{-1} corresponds to the stretching and bending vibrations of Ti–O–Ti bonds [27]. The vibration modes at 1640 cm^{-1} and in the 3600–2600 cm^{-1} range are assigned to the binding vibration of H–O–H and the O–H stretching vibration of the physically adsorbed water [27, 28]. Additionally, here one can notice that the intensities of the bands at 1640 cm^{-1} and 3600–2600 cm^{-1} in the FTIR spectra of S1 and S2 are enhanced with respect to the pristine TiO_2-P25. This indicates that a large amount of adsorbed water remains on the sample surfaces. Moreover, in the case of those two samples, a new absorption band at 1280 cm^{-1} was observed. It is also of note that, for the S1 sample, a new broad band was detected in the 2040–2380 cm^{-1} range.

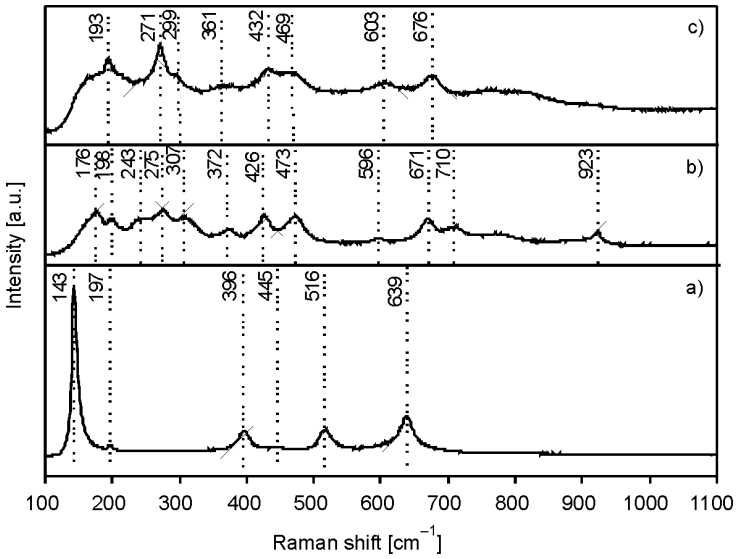

Fig. 6. Raman spectra of: a) pristine TiO_2-P25, b) S1 and c) S2

Figure 6 shows the resonance Raman spectra of the pristine TiO_2-P25 (spectrum a) and produced samples (spectra: S1 – b, S2 – c). It is clearly seen that the spectrum of the TiO_2-P25 shows six peaks at 143, 197, 396, 445 (of very small intensity), and at 516 and 639 cm^{-1}. According to the reference [29, 30], anatase phase of TiO_2 has six Raman active modes ($A_{1g} + 2B_{1g} + 3E_g$) at 147, 198, 398, 515, 640 and 796 cm^{-1}, while rutile has four active modes ($A_{1g} + B_{1g} + B_{2g} + E_g$) situated at 144, 448, 612 and 827 cm^{-1}, respectively. TiO_2-P25, as a mixture of anatase (80%) and rutile (20%), has five Raman peaks (at 143, 197, 396, 516 and 639 cm^{-1}) corresponding to anatase, but just one peak, at 445 cm^{-1}, corresponding to rutile [30].

Additionally, in Figure 6 it is clearly observed that the Raman spectra of S1 and S2 are different from the spectrum of pristine TiO_2-P25. Raman peaks observed for the S1 and S2 nanorods are quite similar to those that have been described before [12, 31]. Moreover, S1 and S2 samples exhibit relatively weak Raman modes in comparison with TiO_2-P25. This observation can be explained by poor crystallinity of the obtained nanorods. In the case of the S1 sample, bands at approximately 176, 198, 243, 275, 307, 372, 426, 473, 596, 671, 710 and 923 cm^{-1} are observed. The Raman modes, at about 176, 198 cm^{-1} and those in the 224–339 cm^{-1} range (namely at 243, 275, and 307 cm^{-1}) are assigned to the stretching modes of Ti–O–Na [12]. The split peaks in the 396–504 cm^{-1} region and the peak at 596 cm^{-1} correspond to the bending and stretching vibration of Ti–O bonds. Moreover, the peak at about 923 cm^{-1} is also attributed to the stretching modes of Ti–O [12, 29, 32]. Additionally, the expected band at 671 cm^{-1} is due to the Ti–O–Ti stretching vibration [23]. In the case of the S2 sample, all the above mentioned bands (except the peaks at about 710 and 923 cm^{-1}) are detected. Additionally, we can state that the Raman peaks having maxima at about 372 cm^{-1} (S1) and 361 cm^{-1} (S2) are probably due to TiO_2 (anatase).

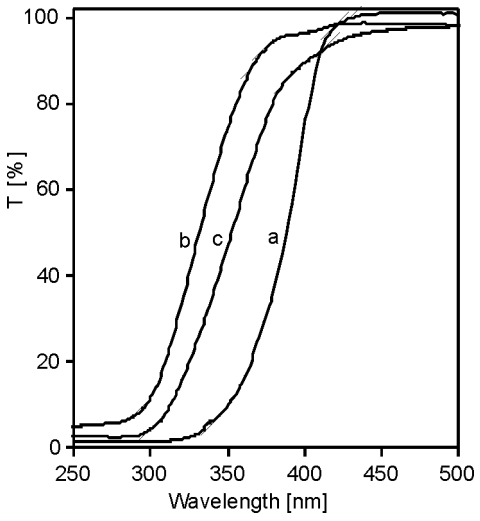

Fig. 7. The DR-UV-vis transmission spectra of: a) pristine TiO_2-P25, b) S1 and c) S2

The DR-UV-vis spectrum of the pristine TiO_2-P25 (spectrum a), as well as the spectra of the S1 and S2 samples (spectra b and c) are presented in Fig. 7. The absorption edges of S1 and S2 shift towards shorter wavelengths in comparison with the pristine TiO_2-P25. The band gap energies of all investigated samples were determined using the DR-UV-vis method and were calculated from the equation:

$$\alpha h\nu = A(h\nu - EG)^r \tag{1}$$

where α is the absorption coefficient, $h\nu$ is the photon energy, EG is the optical band gap, A is a constant which does not depend on the photon energy and r is a parameter equal to 1/2, 3/2, 2 or 3, depending on the type of transition (1/2 for allowed direct, 2 for allowed indirect, 3 for forbidden direct and 3/2 for forbidden indirect optical transitions) [33, 34]. We can state that the band gap energies of the S1 and S2 samples are greater than that for pristine TiO_2-P25. The calculated EG are 3.049, 3.637 and 3.420 eV for TiO_2-P25, S1 and S2, respectively.

Table 1. The band gap values and nitrogen adsorption data for the samples under study

Sample	EG [eV]	BET surface area [m^2/g]	Mean pore diameter [nm]
TiO_2-P25	3.049	52	6.9
S1	3.637	15.6	7.9
S2	3.420	30.3	7.2

Additional characteristic features of the produced nanostructures and the starting material (such as BET surface area, mean pore diameters and band gap energies) are listed in Table 1. According to the manufacturer's data, TiO_2-P25 has the specific surface area of 52 m^2/g and the mean pore diameter of 6.9 nm. The specific surface areas of S1 and S2 samples are lower than that of the pristine TiO_2-P25 sample. For example, the BET surface areas of the S1 and S2 samples are about 3 and 2 times lower, respectively, than that of the TiO_2-P25 sample.

3.2. Photocatalytic reactions

The photocatalytic activities of the produced materials were studied by observing the reaction, specifically the photocatalytic decolourisation, of two organic dyes (Reactive Red 198 – RR198 and Reactive Black 5 – RB5) as model contaminants. At the first stage, the control reaction without catalysts and using RR198 and RB5 solutions (having the concentration of 30 mg/dm^3) was investigated. A small degree of decolourization was observed in both the dyes (RR198 – 5.64%, RB5 – 3.12%) after 2 h of UV irradiation.

Further experiments were conducted using the same organic dyes but contents of all studied materials did not change (10 mg of TiO_2-P25, S1 and S2 on 20 cm^3 of dye solution). Figure 8 shows the decolourization profiles of RR198 and RB5 dyes, in the presence or absence of the considered catalysts, and after being subjected to UV-light irradiation for 2 h. The both organic dyes undergo total decolourization after 1 h of UV illumination, but only for the TiO_2-P25 catalyst. After 2 h of irradiation, the degrees of decolourization of the RR198 and RB5 dyes were 25.7% and 54.9% for the S1 catalyst, and 34.5% and 61.4% in the case of the S2 catalyst. Furthermore, Figure 8 also shows that the sample obtained after acid treatment (S2) exhibits higher catalytic activity than the one obtained directly after hydrothermal reaction (S1).

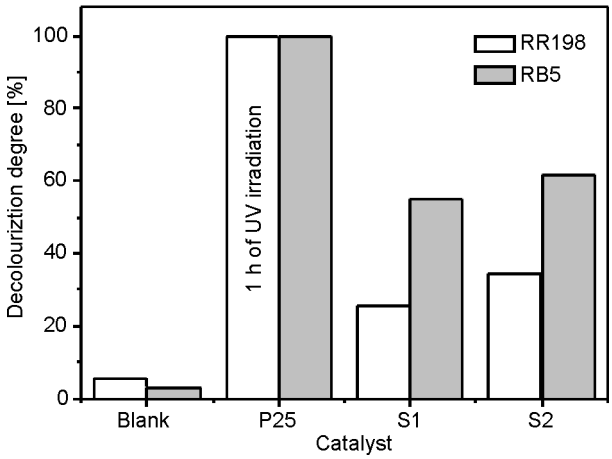

Fig. 8. Photocatalytic decomposition of RR198 and RB5 in the presence of the pristine TiO_2-P25 and S1 and S2 samples

As is well known, the catalytic activity of a catalyst material is directly proportional to its BET surface area. Pristine TiO_2-P25 exhibits the highest BET surface area (52 m^2/g) and the highest photocatalytic activity in the dye decolourization reaction. Moreover, one can observe that the BET surface areas of the produced samples decreased considerably after the hydrothermal reaction (S1, 15.6 m^2/g) and subsequently increased after acid treatment (S2, 30.3 m^2/g). As is clearly observed from the data, there is a direct correlation between the BET surface area and the degree of dye decolourization: the higher the BET surface area, the higher the degree of decolourization of the RR198 and RB5 dyes (TiO_2-P25 > S2 > S1). Additionally, it is worth pointing out that RR198 and RB5 dyes are not adsorbed on the S1 and S2 surfaces. It is known that the adsorption of the reagents on the surface of the photocatalyst is a very important consideration in the photocatalytic process. This might be a possible reason why the nanostructures described here exhibit less photocatalytic activity, compared with the TiO_2-P25 sample, in the dye decolourisation reaction. Detailed studies to verify the proposed explanation are currently in progress.

4. Conclusions

The syntheses and detailed characterization of TiO_2-derived nanorods using commercial TiO_2-P25 as a precursor have been described. The obtained nanorods having an average length of 5.9 μm (after the hydrothermal reaction) and 4.05 μm (after the hydrothermal reaction and acid treatment) revealed to be a composition of different layers of titanates ($Na_2Ti_4O_9$, Na_2TiO_3, $H_2Ti_5O_{11}\cdot H_2O$). Additionally, it was proved that the fabricated nanorods are less active in the photocatalytic reaction of decolourisation of organic dyes than pristine TiO_2-P25. Furthermore, we have proved that the nanorods synthesized from pristine TiO_2-P25 exhibit higher photocatalytic activity than the nanorods synthesized either from hydrothermally treated TiO_2-P25 (referred to as material S1 in this paper) or from hydrothermal-and-acid-treated TiO_2-P25 (referred to as material S2 in this paper).

Acknowledgements

This work was sponsored by the Polish State Committee for Scientific Research, under grant N523 025 32/0983 (B. Z.).

References

[1] KASUGA T., HIRAMATSU M., HOSON A., SEKINO T., NIIHARA K., Langmuir, 14 (1998), 3160.
[2] YU H., YU J., CHENG B., ZHOU M., J. Solid State Chem., 179 (2006), 349.
[3] WU D., LIU J., ZHAO X., LI A., CHEN Y., MING N., Chem. Mater., 18 (2006), 547.
[4] LIU L., ZHANG Y., Sensor Actuat A., 116 (2004), 394.
[5] CHEN C.-C., YEH C.-C., LIANG C.-H., LEE C.-C., CHEN C.-H., YU M.-Y., LIU, L.C. CHEN H.-L., J. Phys. Chem. Solids, 62 (2001), 1577.
[6] BOROWIAK-PALEN E., PICHLER T., GRAFF A., KALENCZUK R.J., KNUPFER M., FINK J., Carbon, 42 (2004), 1123.
[7] LI Y., WANG J., DENG Z., WU Y., SUN X., YU D., YANG P., J. Am. Chem. Soc., 123 (2001), 9904.
[8] NATH M., RAO C.N.R., J. Am. Chem. Soc., 123 (2001), 4841.
[9] NIAN J-N., TENG H., J. Phys. Chem. B., 110 (2006), 4193.
[10] WU Q., HU Z., WANG X., J. Am. Chem. Soc., 125 (2003), 2024.
[11] ARNOLD M.S., AVOURIS P., PAN Z., J. Phys. Chem. B., 107 (2003), 659.
[12] KOLEN'KO Y.V., KOVNIR K.A., GAVRILOV A.I., GARSHEV A.V., FRANTTI J., LEBEDEV O.I., CHURAGULOV B.R., TENDELOO G. V., YOSHIMURA M., J. Phys. Chem. B., 110 (2006), 4030.
[13] XU C., ZHAN Y., HONG K., WANG G., Solid State Commun., 126 (2003), 545.
[14] ZHU Y., LI H., KOLTYPIN Y., HACOHEN Y.R., GEDANKEN A., Chem. Commun., 24 (2001), 2616.
[14] KASUGA T., HIRAMATSU M., HOSON A., SEKINO T., NIIHARA K., Adv. Mater., 11 (1999), 1307.
[15] JR E.M., ABREU M.A.S., PRAVIA O.R.C., MARINKOVIC B.A., JARDIM P., RIZZO F.C, ARAUJO A.S., Solid State Sci., 8 (2006), 888.
[16] CHEN Q., DU G.H., ZHANG S., PENG L.M., Acta Crystallogr. B., 58 (2002), 587.
[17] YANG D.B., CHAN Y.F., ZHANG X.Y., ZHANG W.F., YANG Z.Y., WANG N., Appl. Phys. Lett., 82 (2003), 281.
[18] SUN X., LI Y., Chem.-Eur. J., 9 (2003), 2229.
[19] PAVASUPREE S., SUZUKI Y., YOSHIKAWA S., KAWAHATA R., J. Solid State Chem., 178 (2005), 3110.
[20] YOSHIDA R., SUZUKI Y., YOSHIKAWA S., Mater. Chem. Phys., 91 (2005), 409.

[21] MA Y., LIN Y., XIAO X., ZHOU X., LI X., Mater. Res. Bull., 41 (2006), 237.
[22] MENG X., WANG D., LIU J., ZHANG S., Mater. Res. Bull., 39 (2004), 2163.
[23] TAHIR M.N., THEATO P., OBERLE P., MELNYK G., FAISS S., KOLB U., JANSHOFF A., STEPPUTAT M., TREMEL W., Langmuir, 22 (2006), 5209.
[24] KASUGA T., Thin Solid Films, 496 (2006), 141.
[25] WEI M., KONISHI Y., ZHOU H., SUGIHARA H., ARAKAWA H., Solid. State Commun., 133 (2005), 493.
[26] YU L., ZHANG X., Mater. Chem. Phys., 87 (2004), 168.
[27] ŠTENGL V., BAKARDJIEVA S., ŠUBRT J., VEČERNIKOVA E., SZATMARY L., KLEMENTOVA M., BALEK V., Appl. Catal. B., 63 (2006), 20.
[28] MA R., FUKUDA K., SASAKI T., OSADA M., BANDO T., J. Phys. Chem. B., 109 (2005), 6210.
[29] QIAN L., DU Z-L., YANG S-Y., JIN Z-S., J. Mol. Struct., 749 (2005), 103.
[30] PAPP S., KOROSI L., MEYNEN V., COOL P., VANSANT E.F., DEKANY I., J. Solid State Chem., 178 (2005), 1614.
[31] MENZEL R., PEIRÓ A.M., DURRANT J.R., SHAFFER M.S.P., Chem. Mater., 18 (2006), 6059.
[32] LARRUBIA M.A., RAMIS G., BUSCA G., Appl. Catal. B., 27 (2000), L145.
[33] HASAN M.M., HASEEB A.S.M.A., SAIDUR R., MASJUKI H.H., PWASET, 30 (2008), 221.
[34] BERNARDI M.I.B., LEE E.J.H., LISBOA-FILHO P.N., LEITE E.R., LONGO E., VARELA J.A., Mat. Res., 4 (2001) 223.

Received 20 February 2008
Revised 21 September 2009

Materials Science-Poland, *Vol. 28*, *No. 3*, *2010*

Structural characterization and electrical resistance of the $BaPb_{1-x}Bi_xO_3$ system

M. S. DA LUZ*, A. D. A. COELHO, C. A. M. DOS SANTOS,
H. J. IZARIO FILHO, A. J. S. MACHADO

Escola de Engenharia de Lorena – USP, P. O. Box 116, Lorena, SP 12602-810, Brazil

The electrical resistance $R(T)$ in function of temperature T, and X-ray powder diffraction (XRD) patterns of polycrystalline samples of the $BaPb_{1-x}Bi_xO_3$ system have been described. $R(T)$ measurements of single phase samples show that $BaPbO_3$ exhibits metal-like properties, and that the system exhibits superconductivity in the $0.005 < x < 0.30$ range, but insulating properties for $x > 0.30$. A careful analysis of the onset of the critical temperature (T_C) reveals its strong dependence on the sample composition in the range $0.005 < x < 0.30$ which may be related to the superconducting volume fraction ultimately leading to connected or disconnected superconducting clusters, similar to those observed in granular superconductors.

Keywords: *electrical conductance; XRD patterns; superconductivity; superconducting clusters*

1. Introduction

In 1975, Sleight et al. discovered superconductivity in Bi doped $BaPbO_3$ perovskite phase [1]. $BaPb_{1-x}Bi_xO_3$ compound exhibits a maximum T_C near 13 K depending on the sample composition and heat treatment [2, 3]. By doping the insulator $BaBiO_3$ with K at the Ba sites, Cava et al. and Matheiss et al. reported a new oxide superconductor having a very high critical temperature T_C near 30 K [4–6]. As a consequence, some authors referred to $BaPb_{1-x}Bi_xO_3$ and $BaBi_{1-x}K_xO_3$ as the precursors of the high T_C cuprates [6]. Some questions regarding how structural distortions, doping effects, and critical temperature T_C depend on the sample composition have also received some interest [2, 4, 7–11]. Studies [11] of temperature dependences of electrical resistance, $R(T)$, of the $BaPb_{1-x}Bi_xO_3$ system revealed that Bi substitution at Pb sites induces a superconductor–insulator transition (SIT) in compounds with x very close to 0.30. Several authors have focused great attention on the SIT in low and high temperature superconductors [12–18], however the SIT mechanism of the

*Corresponding author, e-mail: luz@physics.montana.edu

$BaPb_{1-x}Bi_xO_3$ system is not completely understood [11]. As discussed by some authors, two possible mechanisms may explain disorder induced SIT in granular superconductors [18]. Basically, superconductivity can be suppressed either by reducing the amplitude or changing the phase of the superconductor order parameter. Illustrative examples of both kinds of SIT are evident by observing the $R(T)$ curves obtained for homogeneous Bi and granular Ga films [12, 13, 18]. In homogeneous superconductors, SIT occurs when the critical temperature of the sample is reduced [13, 18]. On the other hand, disorder tuned SIT in granular samples occurs through a different mechanism. In such a case, suppression of long range order occurs as a consequence of the localization of the superconducting clusters without reduction of the T_C [12, 18].

In this paper, we present a systematic structural characterization of the $BaPb_{1-x}Bi_xO_3$ system and we describe its electrical resistance in function of temperature. The results allow us to discuss some important aspects concerning the dependence of T_C on the sample composition, and the influence of Bi substitution at Pb sites on the transport properties of the $BaPb_{1-x}Bi_xO_3$ system.

2. Experimental

Polycrystalline samples of $BaPb_{1-x}Bi_xO_3$ were fabricated by the solid state reaction technique using high purity PbO_2, Bi_2O_3, and $BaCO_3$ powders. The powders were compacted, calcined at 780 °C for 24 h, and finally heat treated at 800–850 °C for 24–48 h, depending on the sample composition. All samples were characterized by X-ray powder diffractometry using CuK_α radiation. The diffractograms were indexed using a pseudocubic structure ($P23$) with the lattice parameter $a \approx 4.3$ Å [4, 6] and compared with simulations made with the powder cell program [19], utilizing *International Tables for X-ray Crystallography* [20]. A Perkin Elmer spectrometer (Analyst 800) was used to determine the composition of the samples after heat treatments. The electrical resistances of the samples in function of temperature were measured with a Maglab Oxford system, capable of generating the field strength of 9 T, and by employing the conventional four probe technique. Electrical terminals were prepared using low resistance (ca. 0.1 Ω) sputtered Au contacts.

3. Results

Results of chemical analyses revealed that the nominal composition of the samples was essentially unchanged during heat treatments. None of the analyzed samples exhibited statistically significant differences from the initial composition, within a standard deviation of 3%.

Figure 1 shows the X-ray diffractograms for samples that are representative of the full range ($0 < x < 1.0$) of Bi substitution. The diffractograms exhibit similar peaks, suggesting the samples have the same crystal structure. It is also visible that the dif-

fraction peaks shift with respect to the 2θ angle as the sample composition varies, hence indicating variations in the lattice parameters (notice, for example, how the peaks at $2\theta \sim 70^{o}$ shift systematically to the left as the Bi content x increases between 0 and 1). In spite of questions regarding structural distortions in the $BaPb_{1-x}Bi_xO_3$ system to monoclinic, orthorhombic, or tetragonal [4, 6–8], we have analyzed diffractograms under the assumption that the unit cell is pseudocubic as others have also done [4, 6].

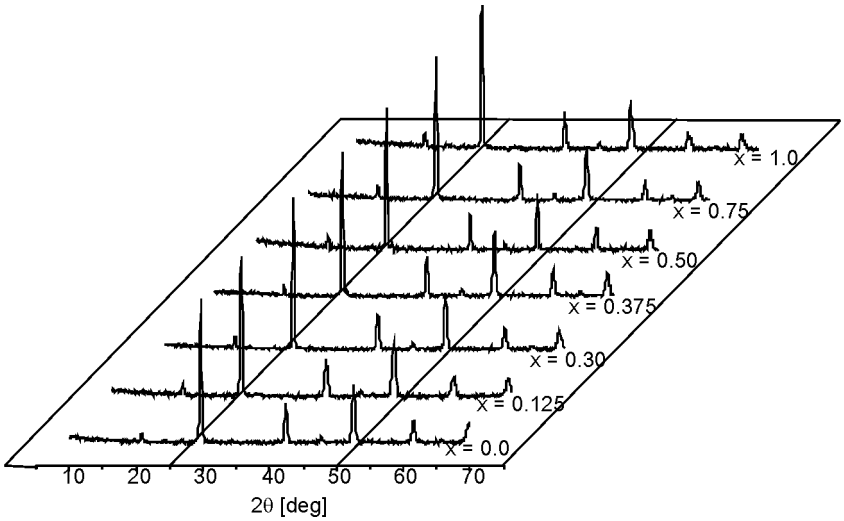

Fig. 1. X-ray powder diffractograms of samples with different Bi contents, over the full range of substitution

Figure 2 shows experimental and simulated diffractograms for $x = 0.125$. The simulated values are in close agreement with the experimental results. In Figure 3, the cubic lattice parameter is plotted against the level x of Bi in the samole. One can observe an approximately linear dependence, suggesting complete substitutional solubility of Bi in $BaPb_{1-x}Bi_xO_3$. This observation agrees with previous results published in the literature [6].

In order to study the transport properties of the samples, electrical resistance in function of temperature was measured. Figure 4 shows the electrical resistivity $R(T)$ plotted against temperature T of samples having compositions with $x \in \{0.0, 0.05, 0.15, 0.20, 0.30, 0.375\}$. It is possible to observe how resistivity changes from the metallic ($BaPbO_3$) to insulator ($x > 0.3$) as the content of Bi in the compound increases. In the $0.05 < x < 0.30$ range, the samples exhibit evidence of superconductivity.

In order to carefully identify the onset of the critical temperature for all superconducting samples, T_C has been defined as the point at which dR/dT versus T changes from normal to superconducting state. T_C defined in this way is plotted in Fig. 5 in function of x in the compound.

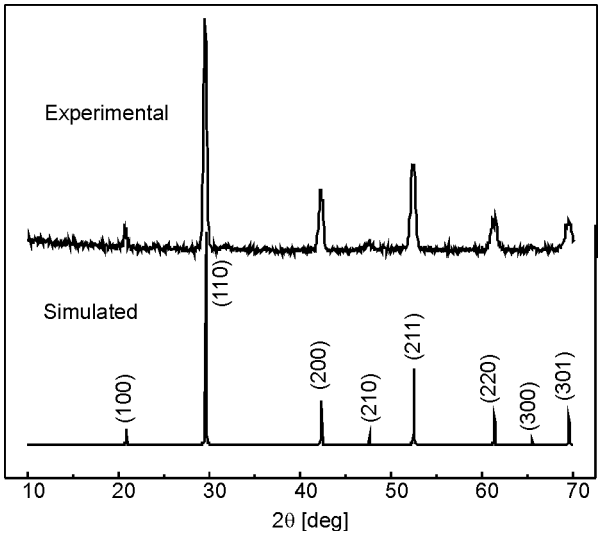

Fig. 2. Experimental and simulated diffractograms for the sample with $x = 0.125$

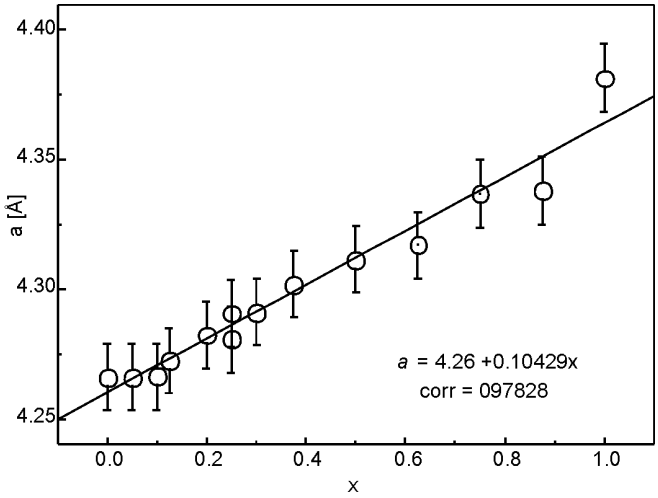

Fig. 3. Pseudocubic lattice parameters (calculated from the diffractograms of simulations) in function of the Bi content (x)

The superconducting critical temperature increases systematically from 11.2 K at $x = 0.005$ to ca. 12 K at $x = 0.15$, and decreases to 11.6 K at $x = 0.30$. Below $x = 0.005$ and above $x = 0.30$, superconductivity in the system vanishes (see Fig. 4). This behaviour is similar to results reported in the literature which show that T_C increases systematically from zero at $x = 0.0$ to ca. 12 K at $x \approx 0.20$, remaining constant until $x \approx 0.30$, and finally vanishing at $x > 0.30$ [2, 3]. As one can see from Fig. 4, the transition to the superconducting state does not reach zero resistance for samples having low Bi contents ($0.005 < x < 0.05$).

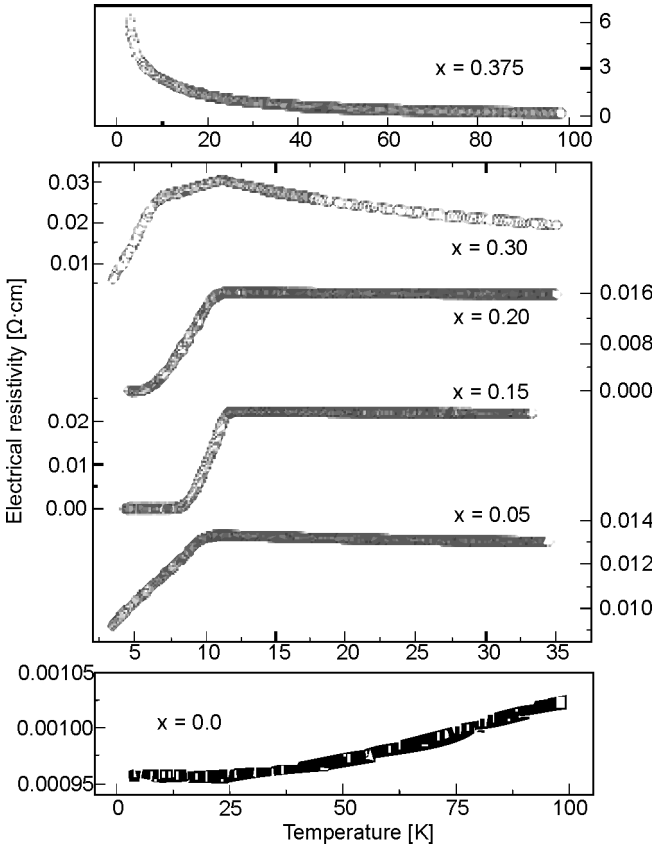

Fig. 4. Electrical resistivity in function of temperature for samples having Bi contents $x \in \{0.0, 0.05, 0.15, 0.20, 0.30, 0.375\}$

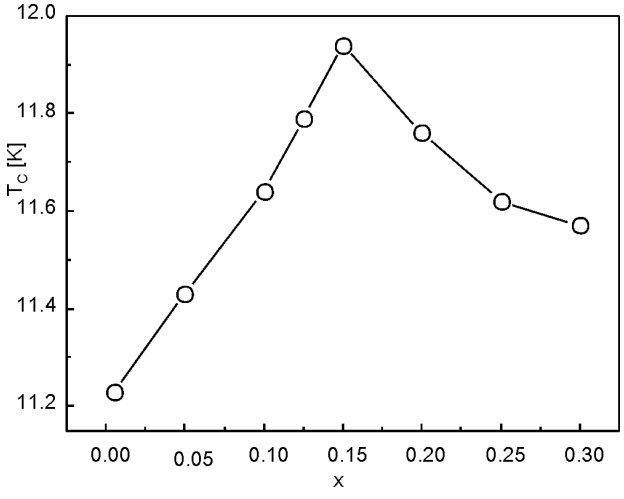

Fig. 5. The dependence of T_C on the Bi content x in the samples

Our interpretation of these results is that it is related to the fraction of superconducting clusters present in the samples. Research [21] on the transport properties of $Bi_2Sr_2Ca_{1-x}Pr_xCu_2O_{8+d}$ (Bi2212 + Pr) polycrystalline samples has shown that the transition to the zero resistance superconducting state depends on the fraction of superconducting clusters in the sample. It was also observed that the zero resistance superconducting state is only reached by samples with a large enough superconducting fraction [21, 22]. If we assume that the resistive transition in the $BaPb_{1-x}Bi_xO_3$ system can be described by such a mechanism, the transition visible in $R(T)$ curves must depend on the superconducting fraction. Therefore, for samples with low Bi contents, this fraction must be small, and therefore zero resistance is not attained, which is consistent with the results shown in Fig. 4. On the other hand, if the superconducting fraction is close to the percolation threshold, a decrease in the transition intensity can be observed which provides information about the onset of the T_C value. This behaviour suggests that the existence of superconductivity in the $BaPb_{1-x}Bi_xO_3$ system must be governed by the same mechanism of inhomogeneous superconductivity as that reported for high-T_C superconductors [21, 23].

4. Summary

Assuming the $BaPb_{1-x}Bi_xO_3$ system has a pseudocubic crystal structure, X-ray power diffraction data reveal there is a linear relationship between the lattice parameter and the content of Bi in the compound. This indicates complete substitutional solubility of Bi in this system. All prepared samples in the Bi range $0.005 < x < 0.30$ exhibit evidence of superconductivity. Careful analysis shows that, for superconducting samples, the critical temperature T_C depends strongly on the content of Bi. We have discussed this behaviour within the context of inhomogeneous superconductivity. The dependence of T_C on the Bi content x indicates that granular samples of the $BaPb_{1-x}Bi_xO_3$ system experience transition to the insulating state due to suppression of the superconducting coupling, much like the transition mechanism observed for granular superconductors.

Acknowledgements

This work has been supported by the FAPESP under grants 97/11113-6, 99/09864-9, and 03/01982-0. The authors also thank B. D. White for valuable comments.

References

[1] SLEIGHT A.W., GILLSON J.L., BIERSTEDT P.E., Sol. State Commun., 17 (1975), 27.
[2] BATLOGG B., Physica B, C, 126 (1984), 275.
[3] HIKATA T., KASATANI Y., YOSHIZAKI R., UWE H., SAKUDO T., SUZUKI T., Phys. Rev. B, 36 (1987), 5578.
[4] CAVA R.J., BATLOGG B., KRAJEWSKI J.J., FARROW R., RUPP W. Jr., WHITE A.E., SHORT K., PECK W.F., KOMETANI T., Nature, 332 (1988), 814.

[5] MATTHEISS L.F., HAMANN D.R., Phys. Rev. Lett., 60 (1988), 2681.
[6] CAVA R.J., BATLOGG B., ESPINOSA G.P., RAMIREZ A.P., KRAJEWSKI J.J., PECK W.F. Jr., RUPP L.W. Jr., COOPER A.S., Nature, 339 (1989), 291.
[7] COX D.E., SLEIGHT A.W., Acta Crystallogr. B, 35 (1979), 1.
[8] UEMURA Y.J., STERNLIEB B.J., COX D.E., BREWER J.H., KADONO R., KEMPTON J.R., KIEFL R.F., KREITZMAN S.R., LUKE G.M., MULHERN P., RISEMAN T., WILLIAMS D.L., KOSSLER W.J., YU X.H., STRONACH C.E., SUBRAMANIAN M.A., GOPALAKRISHNAN J., SLEIGHT A.W., Nature, 335 (1988), 151.
[9] CHAILLOUT C., SANTORO A., REMEIKA J.P., COOPER A.S., ESPINOSA G.P., MARESIO M., Sol. State Commun., 65 (1988), 1363.
[10] PHILLIPS J.C., [In:] *Physics of High-T_C Superconductors*, Academic Press, London (1989), pp. 66–74.
[11] GABOVICH A.M., MOISEEV D.P., Sov. Phys. Usp., 29 (1986), 1137.
[12] JAEGER H.M., HAVILAND D.B., GOLDMAN A.M., ORR B.G., Phys. Rev. B, 34 (1986), 4920.
[13] HAVILAND D.B., LIU Y., GOLDMAN A.M., Phys. Rev. Lett., 62 (1989), 2180.
[14] FISHER M.P.A., Phys. Rev. Lett., 65 (1990), 923.
[15] HEBARD A.F., PAALANEN M.A., Phys. Rev. Lett., 65 (1990), 927.
[16] TANDA S., HONMA M., NAKAYAMA T., Phys. Rev. B, 43 (1991), 8725.
[17] SEIDLER G.T., ROSENBAUM T.F., VEAL B.W., Phys. Rev. B, 45 (1992), 10162.
[18] FINKELSTEIN A.M., Phys. B, 197 (1994), 636.
[19] KRAUS W., NOLZE G., J. Appl. Cryst., 29 (1996), 301.
[20] *International Tables for X-ray Crystallography*, Vol. 1, F.M. Norman, H.K. Lonsdale, The Kynoch Press, Birmingham, England, 1969, p. 306.
[21] DOS SANTOS C.A.M., MOEHLECKE S., KOPELEVICH Y., MACHADO A.J.S., Phys. C, 390 (2003), 21.
[22] SUN X., ZHAO X., WU W., FAN X., LI X.-G., KU H.C., Phys. C, 307 (1998), 67.
[23] OVCHINNIKOV YU.N., WOLF S.A., KRESIN V.Z., Phys. Rev. B, 63 (2001), 064524.

Received 9 May 2008
Revised 6 November 2008

Materials Science-Poland, *Vol. 28*, *No. 3*, *2010*

Sol-gel combustion synthesis of $Bi_{0.5}Na_{0.5}TiO_3$–ZrO_2 ceramic composite

S. KANAGESAN, C. KUMAR*, R. VELMURUGAN, S. JESURANI

Department of Physics, Faculty of Engineering and Technology, SRM University, Kattankulathur 603 203, Chennai, India

Bismuth sodium zirconium titanate, belonging to a new class of ceramic composite powders, was prepared by the sol-gel combustion technique. A yellow precipitate was obtained by slow evaporation of precursor solution at 90 °C for 2 h. The final composition of powder is $Bi_{0.5}Na_{0.5}TiO_3/ZrO_2$. Small, elongated particles of uniform size and shape were identified with an atomic force microscope. The X-ray diffraction pattern confirms that the final powder is composite in nature and consists of a very distinct phase of bismuth titanate, sodium bismuth titanate and zirconia. The electric permittivity for the samples sintered at 1050 °C is about 640 at 50 Hz.

Keywords: *sol-gel combustion; composite; XRD; FTIR; AFM; electric permittivity*

1. Introduction

Due to their wide range of applications such as touch sensors for micromanipulation in microbiology [1], piezoelectric transformers and actuators [2–4], lead zirconium titanate (PZT) piezoelectric ceramics are considered as an important candidate material in electronic industries [5–7]. But, the worldwide restriction on hazardous substances limits the use of lead. A large quantity of lead based piezoelectric, ferroelectric and electrostrictive materials such as $PbZrO_3$–$PbTiO_3$ (PZT) [8–10] and $Pb(Mg_{1/3}Nb_{2/3})O_3$–$PbTiO_3$ (PMN–PT) [11, 12], are produced every year. Due to the toxicity of lead based ceramics, alternative lead free materials are highly preferred in the electronic industry. For two decades, great effort has been made to find high performance lead free materials. For instance, $(Bi_{0.5}Na_{0.5})TiO_3$ (BNT) [13, 14], $Bi_4Ti_3O_{12}$ (BT) [15–18], $SrBi_2Ta_2O_9$ [19, 20] and $BaTiO_3$ [21] based systems have been extensively studied. However, the remnant polarization and electrostrictive properties of these lead

*Corresponding author, e-mail: vckumar60@yahoo.co.in

free materials are still far inferior to the lead-containing materials currently in use. By varying the chemical composition, dielectric and piezoelectric properties of lead free ceramics can be altered. Such materials attract much attention as actuators in electronic applications. Extensive studies, in multiple directions, have been made on lead free piezoelectric ceramics by the research community such as the synthesis of pure ceramics, ceramic–ceramic composites and ceramic polymer composite by various techniques, such as the sol-gel method [22–24], coprecipitation [25, 26], solid state reaction [25] and high temperature deposition technique. Above all, bismuth sodium titanate, $Bi_{0.5}Na_{0.5}TiO_3$ (BNT), is considered to be an excellent alternative candidate as a lead free piezoelectric ceramics. BNT is a ferroelectric ceramics with a remnant polarization of 38 μC/cm^2, Curie temperature (T_c) of 320 °C and a coercive field (E_c) of 73 kV/cm at room temperature. However, although bismuth sodium titanate (BNT) is considered to be a good alternate material to PZT ceramics, it has the drawback of having a strong coercive field (E_c) that causes problems in the poling process.

It is known that zirconia is one of the key materials for engineering and electronics. By doping a small amount of zirconia, the properties of the matrix material can be altered. It has been demonstrated that by doping 0.05 mol % of zirconia, $BaTiO_3$ ceramics showed a fairly satisfactory piezoelectric response, with a d_{33} value of 236 pC/N at room temperature [27]. From this viewpoint, the present work aims to synthesise lead free ferroelectric ceramic, bismuth sodium zirconium titanate (BNZT), by self-propagating combustion synthesis; this involves the exothermic reaction between metal nitrates and an organic fuel, typically ethanol, methanol, urea, or glycine. The thermal behaviour of the dried gel was analyzed by differential scanning calorimetry (DSC) and thermogravimetric analysis (TGA). An X-ray diffractometer (XRD) was used to evaluate the phase formation of the calcined powder. Fourier transform infrared spectroscopy (FTIR) was used to identify tvarious functional groups. The particle morphology and size was obtained by an atomic force microscopic study (AFM).

2. Experimental

Solutions of bismuth nitrate, sodium nitrate, zirconium oxychloride and titanium isopropoxide were used as starting materials. Three separate solutions were prepared and mixed together for combustion synthesis. A stable solution of titanium isopropoxide ($TiC_{12}H_{28}O_4$) was obtained by mixing $TiC_{12}H_{28}O_4$ with acetyl acetone and 2-isoproponal (solution 1). The nominal amount of zirconium oxychloride ($ZrOCl_2 \cdot 8H_2O$) was dissolved in methanol (solution 2). Solution 3 was prepared by dissolving bismuth nitrate with acetic acid and HNO_3. The required amount of sodium nitrate was added to solution 3. After preparation, all three solutions were mixed together under stirring, which yielded a firebrick coloured viscous sol. The sol was slowly evaporated under stirring at 90 °C. After 2 h, a foam-like precipitate formed, due to the exother-

mic reaction between the metal nitrates and organic fuel. The precipitate was combusted at 400 °C. The final calcination was carried out at 700 °C for 3 h to produce $Bi_{05}Na_{05}TiO_3ZrO_2$ composite powder. The calcined powder was ground in a planetary mill in order to obtain fine particles.

3. Results and discussion

The X-ray diffraction pattern (Fig. 1) for the bismuth sodium zirconium titanate (BNZT) composite calcined at 700 °C shows the formation of mixed phases. Characteristic peaks corresponding to monoclinic $BiTi_3O_{12}$ crystals (JCPDS File No. 80 -2143) were recordered at 14.61°, 24.35°, 29.40°, 30.06°, 34.08°, 48.99°, 49.89° and 53.26°. The formation of $mZrO_2$ and $BiTiO_3$ was confirmed by the peaks at 28.09° and 33.56°, respectively. The reflections by rhombohedral BNT crystal planes (JCPDS File No.36-0340) were predicted to be at 32.48°, 40.5°and 58.26° with lower intensities. Since no powder diffraction data is available for the BNZT composite, the phase formation was analyzed by comparing the existing powder diffraction data files for BNT, BT and ZrO_2

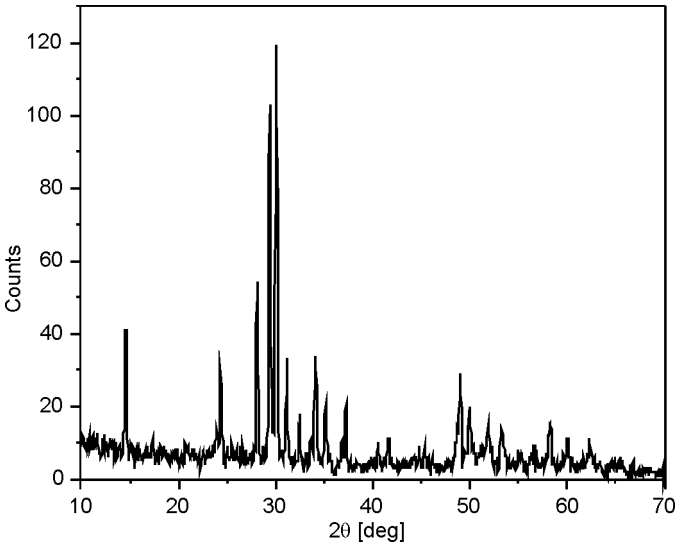

Fig. 1. X-ray diffraction pattern of BNZT composite

The FTIR spectrum of BNZT composite gel is shown in Fig. 2. Three absorption bands corresponding to N–H stretching modes were observed at 3184.3, 1355.9 and 1309.6 cm^{-1}. The vibration at 1384.8 cm^{-1} indicates the presence of nitrate, and the absorption band around 1541 cm^{-1} is due to NO_2 vibration. The strong and sharp absorption bands at 894.9 cm^{-1} and 812 cm^{-1} were recorded as being related to ν(Zr–O) $+\delta$(O–C=O).

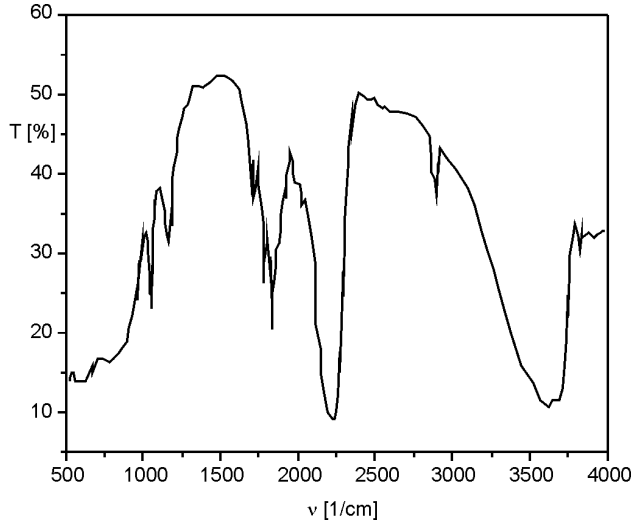

Fig. 2. FTIR spectrum of BNZT gel dried at 100 °C

The DSC (Fig. 3) shows various decomposition stages of BNZT gel with respect to temperature. An endothermic peak at 149 °C is due to removal of adsorbed water, and a broad exothermic peak between 225 °C to 400 °C is due to the burn out of oxalate and nitrates from the amorphous gel. A small exothermic peak around 470 °C may be related to the crystallization of zirconium oxalate gel into zirconia. A small exothermic peak between 520 °C to 600 °C is due to the formation of sodium bismuth titanate phase. From the TGA analysis, a major weight loss of 29 % was predicted, and the overall yield was calculated to be about 38 % of the starting materials.

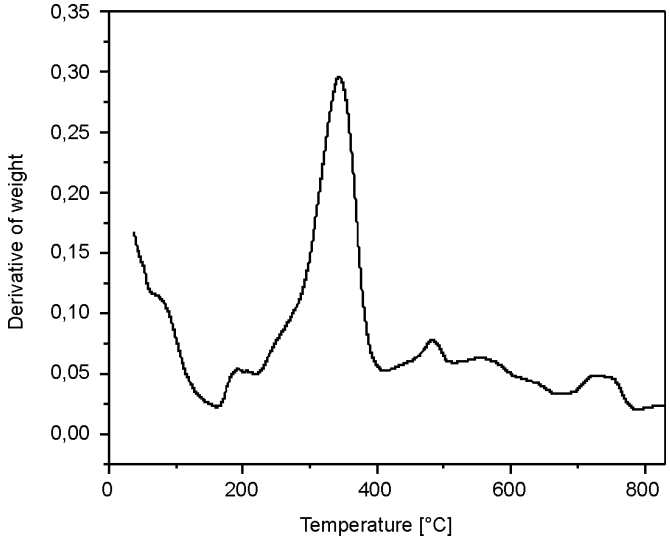

Fig. 3. DSC of BNZT composite

For the AFM study, the particles were deposited on a Si wafer. Before deposition, the wafer was thoroughly cleaned with a mixed aqueous solution of HNO_3 and H_2SO_4. The BNZT powder was dispersed in acetone and dip coated on the Si wafer. AFM images were taken with a silicon cantilever, with the force constant of 0.02 N/m and the tip height of 10–15 μm in a contact mode. Figure 4 shows the AFM image of BNZT particles having uniform size and shape. After data fitting, line profiles were taken to calculate the size of individual BNZT particles. The particles were not spherical in shape, rather they were elongated. The width and length of a BNZT particle was measured to be 170 nm and 550 nm, respectively.

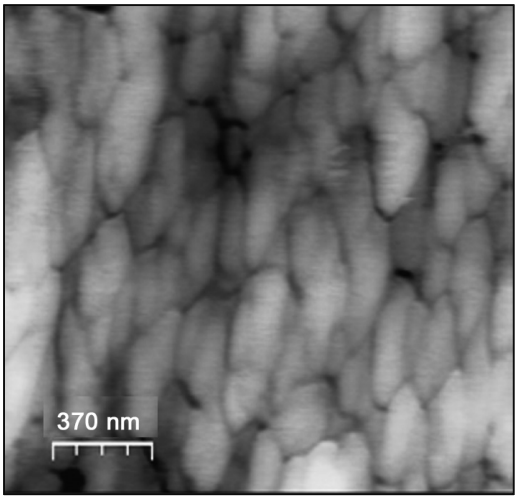

Fig. 4. AFM image of BNZT composite powder

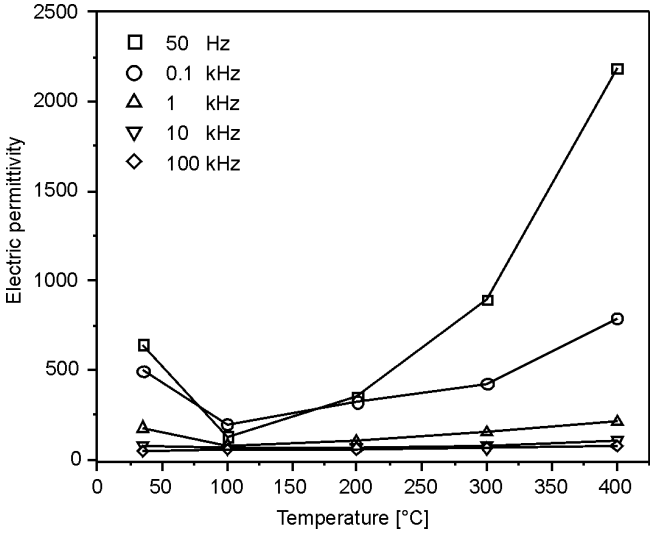

Fig. 5. Temperature dependence of the electric permittivity

Figure 5 shows the temperature dependence of the electric permittivity. In the higher frequency range (1–100 kHz), the electric permittivity (ranging from 75 to 211) is more or less temperature independent and does not increase much for temperatures below 400 °C. But, at lower frequencies (50–100 Hz), the change of the electric permittivity is significant, and attains a maximum value of 2200 at 400 °C. The electric permittivity for pure BNT is 400 at room temperature and 1800 at 400 °C for 100 kHz [28]. For BNT thin film, the electric permittivity was measured to be 300 [29]. Zhu et al. measured the electric permittivity of potassium bismuth titanate to be 536 [30].

Therefore, in the higher frequency range, the zirconia doped BNT has a lower electric permittivity compared with pure BNT. The electric permittivity for the considered composite was measured to be 46 at room temperature and 75 at 400 °C, at 100 kHz. But, in the lower frequency range, the considered BNZT composite has much higher electric permittivity of 640 at room temperature and 2200 at 400 °C at 50 Hz.

4. Conclusions

The X-ray diffraction analysis of the calcined powder indicated that the addition of zirconia suppresses the predominant reflection peak at 32.48° corresponding to BNT phase. The final powder shows a mixed phase which confirms the formation of composite between BNT and ZrO_2. The reason why the measured electric permittivity, at higher frequencies is lower than the expected value may be because the ionic radius of Zr^{4+} is higher than that of Ti^{4+}. For equal molar mixing of ZrO_2 and BNT, zirconium exceeds the stabilization limits and reduces the polarization attributable to the Ti^{4+} ion, and hence the electric permittivity is reduced to a low value. The relaxation temperature of the considered composite was not predicted to lie below 400 °C. Therefore, heavy zirconia doping suppresses the formation of BNT phase and reduces the dielectric permittivity, increasing the relaxation temperature. The ferroelectric property of the considered material is under investigation.

Acknowledgement

The authors would like to thank the Honorable Chancellor Thiru T. R. Pachamuthu and Vice-Chancellor Thiru P. Sathyanarayanan, SRM University, Kattankulathur, for their cooperation and encouragement to carry out this work.

References

[1] YOON CH.-B., JUN S.-H., LEE S.-M., KIM H.-E., LEE K.-W., J. Am. Ceram. Soc., 89 (2006), 1333.
[2] ANDO A., KIMURA M., MINAMIKAWA T., SAKABE Y., Int. J. Appl. Ceram. Tech., 2 (2205), 33.
[3] KURIHARA K., KONDO M., Ceram. Int., 34 (2008), 695.
[4] KANDA T., KUROSAWA M.K., Ultrasonic, 40 (2002), 61.
[5] YU B.-Y., WEI W.-CH., Johnson D.W., J. Am. Ceram. Soc., 88 (2005), 2328.
[6] GUIGUES B., GUILLAN J., DEFAY E., GARREC P., WOLOZAN D., ANDRE B., LAUGIER F., PANTEL R., GAGNARD X., AID M., J. Eur. Ceram. Soc., 27 (2007), 3851.

[7] LUO Y., LIU X., Mater. Lett., 59 (2005), 3881.
[8] BELAVIC D., SANTO ZARNIK M., HOLC J., HROVAT M., KOSEC M., DRNOVSEK S., CILENSEK J., MACEK S., Int. J. Appl. Ceram. Tech., 3 (2006), 448.
[9] MEDVECKY L., KMECOVA M., SAKSL K., J. Eur. Ceram. Soc., 27 (2007), 2031.
[10] CHOI T., LEE J., Thin Solid Films, 475 (2005), 283.
[11] LEE J.S., PARK E.CH., LEE S.H., LEE D.S., LEE Y.J., KIM J.S., KIM W., JIN B.M., Mater. Chem. Phys., 90 (2005), 381.
[12] XIA Z., LI Q., ZHANG S., Solid State Commun., 145 (2008), 38.
[13] KIMURA T., YOSHIDA Y., TROLIER-MCKINSTRY S., J. Am. Ceram.Soc., 89 (2006), 869.
[14] SHIEH J., WU K.C., CHEN C.S., Acta Mater., 55 (2007), 3081.
[15] SIMOES A.Z., RICCARDI C.S., GONZALEZ A.H.M., RIES A., LONGO E., VARELA J.A., Mater. Res. Bull., 42 (2007), 967.
[16] KEKA CHAKRABORTY R., ACHARY S.N., PATWE S.J., KRISHNA P.S.R., SHINDE A.B., TYAGI A.K., Ceram. Int., 33 (2007), 601.
[17] ALGUERO M., FERRER P., VILA E., IGLESIAS J.E., CASTRO A., J. Am. Ceram. Soc., 89 (2006), 3340.
[18] ZHANG L., CHU R., ZHAO S., LI G., YIN Q., Mater. Sci. Eng. B, 116 (2005), 99.
[19] LIU J., ZHANG S., YANG CH., DAI L., J. Am. Ceram. Soc., 88 (2005), 85.
[20] AMORÍN H., KHOLKIN A.L., COSTA M.E.V., J. Eur. Ceram. Soc., 25 (2005), 2453.
[21] WANG L., LIU L., XUE D., KANG H., LIU CH., J. Alloy Comp., 440 (2007), 78.
[22] PEREZ J., VYSHATKO N.P., VILARINHO P.M., KHOLKIN A.L., Mater. Chem. Phys., 101 (2007), 280.
[23] BARDAINE A., BOY P., BELLEVILLE P., ACHER O., LEVASSORT F., J. Eur. Ceram. Soc., 28 (2008), 1649.
[24] HAO J., WANG X., CHEN R., LI L., Mater. Chem. Phys., 90 (2005), 282.
[25] GU H., HU Z., HU Y., YUAN Y., YOU J., ZOU W., Coll. Surf. A: Phys. Eng. Aspects, 315 (2008), 294.
[26] SIMON-SEVEYRAT L., HAJJAJI A., EMZIANE Y., GUIFFARD B., GUYOMAR D., Ceram. Int., 33 (2007), 35.
[27] NATEGHI M.R., BARZEGARI M.R., J. All. Comp., 452 (2008), 36.
[28] BAHUGUNA SARADHI B.V., SRINIVAS K., PRASAD G., SURYANARAYANA S.V., BHIMASANKARAM T., Mater. Sci. Eng. B., 98 (2003), 10.
[29] YU T., KWOK K.W., CHAN H.L.W., Thin Solid Films, 515 (2007), 3563.
[30] ZHU M., HOU L., HOU Y., LIU J., WANG H., YAN H., Mater. Chem. Phys., 99 (2006), 329.

Received 11 August 2008
Revised 3 November 2008

Materials Science-Poland, *Vol. 28*, *No. 3*, *2010*

Application of nanoindentation technique to extract properties of thin films through experimental and numerical analysis

A. WYMYSŁOWSKI[1*], Ł. DOWHAŃ[1], O. WITTLER[2], R. MROSSKO[2], R. DUDEK[2, 1]

[1]Wrocław University of Technology, Faculty of Microsystem Electronics and Photonics, ul. Janiszewskiego 11/17, 50-372 Wrocław, Poland

[2]Fraunhofer Institute for Reliability and Microintegration (IZM), Micro Materials Center, Volmerstrasse 7, D-12489 Berlin, Germany

One of the major topics in novel microelectronics are thin film materials – especially their mechanical properties. Accurate description of such materials is necessary in order to assess their reliability and to predict failures in electronic devices. The mechanical attributes of thin films can be determined using the nanoindentation test. However, with this equipment it is only possible to obtain estimates elastic parameters: Young's modulus and hardness of the thin layer. In the paper, it is demonstrated that with a support of numerical methods the plastic behaviour of the material can also be extracted. The numerical FEM model of the nanoindentation test was elaborated and numerical optimization algorithms were applied. The goal was to examine the elastoplastic behaviour of the investigated thin film, which is the aluminium layer in this case. Various numerical material models were used in order to decently extract the material properties of the investigated thin layer.

Keywords: *nanoindentation; finite element method; thin film*

1. Introduction

The indentation technique was introduced for the first time in the 19th century. It was primarily used to measure hardness H of the material. Historically, the indentation was done by indenters of various shapes, thus leading to a variety of tests and analytical definitions of hardness. The indentation technique, called nanoindentation [1], was introduced in 1992 to examine mechanical properties such as elastic moduli E of investigated materials. Currently, the nanoindentation technique is used in microelectronics to examine properties of thin layers, which is an important issue in reliability analysis.

*Corresponding author, e-mail: artur.wymyslowski@pwr.wroc.pl

2. Nanoindentation

The nanoindentation technique [2] allows assessing Young's modulus of the indenting material. It requires a very precise tip shape, e.g. use of the Berkovich tip, and therefore assures high spatial resolutions [3] (Fig. 1a). It is based on an the analysis of real time load displacement during indentation, which identifies a loading and an unloading curve, as shown in Fig. 1b [4].

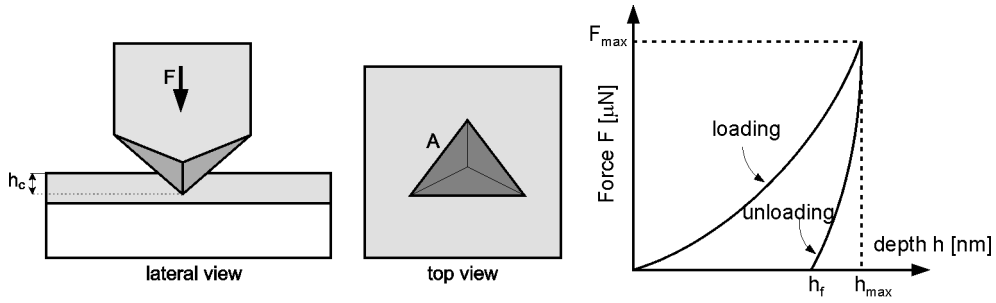

Fig. 1. The Berkovich nanoindentation test (a) and its result – the loading/unloading curve (b); $F/A = H_B \approx F/(24.56h_c)$, A – contact area, F – indenting force, H_B – hardness, h_c – contact depth

Taking into account the unloading nanoindentation curve it is possible to define and estimate the following elastic material properties [3, 5]:

- stiffness S

$$S = \left.\frac{dF}{dh}\right|_{F=F_{\max}} \tag{1}$$

where $F_{\max}$ is the maximum force during the loading and unloading indentation processes,

- hardness H

$$H = \frac{F_{\max}}{A_c} \tag{2}$$

where A_c is the contact area,

- effective modulus of elasticity E_{eff}

$$E_{\text{eff}} = \frac{\sqrt{\pi}}{2}\frac{S}{\sqrt{A_c}} \tag{3}$$

where the parameter E_{eff} is related to the deformation of both materials: specimen and indenter.

2.1. Software tool

In order to perform the requisite numerical analysis, appropriate software had to be developed. The main aim is to model the elastoplasticity of the material, using:

- Analytical algorithms, based on theoretically justified formulae. The benefit of analytical algorithms is that elastic properties such as Young's modulus, can be evaluated accurately. Unfortunately, the drawback is that it cannot be used to study the plasticity behaviour, except the yield strength in some specific cases.
- Optimization analysis combining numerical analysis with optimization algorithms. The goal is to determine the best data fit curves for the experimental measurements of nanoindentation. The data fit curves depend on the selected plasticity model. The benefit of such an approach is that the elastoplastic behaviour of the material can be described with reasonably good accuracy.

3. Results and analysis

The properties of a large number of materials used for microelectronic packaging can be precisely described by mathematical models of elasticity or elastoplasticity. Typical stress–strain models for elastic and elastoplastic materials are presented in Fig. 2.

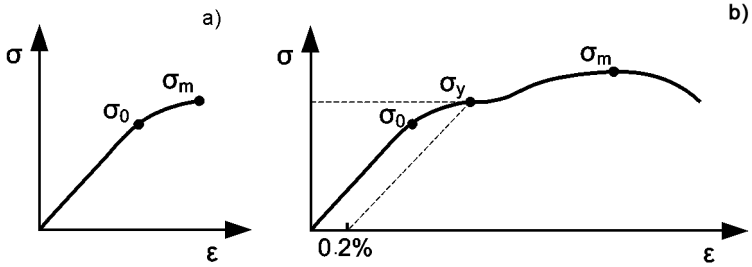

Fig. 2. The stress–strain curves for elastic (a) and elastoplastic (b) models

The research presented here focused on the mathematical description of the elastic and elastoplastic behaviour of specific materials. The above can be achieved by:

- analytical analysis, which uses the strict mathematical dependences in order to assess basic elastic properties of a material,
- numerical modelling, which uses finite element modelling (FEM) to describe the indentation loading and unloading curves, based on data obtained during the indentation tests.

3.1. Experimental setup

A hysitron triboindenter system, equipped with a Berkovich diamond indentation tip, was used for the experimental indentation procedure. The calibration of the system

and of the area function $A(h)$ was undertaken on a fused silica sample, based on the method of Oliver and Pharr [1]. Aluminium thin layers on a silicon substrate were indented with indenters of various loads and depths. The aluminium layer, 1 μm thick, was fabricated in an evaporation process. The loading and unloading curves for each sample were determined experimentally, by performing nanoindentation. One of the goals was to identify a mathematical model that would accurately describe the relationship between the indentation depth and the indentation force.

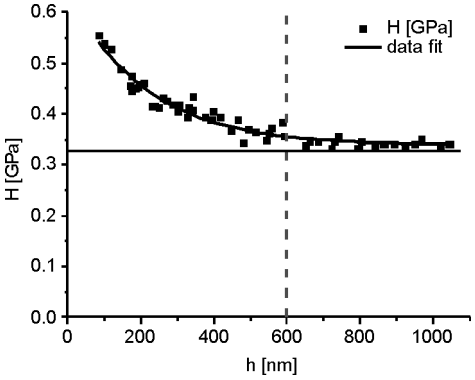

Fig. 3. Hardness H versus indentation depth h for aluminium thin layers

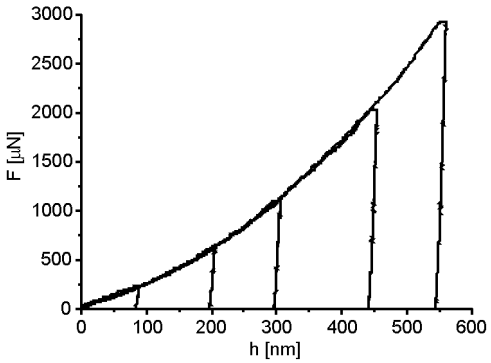

Fig. 4. Selected experimental results of loading and unloading indentation experiment for a thin layer of aluminum on silicon substrate

Classical analysis can describe elastic properties of a material such as the relationship between hardness H and indentation depth h, as shown in Fig. 3. As can be observed, material hardness should, and does, depend on the indentation depth. Despite the data scatter, hardness is clearly observed to decrease monotonically with respect to the indentation depth. Furthermore, the variation in the data measurements is clearly greater for thinner layers than for thicker ones. In fact, according to Fig. 3, the hardness measurements exhibit strong variation for indentation depths below 600 nm but are almost constant for indentation depths above 600 nm. This phenomenon is probably influenced by the presence of the substrate itself. In general, for indentation depths above 600 nm, the variations in the hardness data over the whole 1 μm thick layer are "flattened" by the interaction with the substrate. This clearly indicates the depth dependence of hardness and probably of other mechanical properties too such as Young's modulus or Yield stress for small indentation depths, e.g. below 600 nm in case of 1 μm aluminium layers.

In order to verify the most appropriate material model and corresponding properties for low indentation depths, a number of nanoindentation experiments were made using aluminium thin layers on silicon substrate. The selected results for the indentation depths lower than 600 nm are given in Fig. 4.

The experiments were then analysed numerically. In fact, the experimental results were the starting point to the numerical analysis. In order to extract the material properties, a global optimization algorithm based on simulated annealing with defined constraints technique was applied. In fact, the authors tested a number of optimization algorithms from local methods to global ones of which the simulated annealing seemed to be the most efficient and accurate.

3.2. Numerical modelling

A number of problems in contemporary engineering can be solved by numerical modelling. There are a number of modelling techniques but the analysis presented here exploits the FEM method, using ANSYS v.11. In fact, FEM models and data analysis of nanoindentation experiments can accurately describe the loading and unloading stages. One of the benefits of FEM models is they can exploit different mathematical models of materials. For example, they are suitable for investigating elasticity, elastoplasticity, or even viscoelasticity, with or without the hardening effect. In addition, it can be used to simulate nanoindentation, either using 2D or 3D models. Based on several numerical experiments, it was found that 2D axisymmetric numerical models are precise enough to simulate nanoindentation. Figure 5a shows an example of a 2D FEM model, and in Fig. 5b corresponding experimental data are shown and the data fit curve provided by numerical analysis.

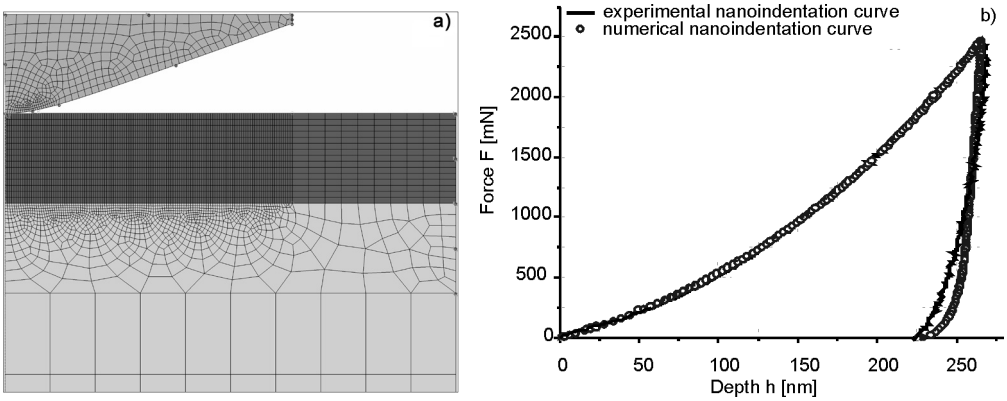

Fig. 5. The 2D numerical model of a nanoindentation test (a) and corresponding experimental and numerical results (b)

A numerical model with adjustable parameters was designed. In particular, it facilitates a systematic investigation of geometric features, for example thickness of a thin layer and indenter shape can be modelled by adjusting the area function coefficients. Thus, the numerical model can be adjusted to the actual geometry of the experimental indentation process. The results of numerical modelling are in very close agreement with the theoretical predictions.

As mentioned earlier, numerical analysis requires an optimization algorithm to find the best data fit, as shown in Fig. 5b. Many local and global optimization algorithms are available; the authors used simulated annealing, which, in their opinion, lead to the most efficient and accurate fitting [7]. The above procedure combining numerical modelling, experimental results and optimization algorithm finely allowed one to extract the most appropriate elastoplastic material model and corresponding properties.

Three models of elastoplastic materials were selected:

- bilinear response without hardening defined by two parameters: Young's modulus E and yield stress σ_y,
- bilinear response with hardening defined by three parameters: Young's modulus E, yield stress σ_y, and tangent modulus E_y,
- non-linear response with hardening, corresponding to the true stress–strain curve defined by the Ramberg–Osgood dependence [6]. Its three adjustable parameters satisfy the following equation:

$$\varepsilon = \frac{\sigma}{E} + K\left(\frac{\sigma}{E}\right)^n \tag{4}$$

where the total strain ε is a function of stress σ; it depends on Young's modulus E as well as on the constant K and exponent n which describe the plastic hardening of the material.

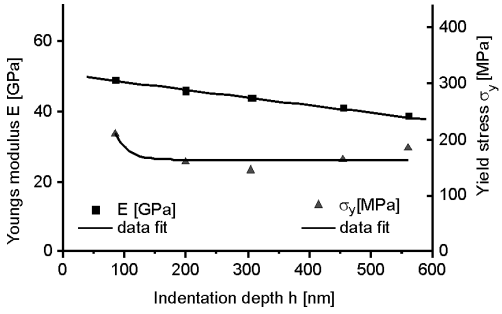

Fig. 6. Data fit curves for the bilinear model without hardening, showing Young's modulus E and Yield stress σ_y as functions of the indentation depth h in the case of a thin layer of aluminium

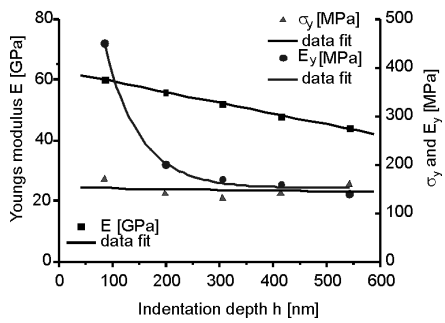

Fig. 7. Data fit curves for the bilinear model with hardening describing Young's modulus E, yield stress σ_y and tangent modulus E_y as functions of the indentation depth h in the case of an aluminium thin layer

The data-fit curves for the bilinear model of elastoplasticity without hardening, describing Young's modulus E and Yield stress σ_y in functions of the indentation depth h, are shown in Fig. 6. Young's modulus E decreases linearly upon increasing the indentation depth h, whereas the yield stress σ_y is observed to decay non-linearly for small depths, but then it levels off to a constant value of about 150 MPa for higher depths.

The data fit curves for the bilinear model of elastoplasticity with hardening, describing Young's modulus E, yield stress σ_y and tangent modulus E_y in functions of the indentation depth h, are given in Fig. 7. The model is characterised by monotonically decreasing functions of the indentation depth h. One of the advantages of the model is that the values for Young's modulus E are higher and more realistic. Unfortunately, similarly to the previous model, it seems to be inappropriate for accurate analysis of thin aluminium layers.

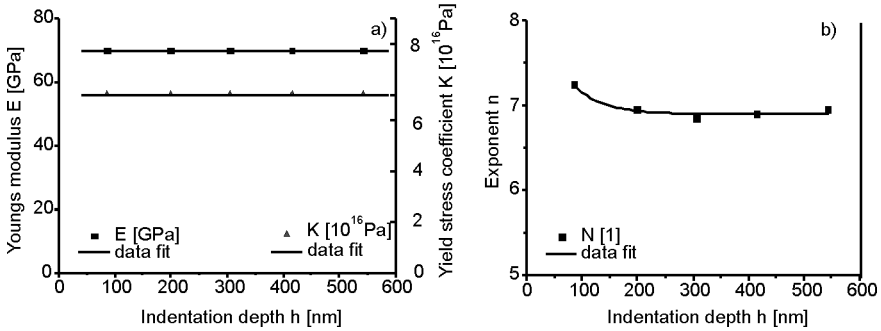

Fig. 8. Data fit curves for the non-linear, Ramberg–Osgood model without hardening, describing Young's modulus E, constant K (a), and the exponent n (b), as functions of the indentation depth h, for thin layer of aluminum

The data-fit curves corresponding to the Ramberg–Osgood model for an elastoplastic material, describing Young's modulus E, constant K and exponent n in functions of the indentation depth h, are given in Fig. 8. The results were obtained under the assumption that Young's modulus E is close to 70 GPa while the constant K is close to 7×10^{16}. The only adjustable parameter in that experiment was the exponent n. Putting all this information together, and substituting these values into the non-linear Ramberg–Osgood equation (Eq. (4)), leads to an elastoplasticity model for the material (Fig. 9).

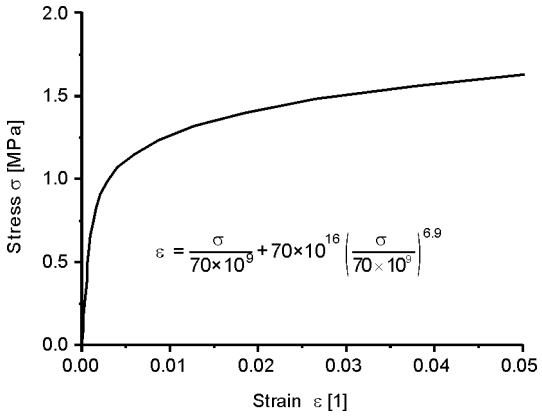

Fig. 9. The stress vs. strain curve for thin aluminium layers, according to the Ramberg –Osgood model, using average values for the model parameters E, K and n

Another benefit of the above model is that it implies plastic strain even at very small stress levels, making this approach more expressive than a bilinear elastoplasticity law, when it is applied in a Coffin–Manson type relation for life testing analysis.

4. Conclusions

Current developments and trends in microelectronics are focused on thin layers and novel materials. This led to application of various tests and measurement methods, capable of determining basic mechanical properties of such materials on both the microscale and the nanoscale. The project presented in this paper focuses on the nanoindentation technique. The specific aim was to describe, both numerically and theoretically, the dynamics of elasticity and elastoplasticity in aluminium. Several mathematical models were considered: the results of tests showed the Ramberg –Osgood model provided the most accurate description of elastoplasticity in the considered material. Furthermore, the Ramberg–Osgood model provides an accurate description of what occurs when very thin aluminium layers are subjected to nanoindentation; it shows, e.g., that the Young's modulus is of the order of 70 GPa, which corresponds well with aluminium bulk properties. The model is described by three variables, whose values appear to be almost constant over the investigated range of indentation depths h. Finally, it should be possible to exploit the Ramberg–Osgood model to predict the response of the material over a wide range of indentation depths.

References

[1] OLIVER W.C., PHARR G.M., J. Mater. Res., 7 (1999), 12564.
[2] VENKATESH T.A., VAN VLIET K.J., GIANNAKOPOULOS A.E., SURESH S., Scripta Mater., 42 (2000), 833.
[3] FISCHER-CRIPPS A.C., *Nanoindentation*, Springer, New York, 2004.
[4] GIANNAKOPOULOS A.E., SURESH S., Scripta Mater., 40 (1999), 1191.
[5] DOERNER M.F., J. Mater. Res., 1 (1986), 601.
[6] XIAODONG L., BHARAT B., Mater. Charact., 42 (2002), 11.
[7] WYMYSŁOWSKI A., WITTLER O., MROSSKO R., DUDEK R., *Application of nanoindentation technique in microelectronics*, Int. Conf. IMAPS – CPMT, IEEE Poland, 2008.

Received 27 June 2009
Revised 29 September 2010

Materials Science-Poland, *Vol. 28*, *No. 3*, *2010*

Fabrication and thermal properties of Al_2TiO_5/Al_2O_3 composites

M. LI, F. CHEN, Q. SHEN*, L. ZHANG

State Key Lab of Advanced Technology for Materials Synthesis and Processing,
Wuhan University of Technology, Wuhan 430070, China

Al_2TiO_5/Al_2O_3 composites with various Al_2O_3 contents were prepared. The phase compositions and microstructure evolution of the samples were observed via XRD and SEM, respectively. The thermal properties, including thermal expansion ratios and the erosion resistance of the Al_2TiO_5/Al_2O_3 composites to molten Al, were investigated. The experimental results show that the relative densities of the prepared Al_2TiO_5/Al_2O_3 composites are proportional to the Al_2O_3 content, and that the composite samples with high Al_2TiO_5 contents have good erosion resistance to molten Al.

Keywords: *Al_2TiO_5/Al_2O_3 composites; microstructure; thermal expansion ratio; erosion resistance to molten Al*

1. Introduction

Aluminum titanate (Al_2TiO_5) ceramics has some superior thermal properties such as low thermal expansion and thermal conduction coefficients, high melting point, high resistance to corrosion and thermal shock resistance [1–3], thus making it one of the best candidates for thermal and structural applications. However, there are two major disadvantages of $A1_2TiO_5$ ceramics, which limit the scope of its applications. Firstly, $A1_2TiO_5$ ceramics is susceptible to extensive microcracking which contributes to its low thermal expansion coefficient and results in its very low mechanical strength. Secondly, $A1_2TiO_5$ ceramics decomposes to Al_2O_3 and TiO_2 in the temperature range of 750–1300 °C [4, 5] which severely limits its structural applications. Thus, some research has focused on the improvement of $A1_2TiO_5$ ceramics [6–8]. It has been reported that thermal decomposition of Al_2TiO_5 can be prevented by some oxide additives such as Al_2O_3, SiO_2, MgO, Fe_2O_3, ZrO_2, $FeTiO_3$, etc. [9, 10] due to the formation of solid solutions.

*Corresponding author, e-mail: sqqf@263.net

In order to explore an efficient way of solving the above two problems, in the present paper alumina (Al_2O_3) was introduced in order to suppress the decomposition of $A1_2TiO_5$ ceramics. Furthermore, Al_2TiO_5/Al_2O_3 composites were experimentally designed and fabricated in order to obtain a ceramic material which has greater mechanical strength than Al_2TiO_5 ceramics.

In particular, as-prepared Al_2TiO_5/Al_2O_3 composites have been used as containers or pipes to transport molten Al; in such applications, Al_2TiO_5/Al_2O_3 composites are in contact with molten Al for a long time. Thus, investigation of thermal properties, including thermal expansion and erosion resistance of Al_2TiO_5/Al_2O_3 composites to molten Al, was also carried out.

2. Experimental

Raw materials used in this paper were: α-Al_2O_3 (Taimei Chemical Co., Ltd., Japan), anatase-TiO_2 (Guangdong Orient Ind. Sci. & Tech. Co., Ltd., China), MgO (Tateho Chemical Ind. Co., Ltd., Japan) and Fe_2O_3 (Taimei Chemical Co., Ltd., Japan). The characteristic features of the raw materials are shown in Table 1.

Table 1. Characteristic features of the raw materials

Material	Mean particle size [μm]	Purity	Density [g/cm^3]
α-Al_2O_3	1.5	≥ 99%	3.99
Anatase–TiO_2	0.3		4.25
MgO	1.0		3.58
Fe_2O_3	1.0		5.37

In accordance with the design prescription shown in Table 2, raw powders of various volume ratios were fabricated by mixing them uniformly in a three dimensional mixing facility for 5–7 h. The mixtures were then loaded in a die, having an inner diameter of 50 mm, and pre-pressed under 10 MPa for 1 min. After cold isostatic pressing (CIP) at 200 MPa, the samples were sintered for 2 h at 1450 °C, using an electric furnace. Finally, the samples were cooled down, in the furnace, to room temperature.

Table 2. Design prescription for the specimens

Sample No.	Volume ratio [%]			
	Anatase-TiO_2	α-Al_2O_3	MgO	Fe_2O_3
1	88	10	1.5	0.5
2	78.4	20	1.2	0.4
3	58.8	40	0.9	0.3
4	39.2	60	0.6	0.2
5	19.6	80	0.3	0.1
6	9.8	90	0.15	0.05

After preparation, the bulk densities of the sintered products were determined according to Archimedes' principle, using distilled water. The phase compositions were analyzed by X-ray diffraction (XRD) using a Rigaku-D/Max-IIIA diffractometer with Cu radiation at 40 kV and 50 mA. The scanning rate of 10 °/min was used to record the diffraction patterns in the 2θ range between 10° and 80°. The microstructure of the fractured surface of the prepared samples was observed by scanning electron microscopy (SEM). The samples were machined into bars of the dimensions 3 mm×4 mm ×35 mm. After polishing, the bars were soaked in a crucible filled with molten Al. After having been maintained at a temperature of 750 °C for 100 h, the samples were cooled in air. The lining and elemental distribution mapping were studied by electron probe microanalysis (EPMA).

3. Results and discussion

3.1. Phase compositions of the Al_2TiO_5/Al_2O_3 composites

In accordance with the design specifications shown in Table 2, the obtained Al_2TiO_5/Al_2O_3 composites were composed of Al_2TiO_5 solute with 5 mol % of $MgTi_2O_5$ and 1 mol % of Fe_2TiO_5 composites and Al_2O_3. The reactions for the formation of $MgTi_2O_5$ and Fe_2TiO_5 can be described by the following two equations:

$$MgO + 2TiO_2 = MgTi_2O_5 \quad (1)$$

$$Fe_2O_3 + TiO_2 = Fe_2TiO_5 \quad (2)$$

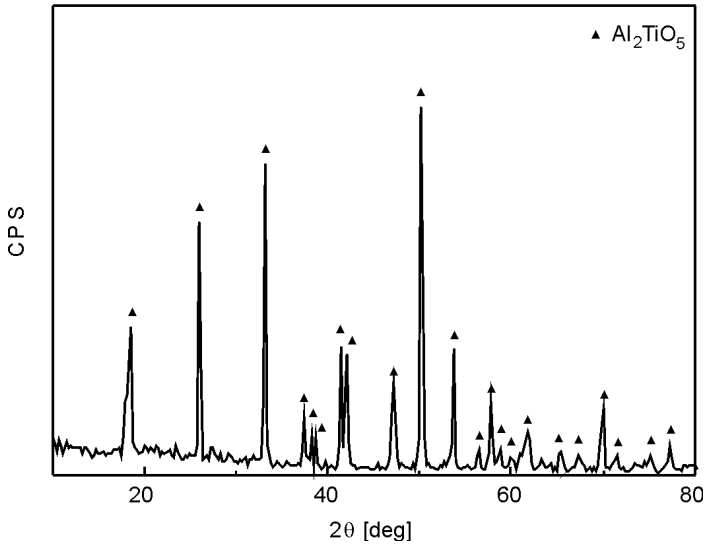

Fig. 1. XRD patterns of the Al_2TiO_5 sample with 5 mol % of $MgTi_2O_5$ and 1 mol % of Fe_2TiO_5 sintered at 1100 °C for 50 h

The XRD patterns of the Al_2TiO_5 sample with 5 mol % of $MgTi_2O_5$ and 1 mol % of Fe_2TiO_5 sintered at 1100 °C for 50 h are shown in Fig. 1. It is clearly visible that all the diffraction peaks are related to Al_2TiO_5. No other phase was detected by XRD, indicating that the composite solute consisted of 5 mol % of $MgTi_2O_5$ and 1 mol % of Fe_2TiO_5, and that the decomposition of Al_2TiO_5 can be effectively suppressed by using $MgTi_2O_5$ and Fe_2TiO_5 as the composite additives.

3.2. Densities and microstructures of the Al_2TiO_5/Al_2O_3 composites

Densities of the sintered Al_2TiO_5/Al_2O_3 composites are shown in Fig. 2. It is clearly seen that both the density and relative density are proportional to the Al_2O_3 content. The density reaches the maximum value of 3.86 g/cm^3 for the sample containing 90 wt. % of Al_2O_3, while the density reaches the minimum value of 3.51 g/cm^3 for the sample containing 10 wt. % of Al_2O_3. The reason is that Al_2TiO_5 is very difficult to fully dense sinter and its density is very low, while Al_2O_3 can easily be densified and has a higher density than Al_2TiO_5. As a result, both the densities and relative densities of the obtained Al_2TiO_5/Al_2O_3 composites are proportional to the Al_2O_3 content.

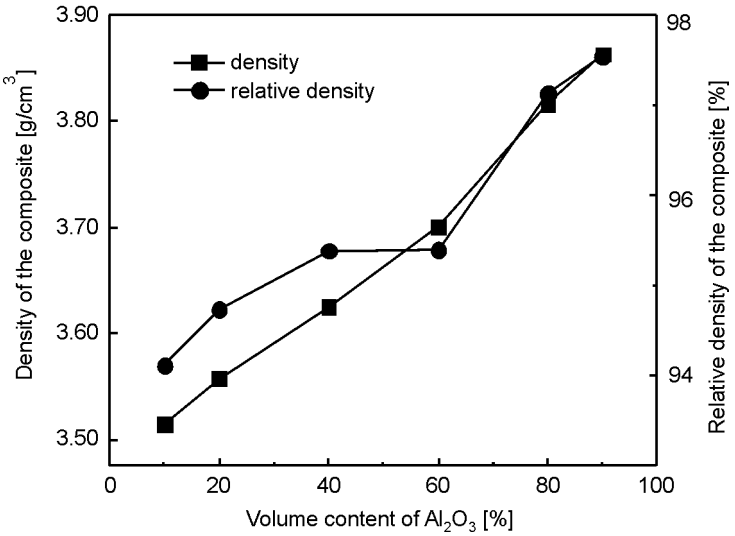

Fig. 2. Density and relative density of the obtained Al_2TiO_5/Al_2O_3 composites in function of the Al_2O_3 content

SEM images of the sintered Al_2TiO_5/Al_2O_3 composites are shown in Fig. 3. The sample with the Al_2O_3 content of 10 vol. % experiences significant grain growth (Fig. 3a); its grain size (after sintering) is ca. 20 μm. There are some pores in this sample, resulting in the incompact structure between the grains, which explains the low relative density shown in Fig. 2. It is also in Figs. 3a–f that the the grain size is inversely proportional to the Al_2O_3 content, and the number of pores decreases gradu-

ally as the Al_2O_3 content increases. When the Al_2O_3 content is higher than 40 vol. %, as shown in Figs. 3c, 3d, the average grain size of the sintered samples is lower than 5 μm,

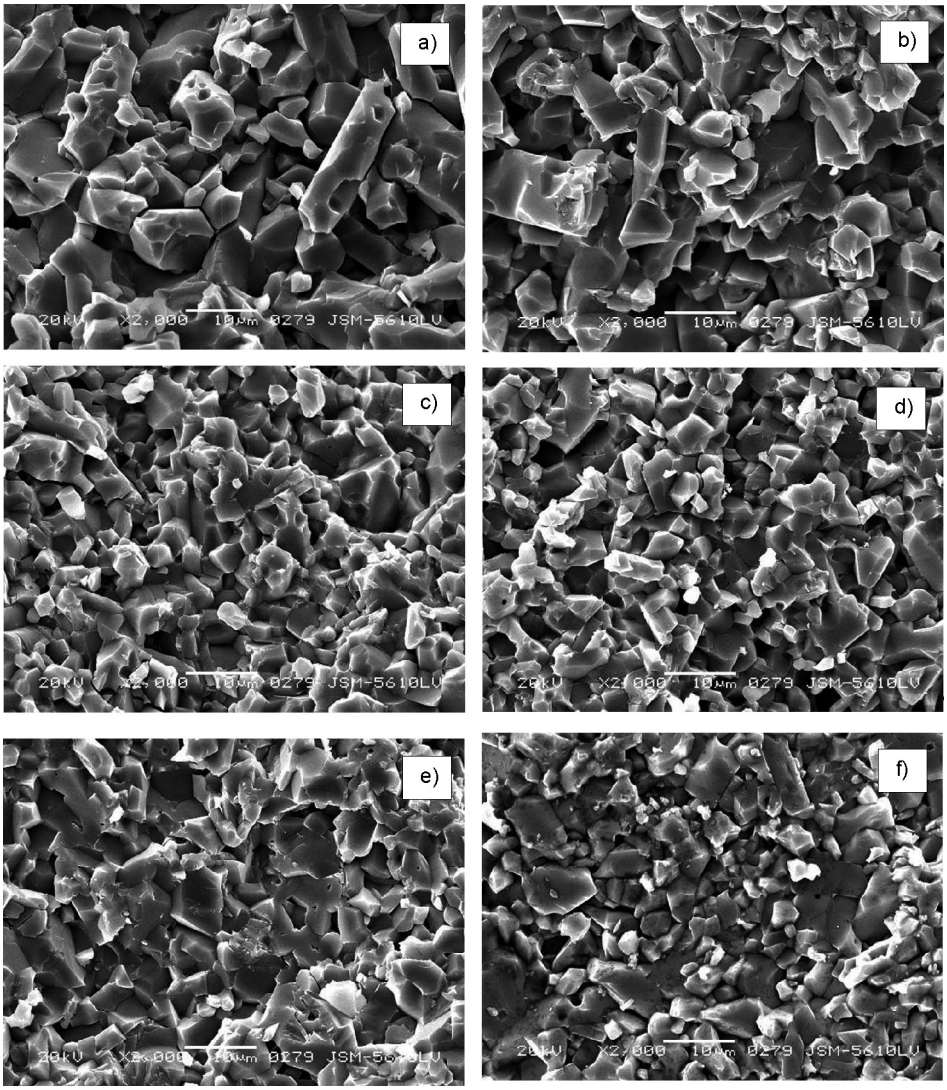

Fig. 3. SEM images of the Al_2TiO_5/Al_2O_3 composites with various Al_2O_3 contents: a) 10 vol. %, b) 20 vol. %, c) 40 vol. %, d) 60 vol. %, e) 80 vol. %, f) 90 vol. %

which is almost the same as the grain size of the raw Al_2O_3 powder. When the Al_2TiO_5 content is almost the same as the Al_2O_3 content, it is the Al_2TiO_5 that prevents further growth of grains of Al_2O_3. When the Al_2O_3 content is higher than 80 vol. %, as shown in Figs. 3e and 3f, the amount of Al_2TiO_5 is too small to prevent the growth of grains of the Al_2O_3, and as a result, many large Al_2O_3 grains can be observed in the SEM

images. However, hardly any pores at all can be observed, indicating the samples are fully dense sintered. It can be concluded from these images that the density of a sintered sample is proportional to the Al_2O_3 content, whereas the porosity is inversely proportional to the Al_2O_3 content, which is quite in agreement with the intrinsic sintering behavior of Al_2TiO_5 and Al_2O_3: Al_2TiO_5 is very difficult to be fully dense sintered while Al_2O_3 can be sintered easily with high density.

3.3. Thermal expansion of the Al_2TiO_5/Al_2O_3 composites

Al_2TiO_5 has a very low thermal expansion coefficient, and thus very good thermal shock resistance. The thermal expansion ratios of the sintered Al_2TiO_5/Al_2O_3 composites having different Al_2O_3 contents are shown in Fig. 4.

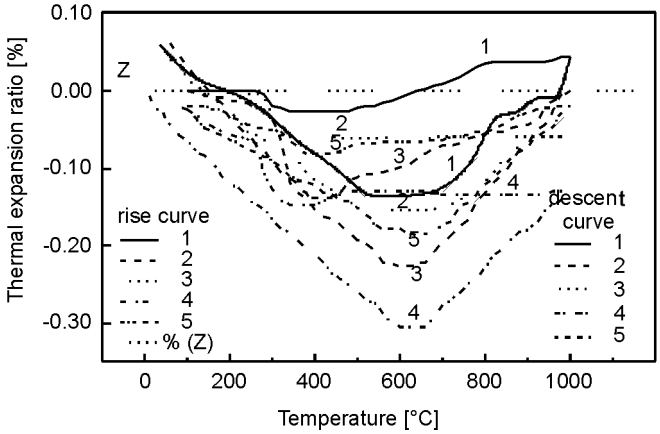

Fig. 4. Thermal expansion ratios of the Al_2TiO_5/Al_2O_3 composites with various Al_2O_3 contents

The thermal expansion ratios of all the samples firstly increase and then decrease as the temperature increases during the heating process, and they firstly decrease and then increase as the temperature decreases during the cooling process. Al_2TiO_5 crystals are composed of crystal domains, and the adjacent crystal domains have different orientations. As a result, the thermal expansion ratio of Al_2TiO_5 is anisotropic. Thus, during the cooling process, an individual crystal domain of the Al_2TiO_5 shrinks, which causes the anisotropy and the formation of the microcracks in the crystal domains. On the other hand, during the heating process, the individual crystal domain of Al_2TiO_5 expands, but the presence of the microcracks prevents the expansion of the crystal domains. As a result, no obvious expansion is seen between room temperature and 700 °C (see Fig. 4). Moreover, with the increase in the temperature, the microcracks among the crystal domains are totally repaired, no extra porous area exists for the expansion, and as a result, the thermal expansion ratio is increased, which is in close agreement with the results shown in Fig. 4.

3.4. Erosion resistance of Al_2TiO_5/Al_2O_3 composites to molten Al

The elemental distribution along the cross-section of a sample of Al_2TiO_5/Al_2O_3 composite containing 20 vol. % of Al_2O_3, after the sample had been soaked in molten Al and cooled in the furnace, was observed by EPMA, as shown in Fig. 5. It is completely obvious from Fig. 5a that a definite interface exists between Al and Al_2TiO_5/Al_2O_3 composites, and nearly no gradient distribution of Al and Ti elements is observed along the thickness direction according to the Al and Ti line distribution characterization, as shown in Fig. 5b. Moreover, the results of lining analysis of Al and Ti elements show that the thickness of Al atomic diffusion is only 10 μm, indicating that Al_2TiO_5/Al_2O_3 composites with high Al_2TiO_5 content have good errosion resistance to molten Al.

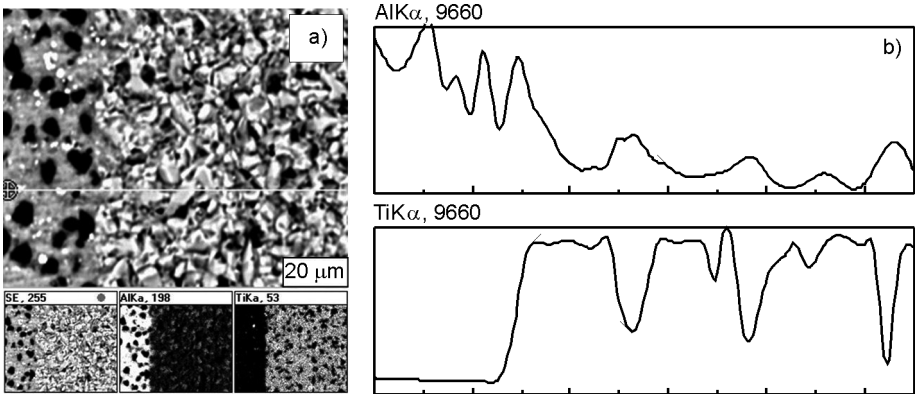

Fig. 5. Back-scattered electron image of a composite sample soaked in molten Al (a) and the lining distribution of Al and Ti along the thickness of the sample

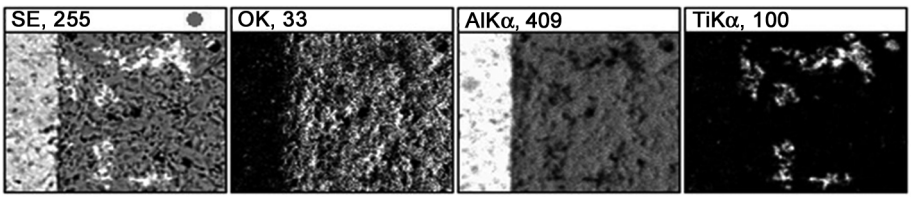

Fig. 6. Elemental distribution of O, Al and Ti along the thickness of the sample

The elemental distribution along the cross-section of a sample of Al_2TiO_5/Al_2O_3 composite having 80 vol. % of Al_2O_3, after the sample had been soaked in molten Al and cooled in the furnace, was observed by EPMA, as shown in Fig. 6. It is clearly evident that there is also a definite interface between the Al and Al_2TiO_5/Al_2O_3 composites having a low Al_2TiO_5 content. However, some molten Al can be seen to penetrate the main body of the material, as shown in Fig. 7. The reason is that when the sample is rapidly heated in molten Al, high thermal stress is induced on the surface of the sample.

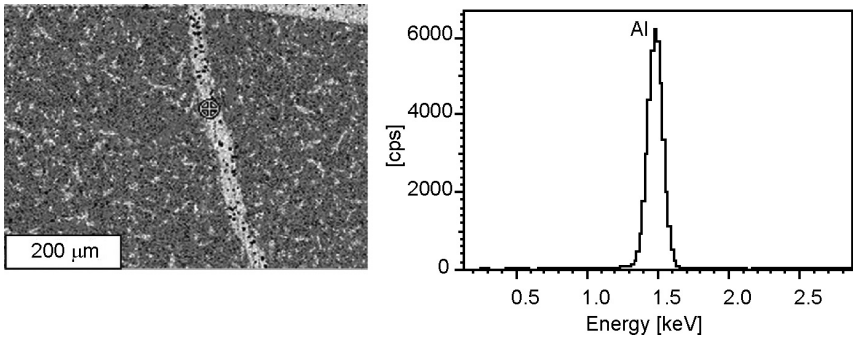

Fig. 7. Back-scattered electron image of a composite sample soaked in molten Al

On the other hand, if the sintered sample has a high Al_2O_3 content, it can have a high relative density, few cracks and low porosity; and these are properties which lead to rapid cracking. Existing cracks become expanded when they are infiltrated with molten Al, and some cracks run through the whole sample, resulting in severe structural damage to the material, indicating that Al_2TiO_5/Al_2O_3 composites with low Al_2TiO_5 content have poor erosion resistance to the molten Al.

4. Summary

Al_2TiO_5/Al_2O_3 composites with different Al_2O_3 contents were prepared, using Al_2O_3, TiO_2, MgO and Fe_2O_3 as the starting powders and by performing pressureless sintering. Some dramatic conclusions follow from the results of our experiments:

- Relative densities of the sintered materials are proportional to the Al_2O_3 content.
- The thermal expansion ratios of the Al_2TiO_5/Al_2O_3 composites are anisotropic.
- As Al_2TiO_5 has a very low thermal expansion coefficient, and very good thermal shock resistance, the thermal shock and the erosion resistances of the Al_2TiO_5/Al_2O_3 composites to molten Al can be improved by increasing the Al_2TiO_5 content.

References

[1] URIBE R., BAUDIN C., J. Am. Ceram. Soc., 86 (2003), 846.
[2] CHEN C. H., AWAJI H., J. Eur. Ceram. Soc., 27 (2007), 13.
[3] KIM I., ZHAO F., GONG J., LEE K., HAN I., KUK W., J. Ceram. Proc. Res., 4 (2003), 71.
[4] MORSIN B., LYNCH R., Acta Cryst. B, 28 (1972), 1040.
[5] HUANG Y., SENOS A., BAPTISTA J., J. Mater. Res., 15 (2000), 357.
[6] PARK S., JUNG S., CHUNG Y., Ceram. Inter., 29 (2003), 707.
[7] YOUSEFI M., ALIZADEH P., YEKTA B., MOLAIE F., GHAFOORIAN N., MONTAZERIAN M., Ceram. Inter., 35 (2009), 1447.
[8] XU G., TU C., WENG W., Key Eng. Mater., 336–338 (2007), 1327.
[9] OHYA Y., NAKAGAWA Z., J. Mater. Sci., 31 (1996), 1555.
[10] FREUDENBERG B., MOCELLIN A., J. Mater. Sci., 25 (1990), 3701.

Received 13 October 2010

Materials Science-Poland, *Vol. 28*, *No. 3*, *2010*

A novel conversion of inert carbon nanotubes to highly dispersed fibres

X. TANG, Y. ZHAO, Q. JIAO*, Y. CAO

School of Chemical Engineering and the Environment,
Beijing Institute of Technology, Beijing 100081, P. R. China

Multiwalled carbon nanotubes were functionalized with alkyl groups and transformed to form highly dispersed carbon nanofibres (CNFs) in ethylenediamine via the Benkeser reaction. The functionalized CNFs were characterized by transmission electron microscopy, scanning electron microscopy, Raman, infrared spectroscopoy as well as thermogravimetric analysis. The functionalized CNFs with long alkyl chains can be highly dispersed in universal solvents such as ethanol, toluene and N, N-dimethylformamide. The conversion mechanism has been investigated and the electrophilic reagents were proposed as key factors affecting the conversion degree.

Keywords: *carbon nanotubes; carbon nanofibres; characterization methods; functionalization*

1. Introduction

Carbon nanotubes (CNTs) are of great interest, stemming from their extraordinary structural, electronic and mechanical properties [1–3]. Many applications based on this unique material have been proposed such as mechanically reinforced composites [4], field-emission transistors [5], bio- and chemical sensors [6], and many others [7, 8]. In order to realize these potential applications, chemical modifications [9–13] to the surface of CNTs should be performed, to improve their solubility and dispersion in solvents. Over the past few years, many chemical reactions have emerged in the sidewall or endcap functionalization of CNTs; a subject having been extensively reviewed [14–16].

Recently, the chemical functionalization of CNTs using the Benkeser reaction was studied and single-walled carbon nanotubes (SWNTs) with alkyl and aryl groups have been successfully functionalized in ethylenediamine, which undergoes a convenient, scalable and moderate process [17]. In contrast with SWNTs, multiwalled carbon nanotubes (MWNTs) are easier to produce, more economical and have been widely

*Corresponding author, e-mail: jiaoqz@bit.edu.cn

used in large-scale consumer applications such as CNT-reinforced polymer composites [18]. Herein, this convenient route has been extended to the functionalization of MWNTs. Fortunately, inert MWNTs can also be functionalized with alkyl groups under Benkeser's condition. It is very interesting that in this reaction most of the MWNTs are transformed into disordered carbon nanofibres (CNFs) which also show good dispersibility in common solvents. To the best of our knowledge, this novel conversion has not been reported in other chemical reactions involving CNTs [9–16].

2. Experimental

In a typical experiment, 30 mg of MWNTs and 40 cm^3 of ethylenediamine were mixed in a flask. The mixture was rigorously stirred under argon at ambient temperature. After 20 min, when the solution became visually homogeneous, pieces of lithium (100 mg) were added in batches until the dark blue colour disappeared. Then hexadecyl iodide was added dropwise to the mixture. The reaction mixture was then stirred for about 3 h. The resulting dark solution was diluted with ethanol, followed by filtering over a 0.2 μm polycarbonate membrane. The dark solid obtained was washed thoroughly with ethanol and deionized water, and dried overnight in a vacuum oven at 80 °C to produce the functionalized product (30 mg).

A comparative experiment was conducted, and followed the same reaction procedure as earlier, except for the substitution of *tert*-butanol for hexadecyl iodide. The product was isolated as a black solid (30 mg).

Raman spectra were acquired using a Renishaw in via-reflex Raman microscope with a laser light wavelength of 532 nm. Fourier transform infrared (FTIR) data were recorded on a Perkin Elmer FTIR spectrometer. Thermogravimetric analyses (TGA) were carried out on a Pyris-1 thermogravimetric analyzer (Perkin Elmer, USA) with the heating rate of 10 °C/min and in nitrogen diluted air atmosphere. TEM images were obtained on a JEM-1200EX electron microscope operating at an accelerating voltage of 100 kV. HRTEM images were acquired using a JEM 2010 high resolution transmission electron microscope at the accelerating voltage of 120 kV.

3. Results and discussion

MWNTs were subjected to Benkeser reduction conditions in ethylenediamine, with an excess of hexadecyl iodide as the electrophile. The morphology of the MWNTs before and after the reaction was investigated by high resolution transmission electron microscopy (HRTEM) and scanning electron microscopy (SEM). As shown in Figs. 1 and 2, pristine MWNTs (p-MWNTs) show a smooth tube structure with regular graphite sheets. However, the hexadecylated products exhibit a disrupted structure with disordered carbon nanofibre features wrapped by some amorphous materials, which can be ascribed to the organic groups covalently attached to their sidewalls. Nearly all of the hexadecylated products observed display these new fibre fea-

tures; they have an average diameter of 15–25 nm and lengths ranging from hundreds of nanometers to micrometers (Figs. 1, 2).

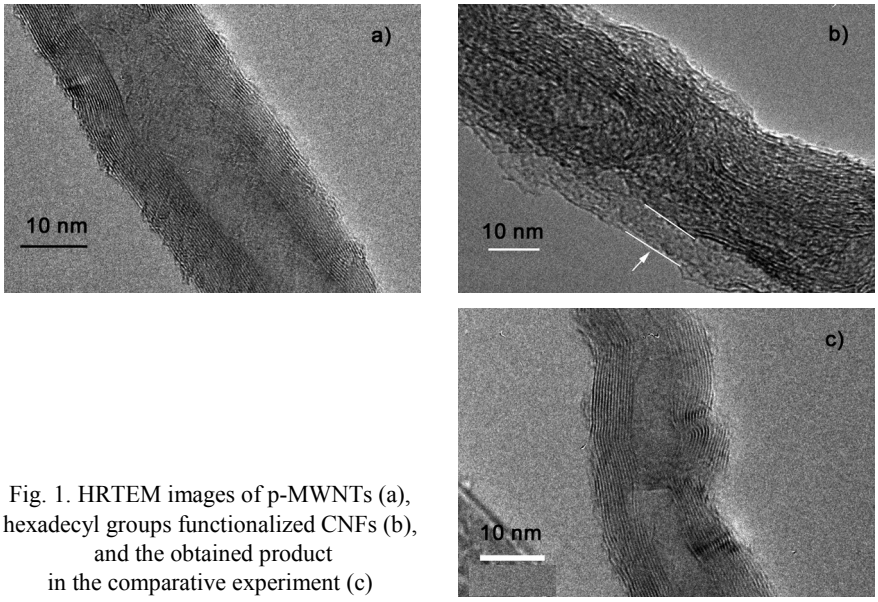

Fig. 1. HRTEM images of p-MWNTs (a), hexadecyl groups functionalized CNFs (b), and the obtained product in the comparative experiment (c)

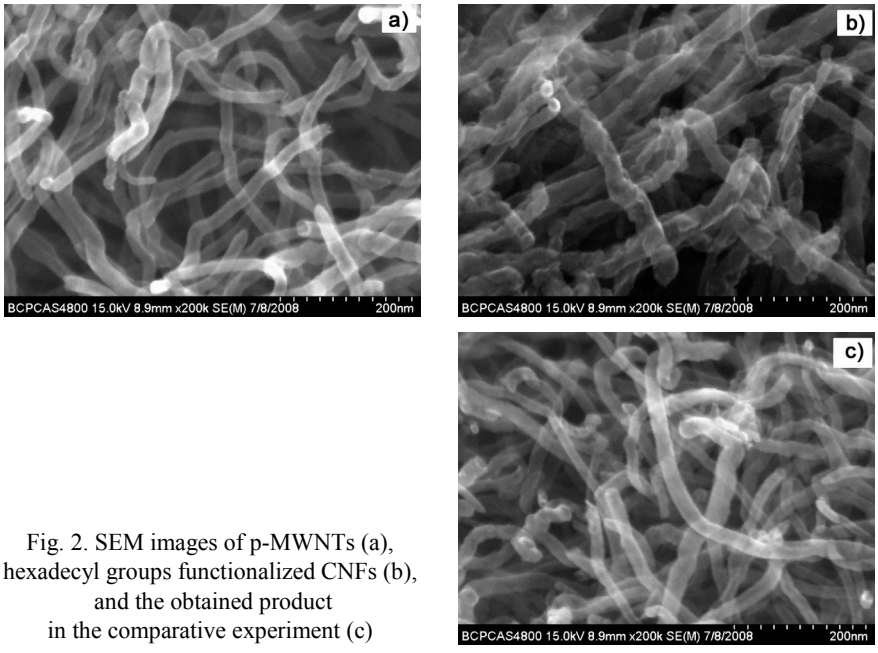

Fig. 2. SEM images of p-MWNTs (a), hexadecyl groups functionalized CNFs (b), and the obtained product in the comparative experiment (c)

The functionalization and morphological transformation was confirmed by Raman spectra (Fig. 3a). The intensity ratio of the disorder band (D band) to the tangential

band (G band) (I_D/I_G) for p-MWNTs and hexadecyl groups functionalized carbon nanofibres (f-CNFs) was increased from 0.77 to 1.17. This significant enhancement of the I_D/I_G ratio is related to the presence of defects, as well as of nanoparticles and amorphous carbon in the functionalized product which resulted from the reduced Benkeser procedure. Additionally, the linewidth of the D band is also broadened at about 50 cm^{-1} as compared with those of p-MWNTs, which further suggests the formation of CNFs [19–21] , and is in agreement with the HRTEM observations.

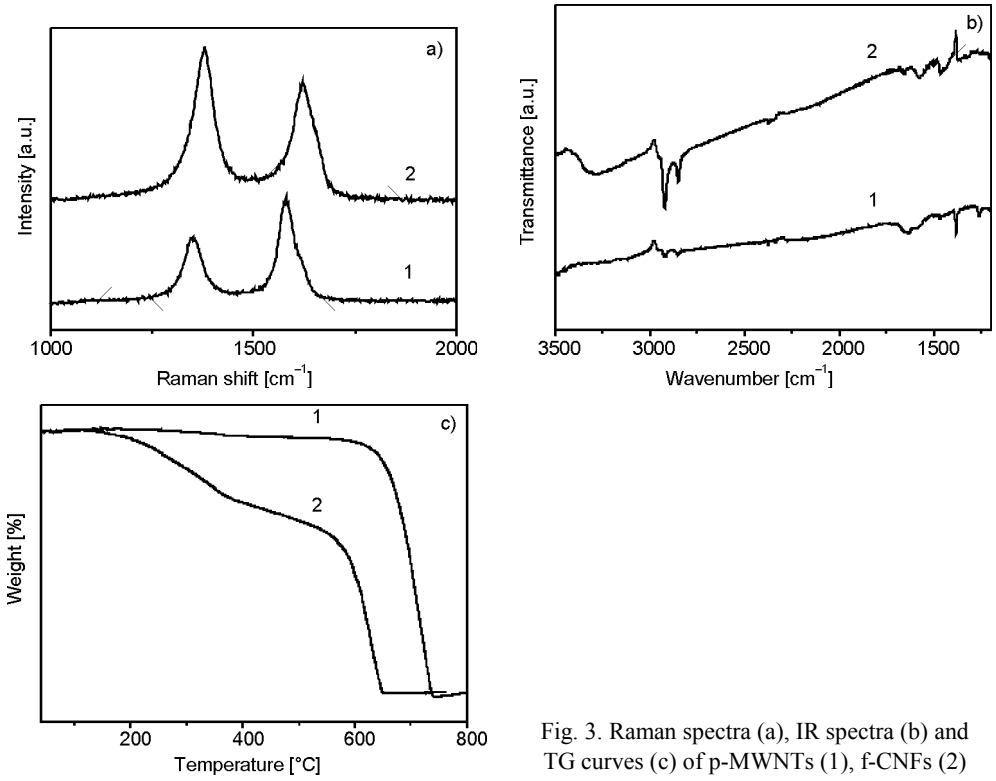

Fig. 3. Raman spectra (a), IR spectra (b) and TG curves (c) of p-MWNTs (1), f-CNFs (2)

The obtained f-CNFs were further characterized by IR spectroscopy (Fig. 3b). The f-CNFs show typical C–H stretching modes at 2920, 2850 cm^{-1}, as well as a C–H deforming mode at 1460 cm^{-1}: these were not found in the p-MWNTs and should come from the long hexadecyl groups attached to the sidewall of the CNFs. Since the reduced product was functionalized with hexadecyl groups, the surface property of f-CNFs could be altered significantly, which was confirmed by the dispersion measurements. As expected, f-CNFs exhibit good dispersibility in toluene, N, N-dimethylformamide (DMF) and ethanol. Figure 4 shows the dispersed states of the p-MWNTs and f-CNFs via sonication for 3 min in these solvents. Dispersed p-MWNTs are easily aggregated, however, f-CNFs are stable as homogeneous black suspensions. As is

known, highly dispersed f-CNFs can also be used as excellent polymer fillers in the field of polymer nanocomposites [22, 23].

The TGA curve (Fig. 3c) of the f-CNFs reveals a 23% weight loss in the range of 200 to 400 °C, which can be attributed to the decomposition of the functionalized hexadecyl groups. The ratio of carbon to hexyadecyl group is estimated to be 62:1, which is identical to that of dodecyl groups functionalized MWNTs reported by Tour et al. [12]. The temperature ascribed to the decomposition of their own structural backbone for f-CNFs is in the range of 550–650 °C, and that is much lower than the corresponding range for p-MWNTs, which is about 600-740 °C. This indicates that the obtained f-CNFs have poor thermal stability. It also provides further evidence of the structural alteration of MWNTs during this Benkeser reaction.

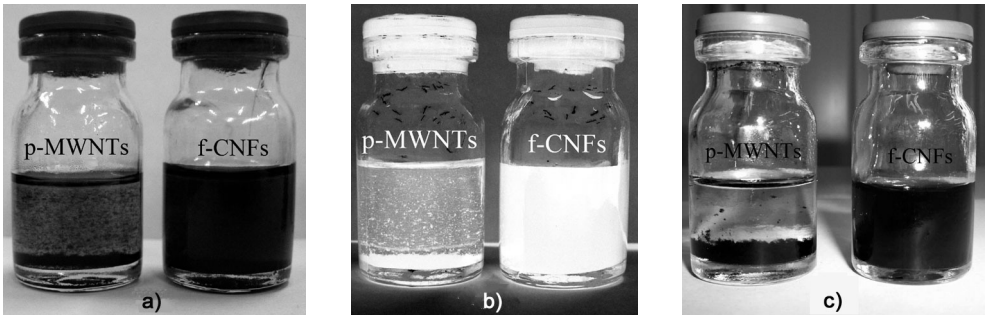

Fig. 4. p-MWNTs and f-CNFs suspensions in toluene (a), DMF (b), and ethanol (c) for variable times after 3 min of sonication. Time since sonication is 30 min (a), 5h (b), 7 days (c)

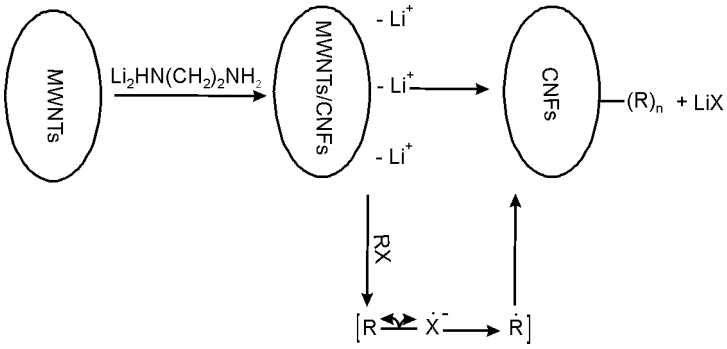

Fig. 5. Proposed mechanism of the conversion process

The mechanism of this interesting conversion from inert MWNTs to highly dispersed f-CNFs seems to be complicated. A preliminary study of the conversion process was undertaken. A comparative experiment was conducted in the absence of an electrophile. When hexadecyl iodide was replaced with a proton source, the tube structures were almost fully preserved (Figs. 1c, 2c). As mentioned above, nearly all the MWNTs are transformed into CNFs when hexadecyl iodide was used. Therefore, the electrophilic reagent plays an important role in the structural conversion. If reagents

with different electrophilic strengths were used, the degree of structural conversion to the final product would differ accordingly, thus resulting in materials with different chiralities and potential uses in electronic applications. Billups et al. [13] proposed that a single electron transferring (SET) mechanism occurs for their reductive alkylation of SWNTs (Birch reaction), including the formation of SWNTs salts and alkylation step in tandum. Mindful of Billups's investigations, we propose that our Benkeser reaction may experience the same process, as shown in Fig. 5. Because the fibre structure cannot be formed without the electrophile in the Benkeser reaction (findings from the comparative experiment), it is concluded that the structure conversion takes place at the alkylation step, rather than the reduction step (salts formation step). The lithiation of the MWNTs causes them to disperse well in ethylenediamne and leaves enough reaction sites for the addition of radicals. Then, the addition of alkyl radicals to the MWNTs may occur not only at the inner graphite layers but also at the outer ones of the MWNTs, which results in the structural deterioration of the MWNTs, and thus yields the functionalized CNFs.

4. Conclusions

A novel conversion of inert MWNTs to highly dispersed CNFs, functionalized with alkyl groups, was developed under the Benkeser reaction, which was confirmed and characterized by TEM, SEM, Raman, IR and TG analyses. The high dispersibility of the CNFs in common solvents was observed in the dispersion experiment. Consequently, this makes then potentially good candidate materials for use as fillers in polymer composites. Preliminary investigations indicate that the conversion takes place at the alkylation step. Investigations on the detailed dynamics of the conversion mechanism, in order to explore the viability of exploiting the considered materials in various fields of electronics, would be the aim of our subsequent research. However, the complexity of the conversion process would make this a highly challenging task.

Acknowledgements

This work was supported by the Chinese National "863" (No. 2006AA03Z570) fund and the Excellent Young Scholars Research Fund of Beijing Institute of Technology (No. c2007YS0404).

References

[1] IIJIMA S., Nature., 354 (1991), 56.
[2] IIJIMA S., ICHIHASHI T., Nature, 363 (1993), 603.
[3] DRESSELHAUS M.S., DRESSELHAUS G., AVOURIS P.H., *Carbon Nanotubes: Synthesis, Structure Properties and Applications*, Springer, Berlin, 2001.
[4] MCINTOSH D., KHABASHESKU V.N., BARRERA E.V., J. Phys. Chem. C., 111 (2007), 1592.
[5] ITKIS M.E., YU A., HADDON R.C., Nano. Lett., 8 (2008), 2224.
[6] KONG J., FRANKLIN N.R., ZHOU C., CHAPLINE M.G., PENG S., CHO K., DAI H., Science, 287 (2000), 622.

[7] NIKITIN A., LI X., ZHANG Z., OGASAWARA H., DAI H., NILSSON A., Nano. Lett., 8 (2008), 162.
[8] BILIĆ A., GALE J.D., J. Phys. Chem. C., 11 (2008), 12568.
[9] YAN D., YANG G., Mater. Lett., 63 (2009), 298.
[10] HU H., ZHAO B., HAMON M.A., KAMARAS K., ITKIS M.E., HADDON R.C., J. Am. Chem. Soc., 125 (2003), 14893.
[11] CHEN L., XIE H., LI Y., WEI Y.U., Mater. Lett., 63 (2009), 45.
[12] STEPHENSON J.J., SADANA A.K., HIGGINBOTHAM A.L., TOUR J.M., Chem. Mater., 18 (2006), 4658.
[13] CHATTOPADHYAY J., CHAKRABORTY S., MUKHERJEE A., WANG R., ENGEL P.S., BILLUPS W.E., J. Phys. Chem. C., 111 (2007), 17928.
[14] TASIS D., TAGMATARCHIS N., BIANCO A., PRATO M., Chem. Rev., 106 (2006), 1105.
[15] KANNAN B., MARKO B., Small., 1 (2005), 180.
[16] BANERJEE S., BENNY T.H., WONG S. S., Adv. Mater., 17 (2005), 17.
[17] TANG X., JIAO Q., CAO Y., ZHANG P., LIU H., WU H., ZHOU M., LI X., ZHAO Y., Chem. Lett., 38 (2009), 220.
[18] COLEMAN J.N., KHAN U., GUN'KO Y.K., Adv. Mater., 18 (2006), 689.
[19] FERRARI A., ROBERTSON J., Phys. Rev. B., 61 (2000), 14095.
[20] BROWN S., JORIO A., DRESSELHAUS M., DRESSELHAUS G., Phys. Rev. B., 64 (2001), 073403.
[21] WANG Y., ALSMEYER D., MCCREERY.R., Chem. Mater., 2 (1990), 557.
[22] RHODES S.M., HIGGINS B., XU Y., BRITTAIN W.J., Polymer., 48 (2007), 1500.
[23] AL-SALEH M.H., SUNDARARAJ U., Carbon., 47 (2009), 2.

Received 27 November 2009

Materials Science-Poland, *Vol. 28*, *No. 3*, *2010*

Thermally stimulated depolarization current Investigations of copolyesteramide (Vectra B 950) polymer liquid crystal

J. K. QUAMARA*, S. K. MAHNA, S. GARG

Department of Physics, National Institute of Technology,
Kurukshetra 136119, India

Thermally stimulated depolarization current (TSDC) characteristics of copolyesteramide (Vectra B950), a polymer liquid crystal having a monomeric composition of 60/20/20 mol % of 6-hydroxy-2 -naphthoic acid (HNA), terethalic acid (TA) and 4-aminophenol (AP) were investigated in the temperature range 20–250 °C in function of polarizing temperature (80–190 °C), polarizing field (2.77–13.88 kV/cm), polarization time (0.5–2 h) and storage time (1 – 100 h). The TSDC spectra in general comprise four maxima, namely β′, β, α, and δ with their respective locations around 30°C, 110 °C, 160 °C and 220 °C. The β peak was attributed to the dipolar nature of the carbonyl group (> C = O) present in HNA and TA non liquid crystalline phase of Vectra B, whereas the β′ peak is due to the dipolar nature of the ester group. The α peak was assigned to a space charge trapping mechanism. A major contribution towards α relaxation comes from interfacial polarization arising from liquid crystalline phase inVectra B. A high temperature of the δ relaxation is associated with the onset of melting due to the movement of large segmental groups of liquid crystalline phase.

Keywords: *Vectra B; polymer liquid crystal; thermally stimulated depolarization current*

1. Introduction

Polymer liquid crystals, i.e. polymers exhibiting liquid crystalline behaviour, were first reported in the mid 1970s [1–3]. These polymers consist of polar groups in anisotropic distribution and non polar groups in the side chains that determine characteristic properties of the liquid crystal. Polymer liquid crystals are demonstrably superior than most widely used engineering thermoplastics with regard to chemical resistance, low inflammability, low melt viscosity, high mechanical and thermal properties, applicability at elevated temperatures, and low isobaric expansivity [3–11]. However, polymer liquid crystals exhibit more complex behaviour than flexible ones. Despite

*Corresponding author, e-mail: jkquamara@yahoo.com

their potential for many applications, the molecular dynamics of various dielectric relaxation processes in polymer liquid crystals are still not well understood, however it is essential before they can be exploited in practical applications. Various dielectric relaxation processes in polymers can be accurately described by applying the thermally stimulated discharge current (TSDC) technique [12]. The TSDC technique essentially consists of two steps: in the first step, a thermoelectret state is formed in the polymers, and then in the second step, the depolarization current spectra at a constant heating rate are obtained. The main advantage of this technique is its high sensitivity, which makes it possible to detect very low dipolar or carrier concentrations. In addition, its very low equivalent frequency allows multicomponent peaks to be resolved accurately. Various current maxima appearing in the TSDC spectra provide deep insight into the molecular origin of dipolar, space charge and other relaxations.

The paper presents our interpretations, based on TSDC analysis, regarding various dielectric relaxation processes occurring in aromatic copolyesteramide polymer liquid crystal, commercially known as Vectra B. Boersma et al. [13] also obtained TSDC data on Vectra B, but only for one polarization parameter T_P (polarization temperature) ranging from 200–280 °C. In the present study, the TSDC spectra of thermoelectret formed under various polarization conditions such as field strength, temperature, time and storage time. In addition, the Cole–Cole distribution was also obtained for the dipolar relaxation process.

2. Theoretical considerations

The decay of polarization after removal of the external field when a polarized polymer is heated uniformly is given as [12]:

$$P(t) = P_e\left[\exp(-\int_0^t \frac{dt}{\tau})\right] \tag{1}$$

where τ is the dipolar relaxation time and P_e is the steady state polarization given by the Langevin formula [12]

$$P_e = \frac{N\mu^2 E_p}{3kT_p} \tag{2}$$

where N is the dipole concentration, μ – the dipole moment, E_p – applied electric field, k – the Boltzmann constant and T_p – the polarizing temperature.

Furthermore, the temperature dependence of τ for a single relaxation mechanism is given by the Arrhenius equation

$$\tau(T) = \tau_0 \exp\left(\frac{U}{kT}\right) \tag{3}$$

where the pre-exponential factor τ_0 is the relaxation time at infinite temperature, and U is the activation energy. Based on Eqs. (1) and (3), the depolarization current density is given as the rate of change of polarization

$$i(t) = -\frac{dP(t)}{dt} = \frac{P(t)}{\tau} \tag{4}$$

Furthermore, in TSDC experiments since time and temperature both vary simultaneously, a new variable T can be introduced by assuming a simple temperature program, so that

$$T = T_0 + ht \tag{5}$$

where T_0 is the initial temperature and $h = \frac{dT}{dt}$ is the heating rate.

From Equations (1)–(5), the TSD current density $i(t)$ at a particular time t can be given as:

$$i(t) = \frac{N\mu^2 E_p}{3kT_p\tau_0} \exp\left[\frac{-U}{kT} - \frac{1}{h\tau_0}\int_{T_0}^{T} \exp\left(\frac{-U}{kT}\right) dT\right] \tag{6}$$

The relaxation time τ at any temperature T can be estimated by the ratio of two quantities: (i) the area under the TSDC curve between the reference temperature T and $T = \infty$, and (ii) the value of the TSDC at the reference temperature T.

From Equation (3) we have

$$\ln\tau = \ln\tau_0 + \frac{U}{kT} \tag{7}$$

The activation energy U can be calculated from the slope of the straight line of the $\ln\tau(T)$ versus $1/T$ plot, using the Bucci plot method [12].

3. Materials and methods

The material used in the present study was liquid crystal of aromatic copolyesteramide polymer procured by the Good Fellow (UK). The polymer is commercially known as Vectra B950, with a composition of 60 mol % of 6-hydroxy-2-naphthoic acid (HNA), 20 mol % of terethalic acid (TA) and 20 mol % 4-aminophenol (AP) [14]. Henceforth we will refer to this polymer liquid crystal asVectra B. TheVectra B samples in the form of pallets of thickness 1.8mm and diameter 19mm were metalised on both sides by vacuum evaporation of aluminum, to form electrical contacts. The sample holder designed for this purpose was suspended in a specially prepared tem-

perature-controlled furnace, shielded against stray pickups. The furnace could be heated at an arbitrary, but constant, rate from room temperature to 250 °C.

The samples were polarized by subjecting them to the desired field E_P at constant temperature T_P for the polarization time t_p, following the usual method [13]. The TSDC data were obtained at a constant heating rate h in the temperature range 20–250 °C using the Keithley electrometer (610C). For studying the aging (storage time) effect, the polarized samples were stored for a specified period t_s. For all the measurements, the heating rate, polarization time and storage time were 2 °C /min, 60 min and 10 min respectively, unless specified otherwise. The activation energies U for various relaxation modes were calculated.

4. Results

Figures 1–4 illustrate the TSDC spectra of Vectra B samples in the temperature range 20–250 °C for various polarization and storage conditions. The number of peaks in the spectra, their location, height and sharpness are found to be governed by the polarization and depolarization parameter as well as the storage time. The TSDC spectra show current peaks at around 30 °C, 110–130 °C, 160–170 °C and 220 °C, and are denoted as β′, β, α and δ peaks, respectively. The values of the activation energy (U) and the pre-exponential factors τ_0 for the β′, β and α peaks with E_p are given in Tables 1, 2 and 3, respectively. The activation energy of the δ peak, which appears only for a high polarization time (t_p = 120 min), comes out to be 0.90 eV.

4.1. Polarization field dependence

Figure 1 illustrates the effect of the polarization field E_P ranging from 2.77 kV/cm to 13.88 kV/cm on TSDC spectra of Vectra B samples polarized at T_P = 100 °C and 190 °C, respectively. We observe a well defined α peak around 160–170 °C (Fig. 1b). The peak temperature T_m is almost independent of E_P but the peak current I_m increases upon increasing polarization field and it exhibits a linear dependence on $E_P^{1/2}$ (inset of Fig. 1b). In addition, a β′ peak also appears around 30 °C. The β peak located around 110–130 °C, is pronounced only for T_P = 100 °C (Fig. 1a). The peak height I_m for this peak shows a linear dependence on E_P (inset of Fig. 1a).

4.2. Polarization temperature dependence

The effect of the polarization temperature on TSDC spectra of Vectra B samples (E_p = 5.55kV/cm) is shown in Fig. 2. The presence of the β peak is clearly evident in Fig. 1a. A shift in the β peak is observed for samples poled at T_P > 110 °C. This temperature is also the glass transition temperature T_g of Vectra B. The α peak appears only in the spectra of samples poled at high T_P. A shift in the α peak location is also

observed towards higher temperatures as T_P increases. A significant enhancement in the height of the α peak is observed in high T_P poled samples. Interestingly, the β′ peak (around 30 °C) is well defined in all the cases, and is observed to increase as T_P increases.

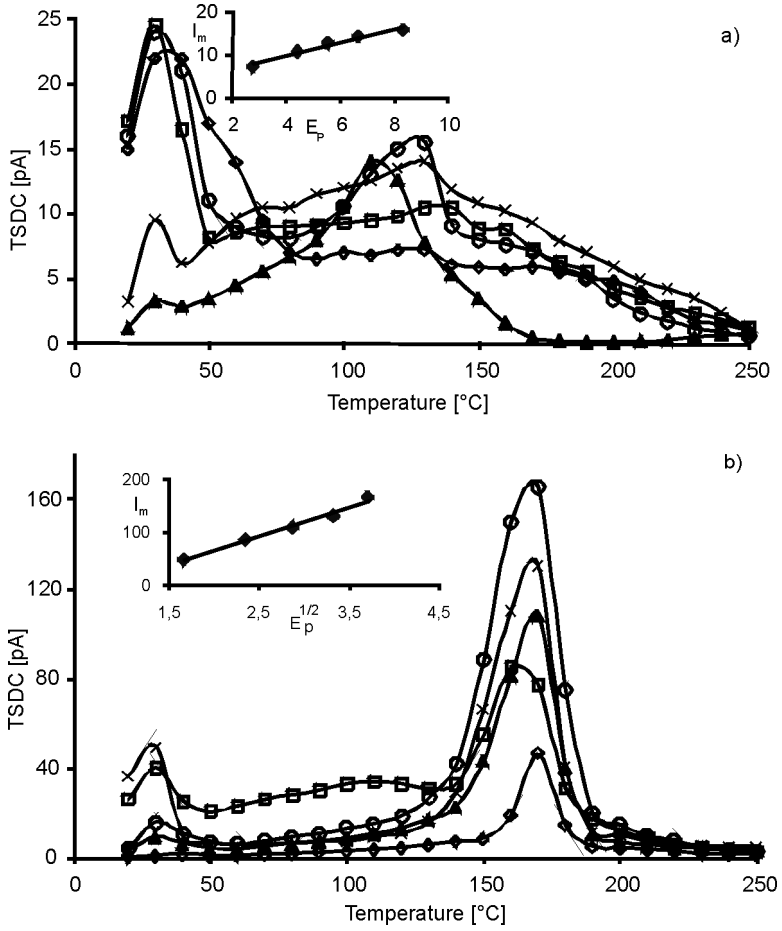

Fig. 1. TSDC spectra of Vectra B samples polarized with various E_P: ◊ –2.77 kV/cm, □ – 4.44 kV/cm, ▲ – 5.55kV/cm, X – 6.66kv/cm, ○– 8.33kV/cm at 100 °C (a), 190 °C (b)

4.3. Effect of storage time (t_s)

The TSDC spectra of Vectra B samples, polarized and discharged under identical conditions but stored for different times (electret aging), are shown in Fig. 3. An increase in t_s suppresses the entire TSDC spectra. The heights of the β′, β, and α peaks reduce gradually. However, the β′ and β peaks vanish completely at high storage times. Further, the α peak shifts towards higher temperaturs and becomes broader as t_s increases.

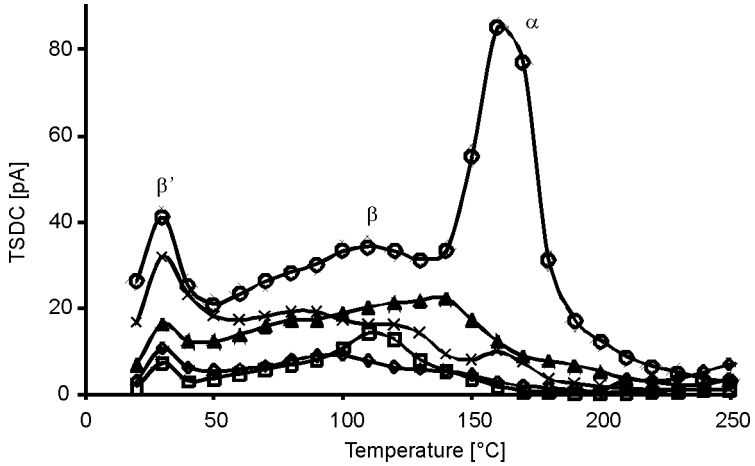

Fig. 2. TSDC spectra ofVectra B samples polarized with various T_P:
◊ – 80 °C, □ – 100 °C, ▲ – 130 °C, X – 160 °C, ○ – 190 °C; E_P – 5.55kV/cm

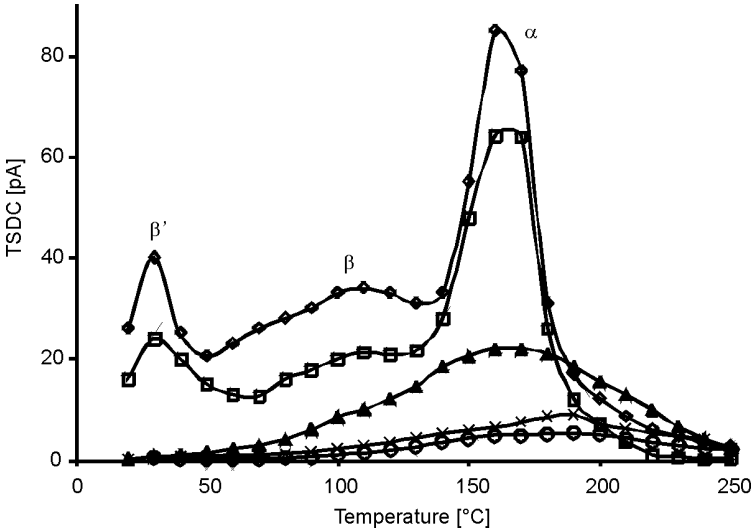

Fig. 3. The TSDC spectra ofVectra B samples stored for various aging times:
◊ – 1 h, □ – 5 h, ▲ – 20 h, X – 50 h, ○ – 100 h; E_P – 5.55 kV/cm, T_P – 190 °C

4.4. Effect of polarization time

The effect of polarization time on the TSDC spectra of Vectra B samples is shown in Fig. 4. Upon the increasing polarization time the β′ peak gradually decreases. The β peak at a short polarization time remains unaffected, but at a long polarization time it disappears completely. A significant increase in the height of the α peak is observed at high $t_{p,}$ and the peak also becomes broader.

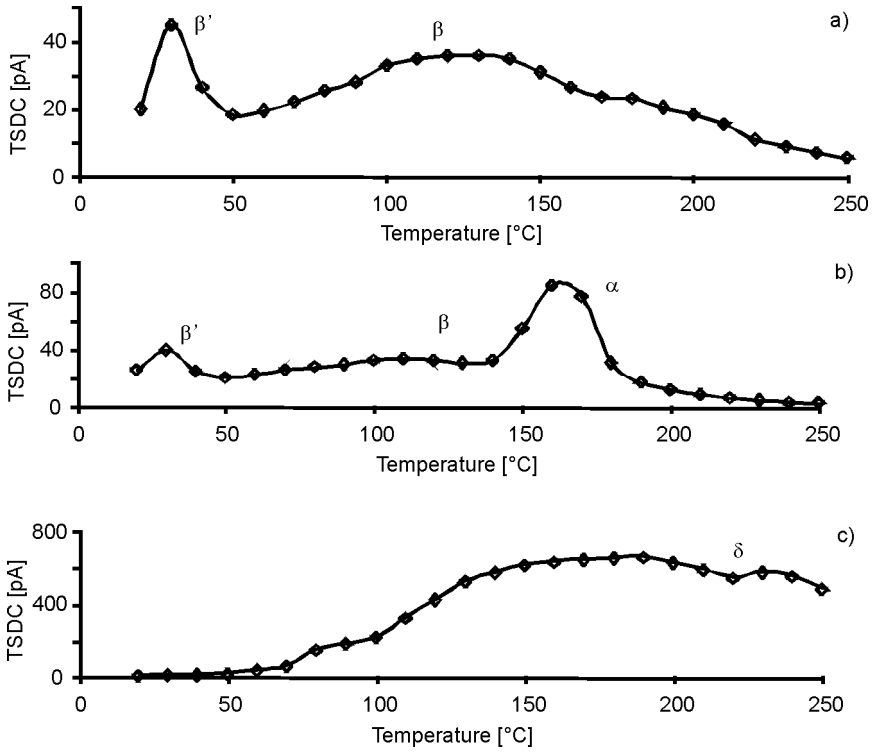

Fig. 4. The TSDC spectra ofVectra B samples polarized for various polarization times: a) 30 min, b) 60 min, c) 120 min; E_P – 5.55 kV/cm, T_P – 190 °C

5. Discussion

The dielectric relaxation processes in liquid crystal polymers are quite complex in nature and presumably result from several different competitive mechanisms involving various physical states associated with crystalline and amorphous phase. The chemical structure of Vectra B is shown below [15]:

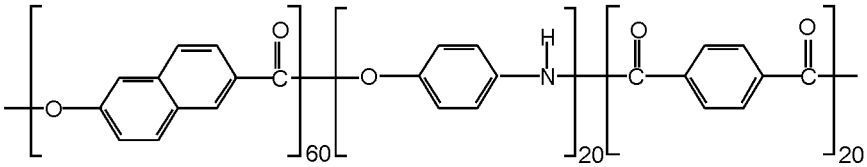

The monomeric composition of Vectra B is 60/20/20 mol % of 6-hydroxy-2-naphthoic acid (HNA), terethalic acid (TA) and 4-aminophenol (AP). A benzene ring associated with the aminophenol molecule provides the liquid crystalline phase to the Vectra B, whereas the amide and the ester group act as bridging groups. The dipolar nature of Vectra B arises from the presence of carbonyl [>C = O] groups in HNA

as well as in TA. A dielectric relaxation process associated with the dipolar nature of >C = O groups in various polymeric materials (termed as β relaxation) has been discussed by many groups [12, 16, 17].

Table 1. Activation energies and pre-exponential factors for β' relaxation of Vectra B

E_P [kV/cm]	T_P [°C]	U [eV]	τ_0 [s]
2.77	190	–	–-
4.44	190	0.11	1.1×10^{-6}
5.55	190	0.16	7.6×10^{-9}
6.66	190	0.13	1.6×10^{-7}
8.33	190	0.13	2.3×10^{-3}
5.55	80	0.13	4.1×10^{-9}
5.55	100	0.15	2.3×10^{-3}
5.55	130	0.14	5.4×10^{-3}
5.55	160	0.15	5.8×10^{-2}

Table 2. Activation energies and pre-exponential factors for β relaxation of Vectra B

E_P [kV/cm]	T_P [°C]	U [eV]	τ_0 [s]
2.77	100	0.32	1.1×10^{-1}
4.44	100	0.36	2.4×10^{-2}
5.55	100	0.42	1.6×10^{-7}
6.66	100	0.44	2.3×10^{-3}
8.33	100	0.43	2.7×10^{-3}
5.55	80	0.41	2.3×10^{-3}
5.55	130	0.23	5.4×10^{-1}
5.55	160	0.29	7.7×10^{-2}
5.55	190	0.22	1.5×10^{-13}

Table 3. Activation energies and pre-exponential factors for α relaxation of Vectra B

E_P [kV/cm]	T_P [°C]	U [eV]	τ_0 [s]
2.77	190	0.68	1.2×10^{-4}
5.55	190	0.72	1.5×10^{-13}
8.33	190	0.74	4.7×10^{-14}
11.11	190	0.79	4.4×10^{-10}
13.88	190	0.82	2.4×10^{-10}

In the present TSDC analysis, the current maximum (β peak) appearing around 110–130 °C (Figs. 1a, 2) has been attributed to the dipolar nature of >C = O groups present in Vectra B structure. The dipolar nature of this relaxation can be judged from certain characteristics observed for this peak, such as: (i) its pheight varies linearly with the polarizing field (inset of Fig. 1a) which is also an indication of uniform induced bulk polarization [18]; (ii) the activation energy associated with this peak (Table 2) is of the same order of magnitude as that predicted theoretically for the side group orientation in polymers [19]; (iii) a shift in the peak temperature occurs as T_P increases. The broad nature of this peak shows a large distribution in the relaxations times. This is due to the fact that various >C = O groups present in Vectra B monomer units are situated at different locations; one >C = O group is present in ester linkage of HNA and AP and other >C = O is present in amide linkage of TA and AP.

For a certain relaxation process in a polymer, the peak temperature is given as [12, 20, 21]:

$$T_m = hU \frac{\tau_{T_m}}{k} \tag{8}$$

where τ_{T_m} is the relaxation time at temperature T and k is the Boltzmann constant. The above dependence shows that for a single relaxation time (single energy of activation) and for a given rate of heating h, T_m should be independent of T_P and t_p. At low values of T_P (or t_p) only fast sub-polarizations could be operative but as T_P (or t_p) is increased, more and more sub-polarizations with longer relaxation times would be activated [22, 23], thereby shifting the peaks towards higher temperatures and also enhancing their hights. In Vectra B, the distribution of the polarization may appear due to non-identical environment around different >C = O groups. Vectra B, being a longitudinal polymer liquid crystal, has 4-aminophenol particles as liquid crystalline phase sandwiched between HNA and TA being non-liquid crystalline flexible spacers [24]. Lenz [25] has shown that flexible spacers are particularly important for thermotropic longitudinal polymer liquid crystals. The type and length of the spacers can determine whether a nematic, cholesteric or smectic phase is formed. At elevated temperatures, under the influence of a field, reduction in the length of the spacer results in an increase in the rigidity of molecules there, by shifting T_m to higher temperatures.

The TSDC maximum appearing around 160–170 °C (α peak, Fig. 1b) has been assigned to a space charge trapping mechanism. In polymer liquid crystals, the charge trapping is possible owing to the presence of crystalline phase, which is responsible for space charge formation via interfacial polarization (Maxwell, Wagner–Sillars effects) [26]. In addition, unsaturated amide and carbonyl groups (due to conjugation) can act as traps for charge carriers contributing to their transport and trapping. The charge trapping may also take place at aromatic carbon, but the probability is much lower compared with the probability of charge trapping at carbonyl carbon. It is due to the delocalization of π electron in the aromatic ring. The space charge origin of this

peak is also confirmed by the following facts: (i) its peak current I_m depends linearly on $E_P^{1/2}$ (inset of Fig. 1b), which also shows the occurrence of an overall non-uniform bulk polarization; (ii) during the electret storage, the peak vanishes almost completely during long storage time (Fig. 3), and; (iii) the corresponding activation energy values for this peak (Table 3) are in the same range as that reported for α relaxation. Furthermore, it is an established fact that viscoelastic and dielectric properties of polymers are directly related to each other. The dynamic mechanical analysis (DMA) of Vectra B samples show a maximum in the loss modulus versus temperature curve, at around 160–170 °C [27]. This is in conformity with the occurrence of α relaxation around this temperature.

A significant enhancement in the α relaxation observed for high t_P (Fig. 4c) is also in conformity with the enhancement in the crystallinity resulting from increased annealing time [28, 29]. The broad nature of the α relaxation for high t_P further shows the merger of multiple transition processes (with large distribution in relaxation time) in the vicinity of α relaxation

An enhancement in the crystallinity with increasing temperature in polymer and also in liquid crystalline polymers particularly above glass transition temperature has been reported by several authors [29, 32]. Increase in crystallinity in polymers result in an increase in α relaxation and lowering of the dipolar relaxation. This is in agreement with the TSDC analysis for this study, namely increases in the α peak intensity correspond to increases in *Tp* (Fig. 2). A higher poling temperature or poling time means more intense annealing and this explains a weaker β relaxation process in high T_P poled samples.

The TSDC maximum appearing at high temperature is generally considered to be due to the charge injection into the polymer from the electrodes directly and/or through interfacial layers, i.e. the Townsend breakdown [12, 20]. However, in the present case, the current maximum appearing around 220 °C (δ peak, Fig. 4c) in high t_P polarized samples cannot be attributed to the charge injection phenomenon, as the polarization fields used are not sufficiently high to cause the Townsend breakdown. Furthermore, the possibility of charge injection can also be ruled out because of the vacuum deposited electrodes. Brostow et al. [33] have shown a high temperature transition in PET/x.PHB polymer liquid crystal due to melting, i.e. movement of large segmental groups in liquid crystalline phase. This transition has also been observed by Quamara et al. [32] in the TSDC analysis of PET/x.PHB polymer liquid crystal. Although the melting temperature of Vectra B has been reported to be around 280 °C [14], the onset of such a melting process should take place at much lower temperature than the actual melting point itself. Hence the δ relaxations can be attributed to melting, i.e. to the movement of large segmental groups in liquid crystalline phase. The onset of this melting process, at around 220 °C, in Vectra B is also evident from an abrupt decrease in its tensile moduli for the same temperature range [27]. The occurrence of δ relaxations in Vectra B is also confirmed from our thermally stimulated

polarized current investigations [34] where we observed a saturation in the polarization current at around 220 °C.

The β′ peak around 30–35 °C cannot be associated with any known transition in Vectra B. Though Dreher et al. [11] have shown a dielectric loss peak around 77 °C but this temperature is almost 45 °C above the β′ peak temperature, thus we are not sure whether the β′ peak can have any relationship with this tanδ peak. Interestingly, in the case of Vectra A and Vectra E, transitions are observed to occur around 35 °C, based on analysis of the temperature versus loss modulus characteristics [27]. Since the β′ peak also lies in the same temperature range, it appears that some common molecular dynamics in these polymer should govern this relaxation process. From the structural analysis of Vectra series polymer liquid crystals (A, B and E), we observe that the ester linkage is common amongst them. This indicates that the dipolar nature of ester linkage may be the cause of β′ relaxation. The activation energy associated with this peak (Table 1) is also in agreement with its dipolar character.

6. Cole–Cole distributions

A distribution function is a measure of the distribution of relaxation times associated with different relaxation processes in a polymer. As we have discussed above, there appears to be a broad distribution in the relaxation times for the β relaxation process in Vectra B. A number of independent causes may be responsible for this distribution. Though there are several forms of distribution functions suggested by many authors [35–38], the most suitable one for describing the distribution of relaxation times τ_m for TSDC is given by the Cole–Cole distribution function [35]. We have obtained the Cole–Cole distribution function of the β peak for Vectra B samples for different polarizing parameters, using following equation [35]

$$f'(u) = \frac{\sin(\beta\pi)}{2\pi\left[\cosh(\beta u) + \cos(\beta\pi)\right]} \tag{9}$$

where $\infty < \tau < \infty$, $0 < \beta \leq 1$ and $u = \ln(\tau/\tau_m)$. The values of τ and τ_m are evaluated using Eq. (3).

The Cole–Cole distribution curves in the form of $f'(u)$ versus u for Vectra B samples polarized at various E_P (T_P = 100 °C) are shown in Fig. 5. These curves show the distribution of τ becomes wider as E_P increases. This is corroborated by the fact that with an increase in the polarizing field, there should be an enhancement in the spectrum of dipolar relaxation times. The shifting of β peaks towards higher temperatures as T_P increases suggests that the distribution function is temperature dependent. In Vectra B, the spectrum of relaxation times is attributable to the presence of different >C = O groups in its monomer units at various locations. In addition, the anisotropy of the internal field in which the dipoles reorient may also contribute to the relaxation spectrum, as in case of other polymers [38].

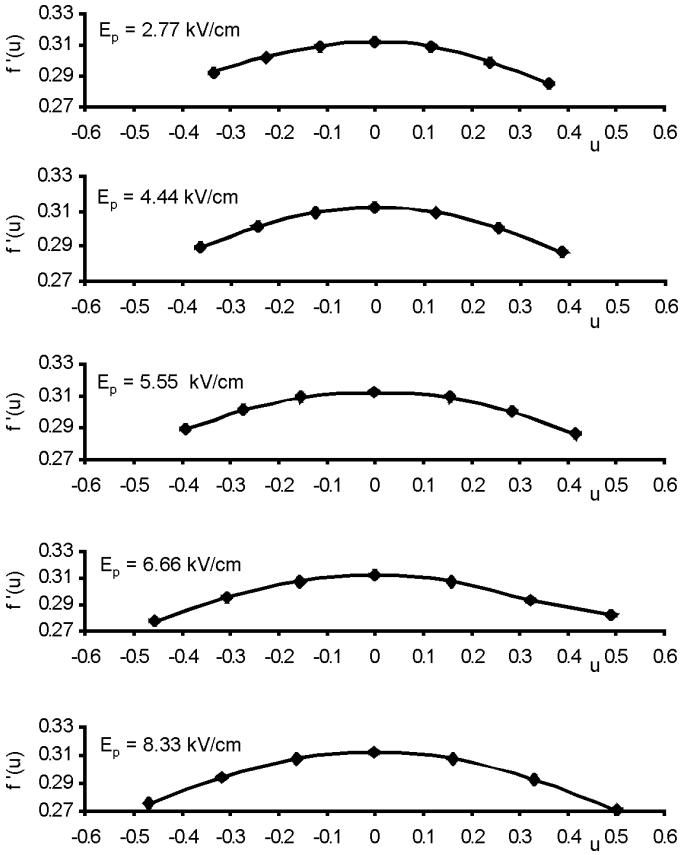

Fig. 5. Cole–Cole spectra of Vectra B samples

7. Conclusions

The TSDC spectra of Vectra B samples polarized under various polarization conditions confirm the occurrence of multiple relaxation processes, denoted β′, β, α, and δ in ascending order of temperature of occurrence in the polymer liquid crystals. The presence of carbonyl groups in the structure of Vectra B is responsible for the occurrence of β relaxation, whereas the α relaxation is due to space charge trapping mechanism via interfacial polarization arising from liquid crystalline phase. The activation energy, as computed using the from Bucci plot method, confirms different types of the relaxations. The β′ relaxation has been associated to ester linkage and δ relaxation is due to the movement of large segmental groups in a liquid crystalline phase.

Acknowledgements

The authors are grateful to DRDO New Delhi for providing funds for the present work.

References

[1] ROVIELLO A., SIRIGU A., J. Polym. Sci. Polym. Lett., 13 (1975), 455.
[2] JACKSON W.J. Jr., KHUFFUSS H.F., Polymer Sci. Polymer Chem., 14 (1976), 2043.
[3] FLORY P.J., ABE A., Macromolecules, 11 (1978), 1122.
[4] BROSTOW W., Kunststoffe, 78 (1988), 411.
[5] GEDDE U.W., LIU F., HULT A., SAHLEN F., BOYD R.H., Polymer, 33 (1994), 2056.
[6] QUAMARA J.K., KAUSHIK B.K., Indian J. Pure Appl. Phys., 34 (1996), 553.
[7] WEISS R.A., SHAO L., LUNDBERG R.D., Macromolecules, 25 (1992), 6370.
[8] GOULD S.A.C., SHULMAN J.B., SCHIRALDI D.A., OCCELLI M.L., J. Appl. Polym. Sci., 74 (1999), 2243.
[9] MANDAL P.K., BANDYOPADHYAY D., CHAKRABARTY D., J. Appl. Polym. Sci., 88 (2003), 767.
[10] VALLEJO F.J., EGUIAZABAL J.I., NAZABAL J., Polym. Engg. Sci., 39 (1999), 1726.
[11] DREHER S., SEIFERT S., ZACHMANN H.G., MOSZNER N., MERCOLI P., ZANGHELLINI G., J. Appl. Polym. Sci., 67 (1998), 531.
[12] VAN TURNHOUT J., [In:] *Electrets*, G.M. Sessler (Ed.), Springer, Berlin, (1980), 81.
[13] BOERSMA A., VAN TURNHOUT J., WUBBENHORST M., Macromolecules, 31 (1998), 7453.
[14] US Patent 5834560, *Liquid Crystal Polymers*, November 10, (1998).
[15] CHUNG SHUNG T., [In:] *Thermotropic Liquid Crystal Polymer*, CRC Press, (2001), 41.
[16] QUAMARA J.K., PILLAI P.K.C., SHARMA B.L., Acta Polym., 33 (1982), 205.
[17] SESSLER G.M., [In:] *Electrets*, Springer, Berlin, 33 (1980), 13.
[18] GROSS B., J. Chem. Phys., 17 (1949), 866.
[19] REDDISH W., Trans. Faraday Soc., 46 (1950), 459.
[20] BHARDWAJ R.P., QUAMARA J.K., NAGPAL K.K., SHARMA B.L., Phys Status sol. (a)., 77 (1983), 347.
[21] GARG M., KUMAR S., QUAMARA J.K., Indian J. Pure Appl. Phys., 39 (2001), 259.
[22] HINO T., SUZUKI K., YAMASHITA K., Japan J. Appl. Phys., 12 (1973), 651.
[23] TURNHOUT VAN J., [In:] *Thermally Stimulated Discharge of Polymer Electrets*, Elsevier, Amsterdam (1975).
[24] SOLUNOV H., VASSILEV T., J. Polym. Sci. Polym. Phys., 12 (1974), 1273.
[25] LENZ R.W., Faraday Disc., 79 (1985), 21.
[26] BROSTOW W., KAUSHIK B.K., MAL S.B., TALWAR I.M., Polymer, 33 (1992), 22.
[27] SHEPARD D.D., TWOMBLY B., Thermiochim. Acta, 272 (1996), 125.
[28] MATSUOKA S., [In:] *Relaxation Phenomenon in Polymer*, Hansar Publ., New York (1992), 211.
[29] CHUNG SHUNG T., [In:] *Thermotropic Liquid Crystal Polymer*, CRC Press, (2001), 88.
[30] HUO P., CEBE P., Polymer Sci., Part B: Polymer Phys., 30 (1992), 239.
[31] JOSHI S., RADHAKRISHAN S., Thin Solid Films, 142 (1986), 213.
[32] QUAMARA J. K., SRIDHARBABU Y., Indian J. Pure Appl. Phys., 41 (2003), 790.
[33] BROSTOW W., SAMATOWICZ D., Polym. Eng. Sci., 1 (1992), 87.
[34] QUAMARA J.K., MANHA S.K., GARG S., Int. J. Polym. Anal. Charact., 15 (2010), 298.
[35] COLE K.S., COLE R.H., J. Chem. Phys., 19 (1951), 1484.
[36] WAGNER K.W., Ann. Phys., 40 (1913), 817.
[37] FROHLICH H., [In:] *Theory of Dielectrics*, Oxford University Press, London, 1958.
[38] GARG M., QUAMARA J.K., Nucl. Instr. Meth. B, 246 (2006), 355.

Received 9 January 2010
Revised 6 August 2010

Materials Science-Poland, *Vol. 28*, *No. 3*, *2010*

Deposition of thin hydroxyapatite films by 335 nm Nd:YAG laser ablation

M. JEDYŃSKI[1, 2*], J. HOFFMAN[1], T. MOŚCICKI[1], W. MRÓZ[2], S. BURDYŃSKA[2], R. DIDUSZKO[3], P. KOŁODZIEJCZAK[4], Z. SZYMAŃSKI[1]

1Institute of Fundamental Technological Research, Polish Academy of Sciences, Świętokrzyska 21, 00-049 Warsaw, Poland

[2]Institute of Optoelectronics of Military University of Technology, Kaliskiego 2, 00-908 Warsaw, Poland

[3]Tele & Radio Research Institute, Ratuszowa 11, 03-450 Warsaw, Poland

[4]Warsaw Technical University, Narbutta 85, 02-524 Warsaw, Poland

The characteristics of hydroxyapatite ($Ca_{10}(PO_4)_6(OH)_2$) thin films deposited by the pulsed laser deposition technique have been describrd. The laser used was a Nd:YAG, operating at the wavelength of 355 nm. All films were deposited at room temperature, either in ambient water vapour or in vacuum, and were annealed, after deposition in air, at 600 °C. Next, they were examined with the use of an X-ray diffractometer, Fourier transform infrared spectrometer, atomic force microscope, micro scratch tester and scanning electron microscope. The analyses showed that crystalline films exhibiting very strong adhesion to the substrate have been obtained.

Keywords: *pulsed laser deposition; hydroxyapatite; biomaterials*

1. Introduction

Growth of thin films of chemically complex materials by the pulsed laser deposition has several advantages. The method is versatile – the laser energy source is outside the chamber and can be changed; practically any material can be vaporized; targets can be used, either in vacuum or in a atmosphere consisting of various reactive gases; sequential ablation of suitable targets allows deposition of multilayered films of various materials. Very precise control of the film thickness is possible, by adjusting the laser pulse mode. High quality films with good adhesion to the substrate can be fabricated with a high deposition rate.

Other advantage of the method is that the stoichiometry of the target is preserved in the deposited films, even in the case of materials having a complex structure. This

*Corresponding author, e-mail: mjedynski@wat.edu.pl

probably results from the fact that a high energy flux to the surface of a target causes all material constituents to be vaporized practically at the same time, regardless of their evaporation temperature. Stoichiometry is, in fact, preserved only in the vicinity of a target. At further distances it is lost due to differences in the molecular masses of the expanding elements and the resulting differences in their rates of expansion.

In this work, the films produced by laser ablation of hydroxyapatite ($Ca_{10}(PO_4)_6(OH)_2$) were studied. Synthetic hydroxyapatite (HA) is a biocompatible ceramics. It is chemically similar to the mineral component of mammalian bone. For this reason, the human body (and bodies of other mammals as well) can adapt HA. HA into it. HA is classified as a bioactive material, forming strong chemical bonds with surrounding bones, unlike other materials such as alumina and zirconia, which are identified as foreign materials and become encapsulated by fibrous tissue. HA is deposited onto orthopaedic implants in order to increase the surface area of bone –implant contact.

Important factors determining the quality of the HA coating are the cohesive strength, the degree of crystallinity and the adherence to the metal surface. In addition, phase stability is essential for successful growth of the osteoblast cells on the film. In the case of hydroxyapatite, it has been found that good coatings are obtained when the ambient gas is water vapour or argon mixed with water vapour at the pressure of 10–150 Pa [1, 2]. In all cases, heating of the substrate over 400 °C is necessary in order for the deposited films to have a crystalline structure. Otherwise amorphous films are obtained which exhibit rapid in vivo degradation, and are unsuitable for medical applications that require biological fixation of the implant to bony tissue [1]. In the case of human joint replacements, titanium alloy Ti_6Al_4V is a typical substrate used for film deposition. On the other hand, films deposited on Ti_6Al_4V substrates at elevated temperatures exhibited very poor substrate adhesion, which was attributed to softening of the substrate, formation of a titanium oxide layer between the hydroxyapatite film and the Ti_6Al_4V substrate, and thermal stresses [1]. Also, the shapes of real implants are complicated and they cannot be heated during deposition as easily as flat substrates. Deposition at room temperature increases adhesion [1, 3] but then post-deposition annealing of hydroxyapatite thin films is necessary to obtain a crystalline film structure. Those experiments, conducted at room temperature, were made with a KrF laser operating at the wavelength of 246 nm and fluency 1–5 $J \cdot cm^{-2}$ [1, 3, 4].

In this work, a Nd:YAG laser was used. A hydroxyapatite (HA) target was ablated under various conditions, i.e. during expansion into vacuum or water vapour. The substrate was kept at room temperature. Next, the deposited HA films were annealed and examined.

2. Experimental

An Nd:YAG Quantel YG981 laser was operated at the wavelength of 355 nm with a pulse energy of 100 mJ and 10 ns pulse duration. The repetition rate was 10 Hz. The

hydroxyapatite target was a dense disk, acquired from the Berkeley Advanced Biomaterials, Inc. The laser fluence was ~3.3 J·cm^{-2} (intensity I = 0.33 GW·cm^{-2}). The incident angle of the laser beam was 45° to the surface normal. The deposition was made in a PLD chamber, either in vacuum or in ambient water vapour, at the pressure of 20 Pa. The number of pulse changes ranged from 12 000 to 18 000. The substrates were Ti_6Al_4V alloy discs positioned at the distance of 4 cm from the target and kept at room temperature. All substrates were polished with abrasive grinding paper and cleaned with acetone, isopropanol and distilled water before use. The roughness of the substrate surface, as measured with a Form Talysurf scanning profilometer, indicated that the Mean square deviation of the substrate surface was about 0.05 μm.

The deposition rate was about 0.18 nm per pulse in water vapour and 0.5 in vacuum. The difference is understandable because in the presence of an ambient gas, the ablated particles are scattered in collisions with the gas molecules and only part of them reach the substrate. After deposition, the substrates were annealed for 1 h in ambient air at 600°C. Next, they were examined with the use of an X-ray diffractometer (XRD), Fourier transform infrared spectrometer (FTIR), Atomic force microscope (AFM), micro scratch tester (MST) and a profilometer. All tests were made at least in duplicate, showing good reproducibility of results.

3. Results

3.1. Film structure

The identification of phases present in the deposited films was made with the use of X-ray diffractometry. The CuK_α line of the wavelength of 1.54 Å was used. The spectra are shown in Fig. 1. Figure 1a shows the diffractogram of the HA target, Fig. 1b shows the diffractogram of HA film deposited after 18 000 pulses in an atmosphere of water vapour under the pressure of 20 Pa, and Fig. 1c shows the diffractogram of HA film deposited after 12 000 pulses under vacuum. One should note that the deposition rate is much higher in vacuum and that the 12 000 pulse coatings are about twofold thicker than the 18 000 pulse coatings obtained in water vapour. All the pertinent peaks of the HA target are present in the deposited films, although some of them are overshadowed by titanium or steel peaks arising from the substrate. All peaks are narrow, which indicates that polycrystalline phase prevails in the deposited films. The only peaks not present in the pattern for the HA target are the titanium peaks, which means that the HA films are not contaminated by any of the dehydrated forms of HA, such as α-tricalcium phosphate (α-TCP) or β-TCP [5].

Absorption spectra of the deposited films, as obtained with the use of the Fourier transform infrared spectrometer (FTIR), are shown in Fig. 2. Characteristic bands [6] of HA are present in all the spectra, i.e., the phosphate band PO_4, the carbonate band CO_3, the hydrocarbon band CH and the hydroxyl band OH.

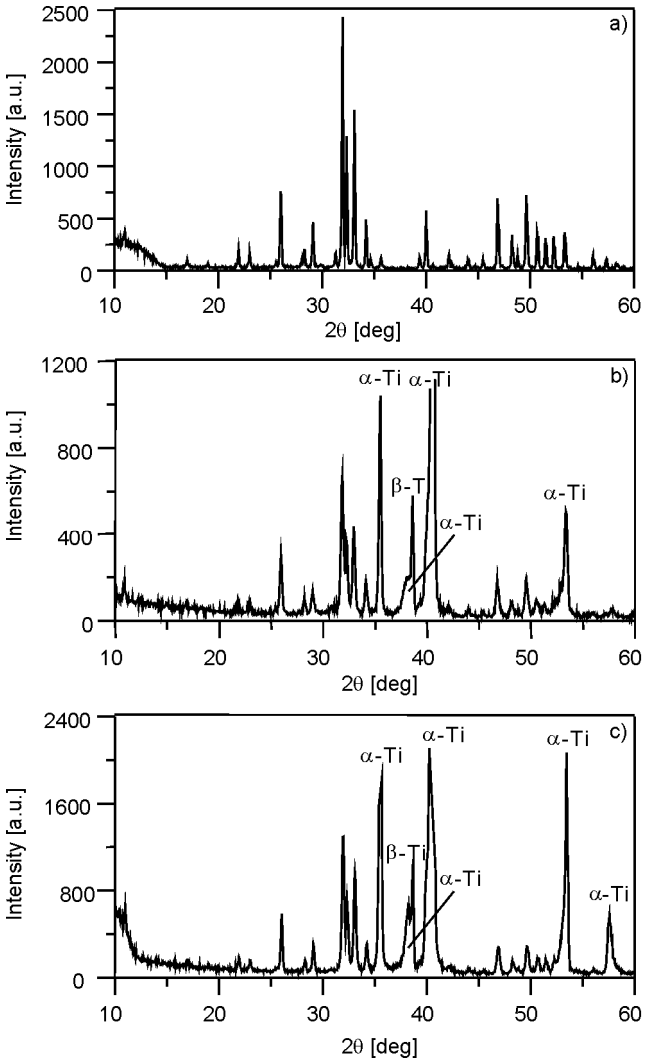

Fig. 1. Diffractograms (CuKα, 1.54 Å) of the HA target and deposited films. All peaks, except for Ti6Al4V, correspond to hydroxyapatite: a) HA target, b) HA film deposited in water vapour, 18 000 pulses, c) HA film deposited in vacuum, 12 000 pulses

Four vibrational modes of phosphate ions, denoted as ν1, ν2, ν3 and ν4, are observed. The ν1 mode has the frequency of 950–1000 cm^{-1}, the ν2 mode 430–460 cm^{-1}, the ν3 mode 1040–1090 cm^{-1}, and the ν4 mode 520–660 cm^{-1}. In both cases, namely for 18 000 pulses in water vapour or 12 000 pulses in vacuum, three well-defined and sharp peaks, occurring at 566, 598 and 630 cm^{-1}, are observed in the ν4 phosphate band. Also, the ν3 phosphate band has well defined peaks at 962, 1000, 1060 and 1087 cm^{-1}. Weak carbonate bands ν3 lie at 1415 and 1465 cm^{-1}. Peaks corresponding to hydro-

carbon bond are situated at 2850 and 2930 cm^{-1} and a broad hydroxyl band in the 3000–3600 cm^{-1} range. Narrow peaks indicate the presence of a polycrystalline phase.

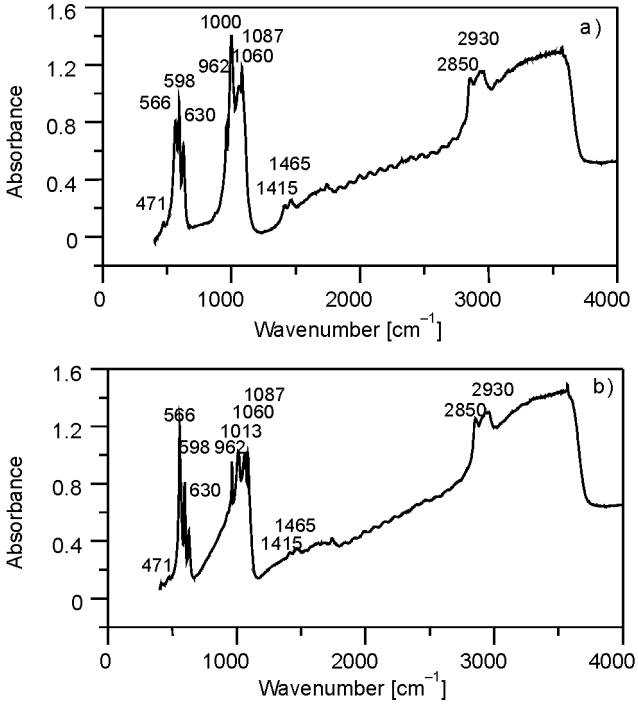

Fig. 2. FTIR spectra of deposited films:
a) 18 000 pulses, water vapour, b) 12 000 pulses, vacuum

3.2. Topography

The topography of the deposited films was studied by the atomic force microscopy, using a Veeco Multi Mode IV SPM. The microscope was used in a tapping mode together with phase mode imaging. In the tapping mode, a stiff cantilever is oscillated close to the sample in an intermittent contact mode. Part of the oscillation extends into the repulsive regime, thus the tip intermittently touches or "taps" the surface. This mode avoids the surface damage associated with contact mode imaging, in the case of soft samples. In phase mode imaging, the phase shift of the oscillating cantilever relative to the driving signal is measured. Contrasts between these phase shifts can be correlated with specific properties of materials such as adhesion forces, surface inhomogeneities, etc. However, in the case of hydroxyapatite such an analysis is still not reliable. Therefore pictures obtained from phase imaging are not presented here.

The topography of the deposited films is shown in Fig. 3. The coating deposited in ambient water vapour after 18 000 laser pulses (Fig. 3a) exhibits a fine-grained struc-

ture in comparison with coatings deposited under a lower pulse count. This coating is characterized by a highly homogeneous distribution of grains.

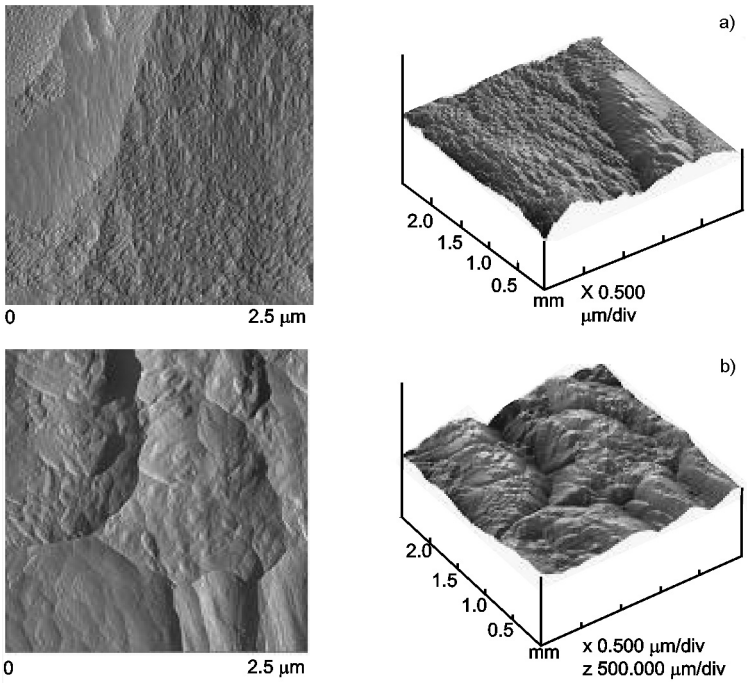

Fig. 3. Topography of deposited layers of hydroxyapatite from AFM: a) 18 000 pulses, water vapour, b) 12 000 pulses, vacuum

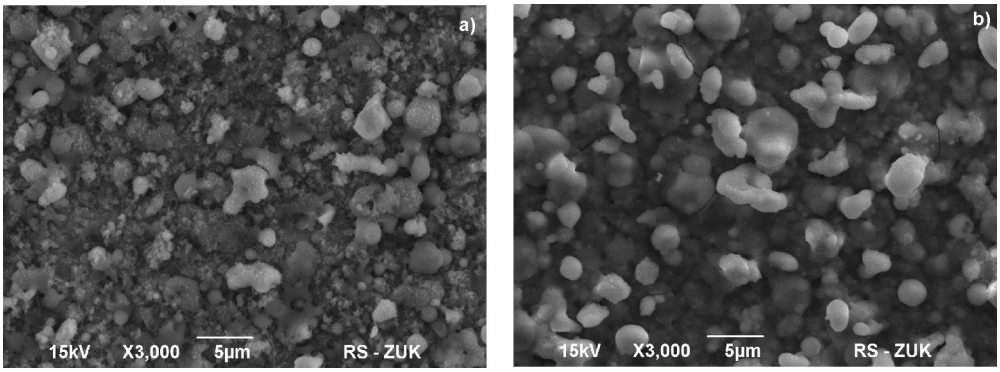

Fig. 4. SEM images of the HA coatings; a) 18 000 pulses, water vapour, b) 12 000 pulses, vacuum

In the case of 12 000 laser pulses in vacuum (Fig. 3b), the topography of the surface coating is considerably different. The grains are of a larger size and on the surface of large grains appear much smaller grains. The images from a scanning electron microscope (Fig. 4) show the same differences. Roughness parameters of films were also

measured with a Form Talysurf scanning profilometer. Mean arithmetic deviation was 0.314 μm and 0.557 μm in the case of 18 000 laser pulses in water vapour and 12 000 laser pulses in vacuum, respectively.

3.3. Adhesion

The adhesion of the deposited HA films to the substrate was evaluated by scratch tests. The tests were made with the use of a CSM micro-scratch tester equipped with a Rockwell indenter tip of 200 μm radius. The tip was drawn across the coated surface under progressive loading. The scratch test parameters were as follows: load: 1–70 N, loading rate: 20 N/min, scratch length: 3 mm, scratch speed 0.87 mm/min. Typical results are presented in Fig. 5, which shows the frictional force and the friction coefficient as the normal force increases. The acoustic emission signals were very weak and therefore they are not presented. The characteristic feature of the signals presented in Fig. 5 is that when the load reaches the value at which the HA film becomes cracked or delaminated from the titanium substrate, both the frictional force and the friction coefficient change abruptly. The images obtained during scratch tests were additionally examined under a scanning electron microscope to confirm conclusions drawn from the scratch tester results (Fig. 6).

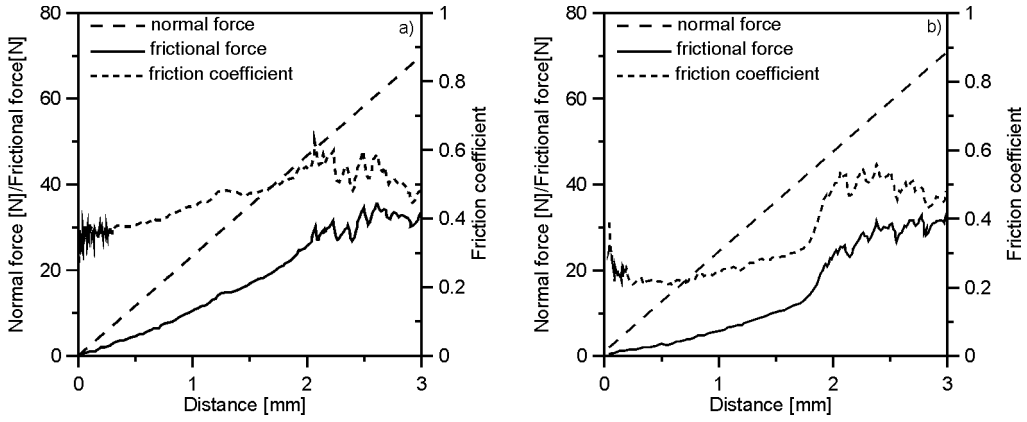

Fig. 5. Scratch tests of HA coatings a) 18 000 pulses, water vapour, b) 12 000 pulses, vacuum

The critical loads at which the first transverse crack lines appear were 43±5 N. Significant differences between the 18 000 pulse coatings deposited in water vapour and the 12 000 pulse coatings deposited in vacuum have not been observed. Before the critical load was reached, the films were only squeezed and dislocated to the sides of the scratching track. No major film delamination was observed in any of the coatings, thereby indicating their high adherence.

The results are encouraging in comparison with those obtained for elevated substrate temperatures. Arias et al. [7] deposited HA coatings in a water vapour atmos-

phere under the pressure of 45 Pa, using an ArF laser at the fluence of 1 J·cm^{-2}. The substrates were heated to 460 °C. All the coatings were 0.9 μm thick. The scratch tests were made using a CSM micro-scratch tester equipped with a Rockwell tip of 200 μm radius. The displacement of films was observed at the load of ca. 10 N.

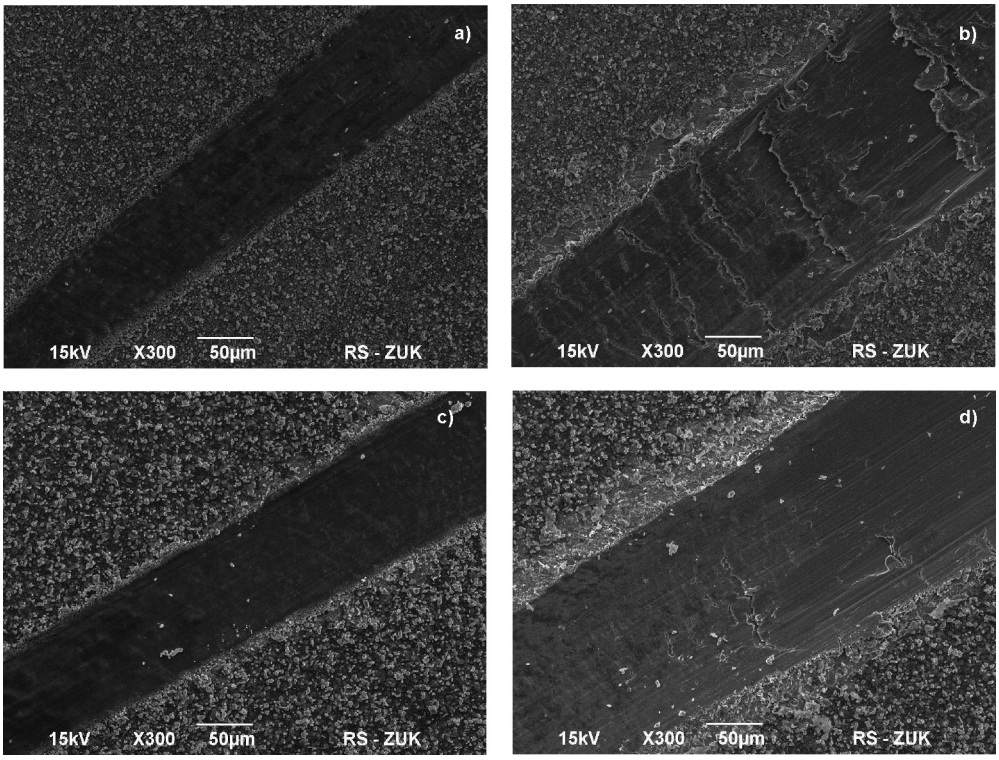

Fig. 6. Scanning electron microscope images from the scratch tests: a) 18 000 pulses, water vapour, d = 0.7 mm, b) 18 000 pulses, view of the transverse crackings at d = 2 mm, c) 12 000 pulses, vacuum, d = 1 mm, d) 12 000 pulses, vacuum, view of the transverse crack lines for d = 1.9 mm

In experiments conducted by Fernandez-Pradas et al. HA coatings were deposited in a water vapour atmosphere under a pressure of 45 Pa using a KrF excimer laser operating at 248 nm at the fluence of 2.3 J·cm^{-2}. The substrates were heated to temperature of 575 °C. The scratch tests were made using a 50 μm radius tip. Film displacements were found to be dependent on the pulse count. The displacements occurred at the loads of 5.7, 2.9, 1.7 and 0.3 N, corresponding to pulse counts of 2000, 4000, 9000 and 18 000, respectively. The thicknesses of these films were 0.17, 0.35, 0.75 and 1.5 μm, respectively. In othe experiments of the same authors [9], HA coatings were deposited in a water vapour atmosphere under the pressure of 10 and 45 Pa using a Nd:YAG laser with the operational wavelength of 355 nm. The laser fluence was 3.1 J·cm^{-2}. The scratch tests were made using a 50 μm radius tip. Crystalline coatings 1–4 μm thick were obtained at the substrate temperatures between 500 °C and

600 °C. Under these conditions the critical loads were about 1 N. In addition, the coatings obtained under the pressures of 10 Pa or 45 Pa, contained either CaO and TetraCP phases (at 10 Pa), or α-TCP phase (at 45 Pa).

Comparison of the results of scratch tests is difficult as the tips in individual experiments have different radii. Very rough estimation can be made based on geometrical similarity [10] which requires equal ratios of the layer thickness to the scratching tip radius. Hence results of the scratch tests of 3–6 μm thick coatings should be compared with those for 0.75–1.5 μm thick coatings scratched with 50 μm tip. Additional condition of equal pressures requires scaling the critical loads with the square of tip radius. This means that critical loads obtained with a 50 μm tip should be multiplied by a factor of 16 to be compared with our results. This scaling leads to a critical load 5–27 N for 1.5 and 0.75 μm thick films obtained in [8] and 16 N for films obtained in [9].

The critical load determined with the use of a 20 μm tip, was 2 N [3]. The authors of the paper do not report the film thickness. However, the experimental conditions (vacuum, laser fluence 4–5 $J \cdot cm^{-2}$) suggest that the films were very thick (over 10 μm) and the results cannot be compared with those obtained in the present work.

4. Conclusions

The results show that satisfactory deposition of thin films of hydroxyapatite can be achieved using an Nd;YAG laser operating at 355 nm. The HA films can be obtained at room temperature, provided post-deposition annealing in ambient air is performed. Such processing makes it possible to obtain good HA films either in ambient water vapour or in vacuum. The crystalline structure of the deposited films is not contaminated by any of the dehydrated forms of HA. The scratch tests showed that HA coatings 3–6 μm thick adhere strongly to the Ti_6Al_4V substrates.

Acknowledgments

This work was partly supported by a Research Project N501 025 31/1604.

References

[1] KOCH C.F., JOHNSON S., KUMAR D., JELINEK M., CHRISEY D.B., DORAISWAMY A., JIN C., NARAYAN R.J., MIHAILESCU I.N., Mater. Sci. Eng. C, 27 (2007), 484.

[2] NELEA V., MIHAILESCU I.M., JELINEK M., *Biomaterials: New Issues and Breakthroughs for Biomedical Applications*, [In:] *Pulsed Laser Application of Thin Films* R. Eason (Ed.), Wiley, Hoboken, 2007.

[3] JOHNSON S., HALUSKA M., NARAYAN R.J., SNYDER R.L., Mater. Sci. Eng. C, 26 (2006), 1312.

[4] NELEA V., RISTOSCU C., CHIRITESCU C., GHICA C., MIHAILESCU I.M., PELLETIER H., MILLE P., CORNET A., Appl. Surf. Sci., 168 (2000), 127.

[5] COTELL C.M., [In:] *Pulsed Laser Deposition of Thin Films*, D.B. Chrisey, G.K. Hubler (Eds.), Wiley, Chichester, 1994.

[6] REHMAN I., BONFIELD W., J. Mater. Sci.: Mater. Medic., 8 (1997), 1.

[7] ARIAS J.L., MAYOR M.B., POU J., LENG Y., LEON B., PEREZ-AMOR M., Biomater., 24 (2003), 3403.

[8] FERNANDEZ-PRADAS J.M., CLERIES L., MARTINEZ E., SARDIN G., ESTEVE J., MORENZA J.L., Biomater., 22 (2001), 2171.
[9] FERNANDEZ-PRADAS J.M., CLERIES L., MARTINEZ E., SARDIN G., ESTEVE J., MORENZA J.L., Appl. Phys. A, 71 (2000), 37.
[10] FISCHER-CRIPPS A.C., *Nanoindentation*, Springer, New York, 2004.

Received 12 January 2010

Materials Science-Poland, *Vol. 28*, *No. 3*, *2010*

Effect of Y^{3+} and Nb^{5+} co-doping on dielectric and piezoelectric properties of PZT ceramics

A. K. ZAK*, A. JALALIAN, S. M. HOSSEINI,
A. KOMPANY, T. SHEKOFTEH NARM

Department of Physics, Materials and Electroceramics Laboratory,
Ferdowsi University of Mashhad, Mashhad, Iran

The effect of co-doping of $Pb_{1-x}Y_x[(Zr_{0.53}Ti_{0.47})_{1-x}Nb_x]O_3$ bulk materials ($0 \le x \le 0.03$) with Y^{3+} ions and Nb^{5+} on their dielectric and piezoelectric properties o was investigated. Samples fabricated by conventional oxide mixing (OM) were sintered at 1250 °C for 2 h in a Pb-rich atmosphere. During the tetragonal–rhombohedral transition in the doped PZT ceramics a negligible effect was observed after additions of Y^{3+} and Nb^{5+} ions. The co-doping with both ions was noted to inhibit grain growth and promote densification and electrical properties. The optimal doping level was found to be at $x = 0.015$, for which the electric permittivity of 907, the piezoelectric constant of 323 pC/N, g_{33} of 40 mV/N, Q_m of 272 and the electromechanical coupling factor (k_p) of 0.49 were obtained.

Keywords: *piezoelectric properties; PZT ceramics; dielectric properties*

1. Introduction

Lead zirconate titanate $Pb(Zr_{1-x}Ti_x)O_3$ (PZT) ceramics of a general formula ABO_3 possess outstanding piezoelectric, pyroelectric and ferroelectric properties [1, 2]. Special attention is given to modified PZT systems having compositions near their morphotropic phase boundaries (MPB), between Ti-rich tetragonal and Zr-rich rhombohedral phases with monoclinic phases [3].

The effect of doping on various physical and chemical properties of this material was identified and extensively exploited to improve the performance of the material. Many aliovalent compositional alterations to PZT have been studied, either with higher valence substitutions (donors) or with lower valence ions (acceptors) [4]. PZT ceramics can be doped with ions to form "hard" and "soft" PZTs. Hard PZTs are doped with acceptor ions such as K^+, Na^+ (for site A) and Fe^{3+}, Al^{3+}, Mn^{3+} (for site B), creating oxygen vacancies in the lattice [5, 6]. Soft PZTs are doped with donor ions

*Corresponding author, e-mail: alikhorsandzak@gmail.com

such as La^{3+} and W^{6+} (for site A) and Nb^{5+}, Sb^{5+} (for site B) leading to the creation of site A vacancies in the lattice [7–10]. Soft PZTs normally have higher permittivity, larger losses, better piezoelectric coefficients and are easy to pole. Thus, they can be used for applications requiring very high piezoelectric properties. Doping PZT ceramic with a small amount of Nb (ca. 2 wt. %) significantly increases the electric permittivity and piezoelectric coefficients [11, 12]. The fatigue behaviour of PZT has also been improved by the addition of Nb [13]. Yttrium doping is another way to improve the properties of PZT ceramics. Li et al. [14] have shown that Y-doped PZT has a large remnant polarization, a small leakage current, and good fatigue endurance. However, very little information is available on the effect of Y^{3+} and Nb^{5+} co-doping on the microstructure and piezoelectric coefficient of PZT ceramics [15].

In this study, we studied the effect of Nb and Y co-doping on the grain size, structure as well as on dielectric and piezoelectric properties of PZT ceramics.

2. Experimental

PbO, ZrO_2, TiO_2, Nb_2O_5, and Y_2O_3 (Merck, >99% purity) were used to fabricate the samples were fabricated according to the formula: $Pb_{1-x}Y_x(Zr_{0.53},Ti_{0.47})_{1-x}Nb_xO_3$ ($0.01 \leq x \leq 0.03$). 5 % wt. excess of PbO was added to compensate for the loss of lead (Pb) during the final heat treatment. The mixed powder was ball-milled for 3 h in ethanol using zirconia balls and a Teflon jar, and then the mixture was dried at 100 °C. Calcinations were carried out at 900 °C for 2 h with the heating rate of 4 °C/min. For granulation, 3 wt. % of poly(vinyl alcohol) (PVA) was added to the PZT powder as a binder which was then pressed into disc-shaped pellets, each having the diameter r of 11 mm and the thickness of ca. 2 mm under the pressure of 250 MPa. The sintering temperature was 1250 °C and the isothermal sintering time was 2 h, under the heating rate of 4 °C/min. The samples were characterized by X-ray diffraction (XRD), and a scanning electron microscope (SEM) was used to study the microstructures of the sintered pellets. The electric permittivity K_{33} was deduced from the capacitance, measured at the frequency of 100 Hz. The specimens were poled for 30 min in silicone oil at 120 °C under the field of 2.5 kV/mm, and they were cooled to room temperature before the electric field was removed. All electromechanical measurements were performed one week after poling. The piezoelectric constant d_{33} was measured with a d_{33} meter (Penne Baker, model 8000, USA) and the voltage constant g_{33} was calculated from the following equation:

$$g_{33} = \frac{d_{33}}{\varepsilon_0 K_{33}} \tag{1}$$

Other piezoelectric parameters such as mechanical quality factor Q_m and coupling factor k_p were calculated from the impedance–frequency curves [16].

$$k_p^2 = \frac{2.54(f_a - f_r)}{f_r} - \left(\frac{(f_a - f_r)}{f_r}\right)^2, \qquad Q_m^2 = \frac{f_a^2}{\left[2\pi f_r Z_r C\left(f_a^2 - f_r^2\right)\right]} \tag{2}$$

where f_a is the antiresonance frequency and f_r is the resonance frequency of disk shape PZT samples.

3. Results and discussion

3.1. XRD patterns

The phase formation and orientation of pure and doped PZT samples were investigated by X-ray diffraction analysis in the range of 20–100°, using CuK_α radiation as shown in Fig. 1.

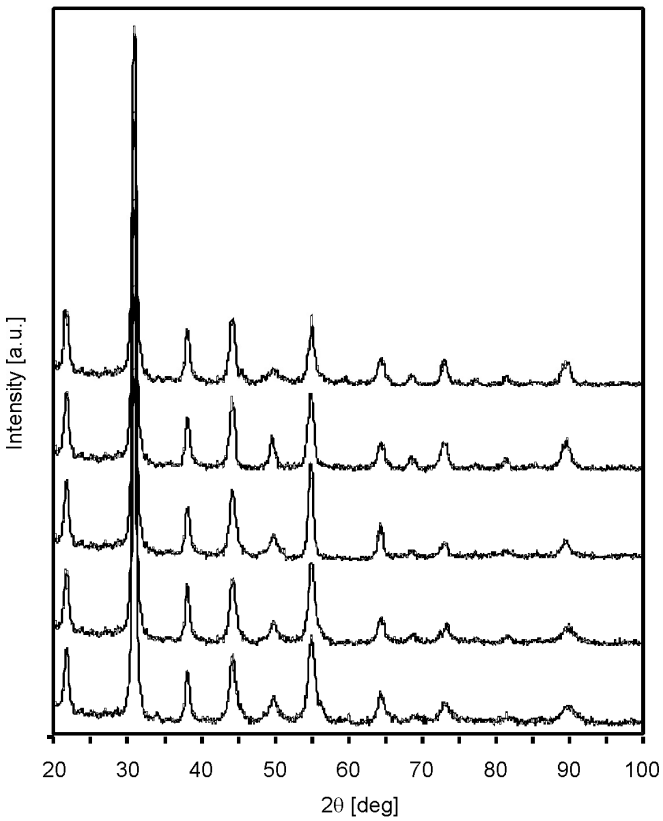

Fig. 1. XRD patterns of $Pb_{1-x}Y_x(Zr_{0.53}Ti_{0.47})_{1-x}Nb_xO_3$ samples: a) $x = 0.0$, b) $x = 0.01$, c) $x = 0.015$, d) $x = 0.02$, and (e) $x = 0.03$

The XRD results reveal the coexistence of a perovskite type tetragonal phase with a rhombohedral one, free from a pyrochlore phase. X-ray patterns show that tetragonality is increased with doping levels $x = 0.01$ and $x = 0.03$, since at $2\theta = 73°$ an extra peak appears next to the main peak [17]. In these cases, the balance between the tetragonal and rhombohedral crystalline phases is disturbed, but tetragonal phase prevails. Maximal tetragonality in doped PZT occurs at $x = 0.01$, and corresponds to maximum intensity of the XRD peaks. Generally, high-piezoelectric activity at the MPB is attributed to the a number of thermodynamically equivalent states, which allows a high degree of alignment of ferroelectric dipoles. Such a high degree of alignment and enhanced polarizability at the MPB results in a dramatic enhancement of dielectric and piezoelectric properties near the MPB. Recently it has been shown that the monoclinic structure could be pictured as providing a bridge between rhombohedral and tetragonal structures, which makes the polarization easier [6].

3.2. Surface morphology

Typical SEM images of pure and doped PZT with Y and Nb ($x = 0.015$) are shown in Figs. 2 and 3. The SEM results indicate that the average grain size of doped PZT is smaller in comparison with pure PZT, and it was found to be about 3μm.

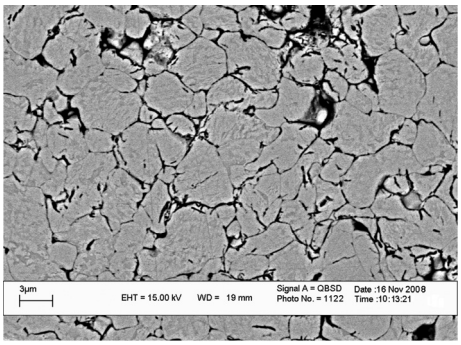

Fig. 2. Typical SEM images of polished and subsequently etched pure PZT ceramics (Zr/Ti ratio 53/47) sintering at 1250◦C for 2 hours

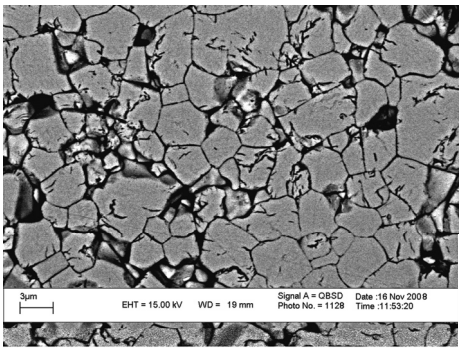

Fig. 3. Typical SEM image of polished and subsequently etched doped PZT ($x = 0.015$) ceramics (Zr/Ti ratio 53/47) sintering at 1250◦C for 2 hours

3.3. Piezoelectric coefficients

Electrical properties such as the electromechanical and piezoelectric properties, were systematically evaluated with respect to the Nb and Y ratio. Table 1 shows the values of the d_{33} piezoelectric coefficient g_{33}, the mechanical quality factor Q_m and the coupling coefficient k_p for various x values of Nb and Y co-doped PZT. In the case of co-doping, the d_{33} and g_{33} coefficients reach a maximum value at $x = 0.015$ and their evolution versus ratio are very similar. The k_p increases as x increases, and reaches

a maximum at $x = 0.02$, then it decreases for higher values of x. The Q_m increases upon x increasing. At room temperature, the optimum value of d_{33} is 323 pC/N and that of k_p is 0.49, corresponding to $x = 0.015$.

Table 1. Dielectric and piezoelectric properties of PZT doped with various elements

Compound	ρ [g/cm^3]	K_{33}	d_{33} [pC/N]	g_{33} [mV/N]	k_p	Q_m
Pb $(Zr_{0.55}Ti_{0.45})_{0.975}Nb_{0.025}O_3$ [4]	–	679	233	–	0.45	122
$Pb_{0.092}La_{0.08}$ $(Zr_{0.55}Ti_{0.45})_{0.975}Nb_{0.025}O_3$ [4]	–	1978	338	–	0.58	73
$Pb_{0.89}(BaSr)_{0.11}(Zr_{0.52}–Ti_{0.48})_{0.99}Mn_{0.01})O_3$+1%F [6]	–	1650	340	–	0.8	–
$Pb_{0.89}(BaSr)_{0.11}(Zr_{0.52}–Ti_{0.48})_{0.99}Mn_{0.01})O_3$ [6]	–	1190	260	–	0.7	–
$Pb_{1.03-x}Y_x[(Zr_{0.52}Ti_{0.48})_{1-x}Nb_x]O_3$ (0.02) [15]	–	1380	–	–	0.6	–
$Pb_{1.03}[(Zr_{0.52}Ti_{0.48})_{1-y}Nb_y]O_3$ ($y = 0.02$) [15]	–	925	–	–	0.48	–
$Pb(Zr_{0.52}Ti_{0.48})_{0.975}Nb_{0.025}O_3$ [17]	–	–	–	–	0.27	–
$0.8Pb(Zr_{1/2}Ti_{1/2})O_3–0.2Pb(Co_{1/3}Nb_{2/3})O_3$ [19]	–	716	–	–	–	–
$0.15[Pb(Ni_{1/3}Nb_{2/3})O_3]–0.85[Pb(Zr_{1/2}Ti_{1/2})O_3]$ +1%Y_2O_3 [20]	7.53	1616	–	–	0.47	128
Present work						
$Pb_{1.03-x}Y_x[(Zr_{0.53}Ti_{0.47})_{1-x}Nb_x]O_3$ (0.0)	7.54	584	190	37	0.37	453
$Pb_{1.03-x}Y_x[(Zr_{0.53}Ti_{0.47})_{1-x}Nb_x]O_3$ (0.01)	7.64	823	309	42	0.44	267
$Pb_{1.03-x}Y_x[(Zr_{0.53}Ti_{0.47})_{1-x}Nb_x]O_3$ (0.015)	7.56	907	323	40	0.49	272
$Pb_{1.03-x}Y_x[(Zr_{0.53}Ti_{0.47})_{1-x}Nb_x]O_3$ (0.02)	7.56	945	218	26	0.50	303
$Pb_{1.03-x}Y_x[(Zr_{0.53}Ti_{0.47})_{1-x}Nb_x]O_3$ (0.03)	7.42	723	206	32	0.30	305

3.4. Densities and electric permittivities

The electric permittivities of the samples are increased after co-doping with Nb and Y, and attain a maximum value of 945 at $x = 0.02$ (Table 1). Initially, the densities of the doped PZT ceramics increase in proportion with the doping level. Maximum density is attained at $x = 0.010$; for higher values of x, the density is inversely proportional to the doping level. The number of Pb vacancies in PZT is closely related to the types and valence of the dopants. This is due to the Pb vacancies that are compensated by electrons produced by the donor dopants [15]. Doping Y^{3+} will create more Pb^{2+} vacancies in order to maintain electroneutrality. As a result, the densification is enhanced and therefore the densities of the doped PZT ceramics are increased for doping levels ranging from $x = 0.01$ to 0.03. The decrease in the density for $x > 0.01$ may be attributed to the decrease in the diffusivity of Pb vacancies, which results from the cation gradients within the PZT grains and/or the dopant segregation at the grain boundaries. Similar results have been reported when other donor dopants were employed [18]. The results were compared with those of other studies (Table 1).

4. Conclusion

We have considered the effect of Y^{3+} and Nb^{5+} co-doping on the dielectric and piezoelectric properties of the $Pb_{1-x}Y_x[(Zr_{0.53}Ti_{0.47})_{1-x}Nb_x]O_3$ ($0 \le x \le 0.03$), namely

(PZT) ceramics. The XRD results reveal the coexistence of a perovskite type tetragonal and a rhombohedral crystalline phases being free from a pyrochlore phase. X-ray patterns show that tetragonality is increased for doping levels $x = 0.01$ and $x = 0.03$, since at $2\theta = 32°$ an extra peak appears next to the main peak. The characterization of ceramic samples showed that significant change in the piezoelectric properties occurs at 0.015 wt. % of dopant in PZT. The optimized piezoelectric parameters were $d_{33} = 323$ pC/N, $K_{33} = 907$, $k_p = 0.49$, $Q_m = 272$, $g_{33} = 40$ mV/N for the modified composition. These parameters were similar to those for the soft PZT materials and are useful for the development of underwater transducers, piezoelectric accelerometers and medical applications.

References

[1] JAFFE B., COOK W.R., JAFFE H., Piezoelectric Ceramics, Academic Press, New York, 1971.
[2] OKAZAKI K., Ferroelectrics, 41 (1982), 77.
[3] BERLINCOURT D., J. Accost. Soc. Am., 91 (1992), 3034.
[4] SINGH V., KUMAR H.H., KHARAT D.K., HAIT S., KULKARNI M.P., Mater. Lett., 60 (2006), 2964.
[5] HIZEBRY A., ATTAOUI H.E., SAADAOUI M., CHEVALIER J., FANTOZZI G., J. Euro. Ceram. Soc., 27 (2007), 557.
[6] BOUCHER E., GUIFFARD B., LEBRUN L., GUYOMAR D., Ceram. Inter., 32 (2006), 479.
[7] HELBIG U., J. Euro. Ceram. Soc., 27 (2007), 2567.
[8] SANTOS D.M., SIMOES A.Z., ZAGHETE M.A., SANTOS C.O., VARELA J.A., LONGO E., J. Mater. Chem. Phys., 103 (2007), 371.
[9] KULCSAR F., J. Am. Ceram. Soc., 42 (1959), 49.
[10] KULCSAR F., J. Am. Ceram. Soc., 42 (1959), 343.
[11] MIURA K., TANAKA M., J. Appl. Phys., 36 (1997), 226.
[12] DIMOS D., SCHWARTZ R.W., LOCKWOOD S.J., J. Am. Ceram. Soc., 77 (1994), 3000.
[13] GRISWOLD E.M., SAYER M., AMM T., Can. J. Phys., 69 (1991), 260.
[14] LI C., LIU M., ZENG Y., YU D., SENS. Actuators A, 58 (1997), 245.
[15] ZHANG R.F., ZHANG H.P., MA J., CHEN Y.Z., ZHANG T.S., Sol. St. Ion., 166 (2004), 219.
[16] GUANG YE Z., *Handbook of Dielectric, Piezoelectric and Ferroelectric Materials*, Woodhead, New York, 2008.
[17] PITICESCU R.M., MITOSERIU L., VIVIANIAND M., POLADIAN V.M., J. Euro. Ceram. Soc., 25 (2005), 2491.
[18] DURRUTHY-RODRÍGUEZ M.D., PÉREZ-FERNÁNDEZ L.D., PELÁIZ-BARRANCO A., CALDERÓN-PIÑAR F., Appl. Phys. A, 95 (2009), 423.
[19] PRASATKHETRAGARN A., UNRUAN M., NGAMJARUROJANA A., LAOSIRITAWORN Y., ANANTA S., YIMNIRUN R., Current Appl. Phys., 9 (2009), 1165.
[20] KANG S.H., LEE D.S., LEE S.Y., KIM I.W., KIM J.S., PARK E.C., Ceram. Inter., 30 (2004), 1453.

Received 20 January 2010

Materials Science-Poland, *Vol. 28*, *No. 3*, *2010*

Synthesis of mesoporous silica by cationic surfactant templating in various inorganic acid sources

W.-D. XIANG[1], Y.-X. YANG[2, 3*], J.-L. ZHENG[2], L. CAO[2], H.-J. DING[2], X.-N. LIU[4]

[1]College of Chemistry and Materials Engineering, Wenzhou University, Wenzhou, Zhejiang 325035, P.R. China

[2]Department of Chemistry, East China University of Science and Technology, 200237, P.R.China

[3]State Key Laboratory of Inorganic Synthesis and Preparative Chemistry, College of Chemistry, Jilin University, Changchun 130012, P.R. China

[4]Analysis Test Center, Yangzhou University, Yangzhou, 225009, P.R.China

Mesoporous silica materials with well-ordered hexagonal structure were synthesized under acidic conditions. The influences of crystallization conditions, aging conditions, acid sources HX and acid/ tetraethyl orthosilicate ratio on the order degree and the morphology have been discussed. The increase of crystallization temperature or crystallization time was beneficial for the condensation of silica species, but had no effect on improving the order degree of mesoporous silica. The order degree of mesoporous materials using various acid sources HX under the same acid concentration swas as follows: HNO_3＞HBr＞ H_2SO_4＞HCl which differed from that in the Hofmeister series; the sulfate anions SO_4^{2-} can play a supporting role on pore structure in the form of space occupation, leading to forming more ordered products than in HCl. Besides, the NO_3^- and Br^- ions showed contrary effect on the growth of micelles, the bigger the pore wall thickness we obtained, the less HBr or the more HNO_3 we used.

Keywords: *mesoporous silica; synthesis conditions; acid source; acidic anions*

1. Introduction

Since the publication by Mobil's scientists,of the first paper on the so-called M41S family of mesoporous molecular sieves with regularly ordered mesopore arrangements and narrow pore size distributions, mesoporous materials have attracted increasing attention due to growing interest in their engineering applications as well as

*Corresponding author, e-mail: yxyang@ecust.edu.cn

in heterogeneous catalysis, ion exchange, adsorption separation and other advanced techniques. So far, various synthetic routes have been developed, including S^+I^- (S^-I^+, $S^+X^-I^+$, $S^-M^+I^-$, SI, NI, etc. [1–4]. Among them, the synthetic routes of well-ordered hexagonal mesoporous silica belong to the S^+I^- and $S^+X^-I^+$ pathways. According to Huo [3] et al., the alkaline route involves direct co-condensation of anionic inorganic species with a cationic surfactant in the S^+I^- pathway. By contrast, the acid route involves condensation of ionic inorganic species in the presence of similarly charged surfactant molecules, this $S^+X^-I^+$ pathway is mediated by counterions of opposite charge to that of the surfactant head group.

It is noted that the synthesis by the S^+I^- route is different from that by the $S^+X^-I^+$ route. As Huo et al. pointed out, the S^+I^- route is carried out in alkaline conditions by self-assembly of anionic silicates and cationic surfactant molecules [3], where $S^+ = C_nH_{3n+1}N^+(CH_3)_3$, n = 8–18, and I^- is the anionic silicate species. The synthesis is performed under conventional hydrothermal conditions, which usually requires that the reaction system be under a liquid self-pressure, and at high temperature for a long reaction time. This will restrict the engineering applications of mesoporous materials.

However, the $S^+X^-I^+$ route achieves self-assembly via a different route from the former, but it uses the same long quaternary ammonium surfactant as a structure-directing agent in acid condition, where $S^+ = C_nH_{3n+1}N^+(CH_3)_3$, $X^- = Cl^-$, Br^-, SO_4^{2-}, NO_3^-, etc., I^+ is a cationic silicate species. As Stucky et al. proposed [5], the ammonium surfactant S^+ is used as a templating agent, but the acid anion X^- plays a role in this route, as it serves to buffer the repulsion between the I^+ and the S^+ by means of weak hydrogen bonding forces in acidic conditions. Thus the $S^+X^-I^+$ route can offer more versatile structures and morphologies than the S^+I^- route, due to its weaker surfactant/silicate interaction in $S^+X^-I^+$, the association of S^+X^- determines the structure and morphology of the mesoporous materials.

It is noted that the acidic system has the pH value lower than 2, the soluble silicate species promote acidic ionization, because their isoelectric point (IEP) is larger than 2 [6, 7]. Thus the mesoporous materials framework is considered as formation via the $S^+X^-I^+$ self-assembly route in acidic media [3]. The advantage of this method is that the reaction system needs no liquid self-pressure, and the high quality mesoporous molecular sieves can be obtained by a reaction of short duration at low temperature.

Although hexagonal close-packing mesoporous silica can be obtained either in alkaline conditions or in acidic conditions, there are lots of differences in both properties such as the pore size, pore wall thickness and pore structure, except that they have the similar crystal symmetry. Stucky [5] proposed that acid synthesis and alkaline synthesis are two different routes via a quite different internal mechansim. At present, less attention is focused on studies of acid synthesis, in contrast to studies of alkaline synthesis. In particular, there have been few comprehensive studies on the conditions of syntheses. Thus in this paper, we discuss experimental factors affecting acid synthesis, including acid sources, the molar ratio of acid/ tetraethyl orthosilicate (TEOS), the temperature and the reaction time, in order to study the influence of various experi-

mental conditions on the order degree and properties of mesoporous materials. Here, we find that ordered mesoporous silica can be synthesized, using a surfactant etyltrimethylammonium bromide (CTAB) templating in a acid medium, by the $S^+X^-I^+$ route at a low temperature of 30 °C, and in a short time ca. 24 h. We attempted to obtain highly ordered mesoporous materials, based on the results of comprehensive tests on various acidic anions.

2. Experimental

Reagents. The following reagents were used: cetyltrimethylammonium bromide (CTAB), nitric acid, hydrochloric acid, hydrobromic acid, and sulfuric acid (all A.R. grade, Shanghai Chemical Reagent Company Ltd., China), tetraethyl orthosilicate (TEOS, Shanghai Chemical Reagent Company Ltd., China).

Synthesis of mesoporous silica. The structure directing agent CTAB was dissolved in HBr(aq.), HCl(aq.), HNO_3(aq.), H_2SO_4(aq.) respectively, with vigorous stirring, followed by slowly adding TEOS in certain proportions. The chemical composition of the mother gel was 1 CTAB : 3.0 TEOS : 18.7 HX : 741 H_2O, where X : Cl^-, NO_3^-, SO_4^{2-}, or Br^-. The resulting mixture was stirred at 30–35 °C and kept static to aging. Then it was cooled down to room temperature (RT). The resulting white precipitate was filtered, washed with deionized water and dried in air at RT. Finally, the product was calcined at 550 °C for 6 h; the temperature was raised from RT to 550 °C under the heating rate of 2 °C·min^{-1}.

Characterization. The powder X-ray diffraction measurements of the mesoporous silica were performed on a D/max 2550 VB/PC X-ray diffractometer, using Ni-filtered CuK_α radiation (40 mA, 40 kV, 1° (2θ) min^{-1}) at RT. The Fourier transform infrared (FTIR) spectrum was recorded on a Nicolet 510P FT-infrared spectrometer, over the spectral range of 4000–400 cm^{-1}, at the resolution of 2 cm^{-1}, using KBr wafers.

The pore images and ordering of mesoporous silica were observed with a JEOL JEM-2100F type transmission electron microscope, operated at 200 kV. The surface morphology of mesoporous silica was observed with a Hitachi s4800 field emission scanning electron microscope, at an accelerating voltage of 15.0 kV. The samples were dispersed in ethanol by sonication and subsequently dropped on carbon microgrids.

Nitrogen adsorption–desorption measurements at 77.4 K were carried out on an ASAP2405 volumetric adsorption analyzer from Micromeritics. Before the measurements, the samples of mesoporous silica were outgassed at 600 °C in the adsorption apparatus, the surface area of the mesoporous silica was calculated, using the BET equation, from adsorption data within the P/P_0 range of 0.05–0.30. The adsorption capability and pore structure of calcined mesoporous silica were calculated from the adsorption isotherms, by the BJH approach.

3. Results and discussion

3.1. Analysis of the experimental process

After a few seconds, when TEOS was slowly added to the acid solution in the presence of CTAB, ivory-white colloidal precipitate was produced which indicates that the TEOS had been hydrolyzed SiO_2 gel formed. The longer the stirring time, the greater the quantity of precipitate produced.

The process has been conducted in two stages: the first stage begins with the TEOS addition and ends when the precipitation process is complete; the second stage starts with the crystallization process and ends with the aging process. During the first stage, a magnetic stirrer must be used for stirring, while during aging process, in the second stage, the sample should be kept static at constant temperature. It was also found that CTAB did not easily dissolve in HBr(aq.), unlike the other three acids.

3.2. The role of crystallization temperature and crystallization time on the mesoporous synthesis

As Huo et al. proposed, well-ordered hexagonal mesoporous silica could be synthesized at room temperature in the acidic medium [3, 7]. It is questionable, however, whether this temperature is optimum with respect to the ordering and properties of mesoporous silica. How will the quality of mesoporous silica be influenced by an increase in the temperature? To answer this question, subsequent discussion shall be based on the results of experimental tests.

Figure 1 shows small angle X-ray powder diffraction (SXRD) patterns of the products synthesized, using HCl and HBr as the acid sources, at various temperatures. The SXRD pattern for the as-made product synthesized using HCl by crystallization at 30 °C shows one strong (100) diffraction peak, $2\theta = 2.14°$, and two weak diffraction peaks, $2\theta = 3.64°$ and $4.24°$ (Fig. 1), which are indexed to the (110) and (200) crystal faces, respectively. The corresponding crystal plane spacing d_{100} was calculated to be 4.12 nm, based on the Bragg formula $\lambda = 2d\sin\theta$. This shows that the sample is strongly representative of a hexagonal symmetry channel structure. The results of indexing of the SXRD pattern with $a = 4.1440$ nm $c = 2.7911$ nm are given in Table 1. HCl was the acid source at 30 °C, the XRD data refer to the as-synthesized sample. d_{exp} is the empirical value for the interplanar spacing, and d_{cal} is the theoretical value of the interplanar spacing, *hkl* are the Miller indices for the hexagonal unit cell. Table 1 shows that all the diffraction peaks in the pattern of the as-made product can be readily indexed by a set of lattice parameters. The largest relative deviation between the theoretical predictions and the experimental data is 0.23%, which indicates that the as-made product, synthesized by crystallization at 30 °C, is a single phase with hexagonal symmetry.

The SXRD patterns for the as-made product synthesized by crystallization at 50 °C and 70 °C all show a strong (100) diffraction peak near 2.52°, corresponding to

the crystal plane spacing of about 3.50 nm; it is evident however that the (100) diffraction peak has been broadened to some extent, and that the (110) diffraction peak is hard to distinguish. For the product crystallized at 90 °C, a poor SXRD pattern was observed, which exhibits a broadening peak with a peak packet near 2.00° in the low-angle region, indicating that the product contains large amount of non-hexagonal phase, and thus the (100) diffraction peak was heavily widened.

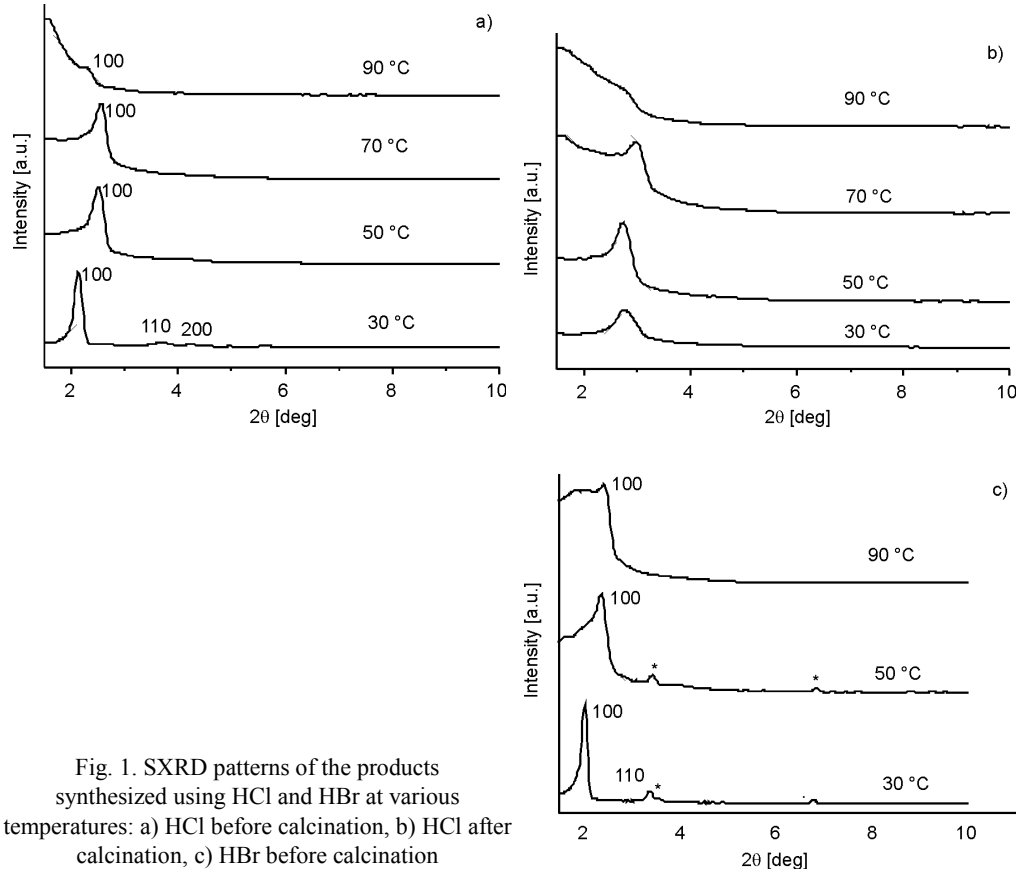

Fig. 1. SXRD patterns of the products synthesized using HCl and HBr at various temperatures: a) HCl before calcination, b) HCl after calcination, c) HBr before calcination

Table 1. The index results of XRD data

2θ [deg]	d_{exp} [nm]	d_{cal} [m]	*hkl*
2.14	4.1249	4.1440	100
3.64	2.4253	2.3925	110
4.26	2.0725	2.0720	200

As a note, according to our analysis presented above, when the crystallization temperature increases from 30 °C to 90 °C and when HCl as the sole source of acid, the crystallization degree of the as-made products obviously becomes lowered, and the pore arrangements of the as-made products become more disordered. By comparing

SXRD patterns of the products synthesized using HCl before and after calcination, as shown in Fig. 1, it can be observed that the peak shape of each calcined product becomes less sharp than that of the as-made product, indicating that the ordering degree decreases. It is probably because a large amount of template is removed after calcination, leading to the inorganic framework collapsing to a different extent.

As can be seen in Fig. 1, the SXRD pattern for the as-made product synthesized using HBr by crystallization at 30 °C shows one strong (100) diffraction peak, $2\theta = 2.02°$, corresponding to a crystal plane spacing of 4.37 nm; and two weak diffraction peaks at $2\theta = 3.52°$ and 4.08°, which are indexed to the (110) and (200) crystal faces, respectively. It is consistent with the reported data regarding the characteristic diffraction peak of MCM-41, and it indicates that an inorganic framework of as-made products is obtained and has a hexagonal mesoporous structure. Furthermore, two undefined weak peaks appear; they are labeled by stars at about 3.40° and 6.70° within the range of $2\theta = 3–7°$. For clarity, an XRD experiment was also performed on CTAB. The results showed two well-defined strong diffraction peaks at about 3.40° and 6.70°, which indicates that the two aforementioned, poorly defined, weak diffraction peaks can be attributed to CTAB. Because of the poor solubility of long hydrophobic chains CTAB in HBr(aq.). the unreacted template separates out during the formation of mesoporous silica.

When the crystallization temperature rises to 50 °C, the as-made product displays one defined (100) diffraction peak at 2.37°, and two peaks of template CTAB, but the peak corresponding to (110) crystal faces is hard to distinguish. One can also observe an apparent broadening of the (100) peak with a peak packet in the low-angle region, when the crystallization temperature reaches 90 °C, indicating the as-made product has a low degree of crystallization. Thus it may be concluded from Fig. 1 that upon increasing the crystallization temperature, the degree of crystallinity and pore order of as-made products becomes lower, if HBr is the sole acid source.

Thus, no matter what source of acid we use, the degree of crystallinity and pore order of the as-made products both decrease upon increasing the crystallization temperature. It is probably because there is an aggregation-dissociation balance between template agent micelles and individual template agent molecules in the synthesis system [7]. When the temperature increases, the molecule thermal movements are accelerated, the molecules of template in micelles are easy to free itself from bound states, and become individual molecules. It leads to the number of micelles decreasing.

In addition, the higher thermal activity of molecules causes instabilities among the micelles, and thus the packing arrangements of micelles become less ordered. When the product is crystallized at 50 °C and 70 °C, the density of the micelles decreases, and the packing arrangements of micelles become slightly disordered. For this reason, the condensation rate of silica species also increases. It leads to the formation of many high polymers of silicon species, even the formation of some amorphous substances among sparse micelles. As a consequence, the SXRD patterns of the as-made product crystallized at 50 °C and 70 °C are broader and less defined than that of the product crystallized at 30 °C.

When the product is crystallized at 90 °C, the packing arrangements of micelles become relatively disordered; the density of micelles in solution obviously decreases as well but the condensation rate of silica species seriously increases. This leads to the formation of quite a large number of amorphous silica among sparse micelles, and thus the SXRD patterns become broader and less distinct, resulting in broadening of the (100) diffraction peak. Consequently, an increase in the crystallization temperature can accelerate the condensation rate of inorganic species, if synthesis is performed in an acid aqueous medium, but it makes no improvement to the quality of the products. On the contrary, it probably causes degradation in the quality of the product.

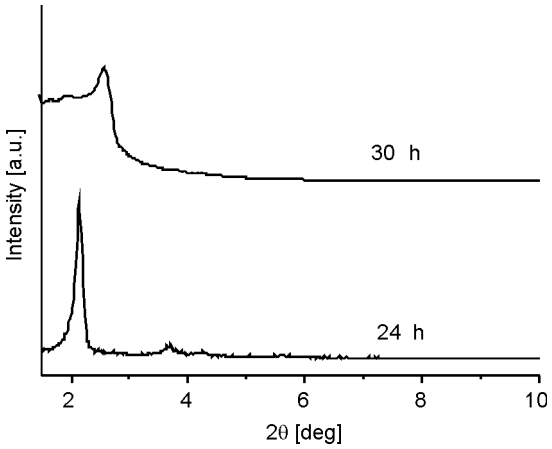

Fig. 2. SXRD patterns of the samples synthesized at various time

Figure 2 shows SXRD patterns of the products synthesized at 30 °C using HCl as the acid source for various durations of crystallization. When the as-made product is crystallized for 24 h, the SXRD pattern displays a well-defined diffraction peak and two weak diffraction peaks in the range of 1.0–10°. Whereas the as-made product is crystallized for 30 h, the SXRD pattern displays a single broadening peak indexed as (100) diffraction, which indicates low order of the product. This demonstrates that a prolonged crystallization time results in a poor degree of crystallinity and low-ordered pore structure of as-made products. It is probably because prolonged crystallization time leads to the deterioration of the mesopore structure [8], and disappearance of the mesoporous features. According to Gao [9], the crystal product may change into amorphous state after prolonged crystallization. This is also noted that the MCM-41 phase is in a metastable state, prolonged crystallization time may cause the system to transform into more stable amorphous state.

3.3. Role of aging temperature and aging time in the mesoporous synthesis

Figure 3 shows SXRD patterns of the products at various aging temperatures with various aging times after crystallization at 50 °C for 30 h, using HBr as the sole source

of acid. It can be seen from Fig. 3 that at comparatively low temperatures (50 °C or 30 °C), no matter how the two factors, aging temperature or prolonging the aging time are changed, the peak profiles in the SXRD patterns can be observed to remain almost unchanged. This indicates the above two factors have no influence on the degree of crystallinity or on the ordering of the pore structure of the products. Because the hexagonal structure of the products has been formed after crystallization for a certain time, so low aging temperature has no effect on the stability of hexagonal arrays of cylindrical micelles, and prolonging the aging time has no significant effect on the degree of crystallinity and ordering of pore structure. This demonstrates that under the precondition of keeping no effect on the stability of the micelles, the ordered hexagonal structure may not be influenced by the condensation of the silicate species.

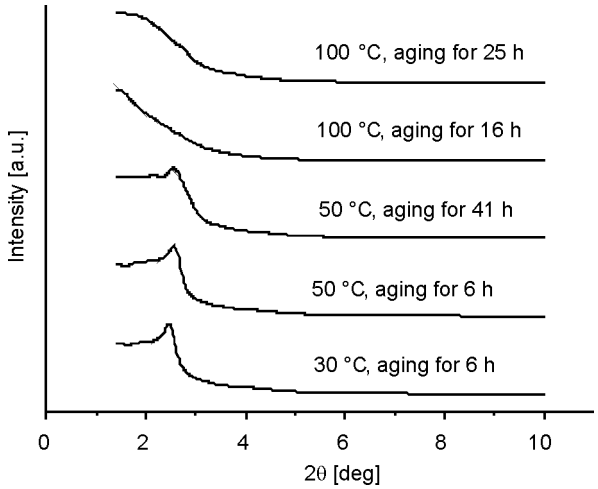

Fig. 3. SXRD patterns of the samples synthesized under various aging conditions

When the crystallized product was transferred to the hydrothermal reactor for aging at 100 °C, the degree of crystallinity and the ordering of the pore structure decreased sharply. As shown in Fig. 3, after aging at 100 °C for 16 h or 25 h, its diffraction peaks in the low-angle region disappeared completely. It occurs because the stability of loose hexagonal arrays of cylindrical micelles may be influenced by a high aging temperature, while the condensation and deposition of silicate species are accelerated if the aging temperature is raised, thereby leading to the decrement of both the degree of crystallinity and the ordering of the pore structure. The results described above demonstrate that the reaction temperature should be limited to 100 °C in acid synthesis, otherwise the order and quality of the mesoporous product will be seriously degraded. This route is different from alkaline synthesis, in which most products are synthesized at temperatures above 100 °C. In the case of alkaline synthesis, high temperatures can feasibly accelerate the condensation of silicate species in the crystallized product, and optimize the degree of long range order. However, in the case of acid

synthesis, such is not the case. In conclusion, high temperature alkaline synthesis is feasible, whereas high temperature acid synthesis is not feasible.

3.4. Acid source with various acidic anions

To study the influence of acidic anions for four various acid sources on the order and quality of the mesoporous product, the mesoporous materials were synthesized by using CTAB as the surfactant and TEOS as a silica source in the presence of various acid sources: H_2SO_4, HCl, HBr, and HNO_3.

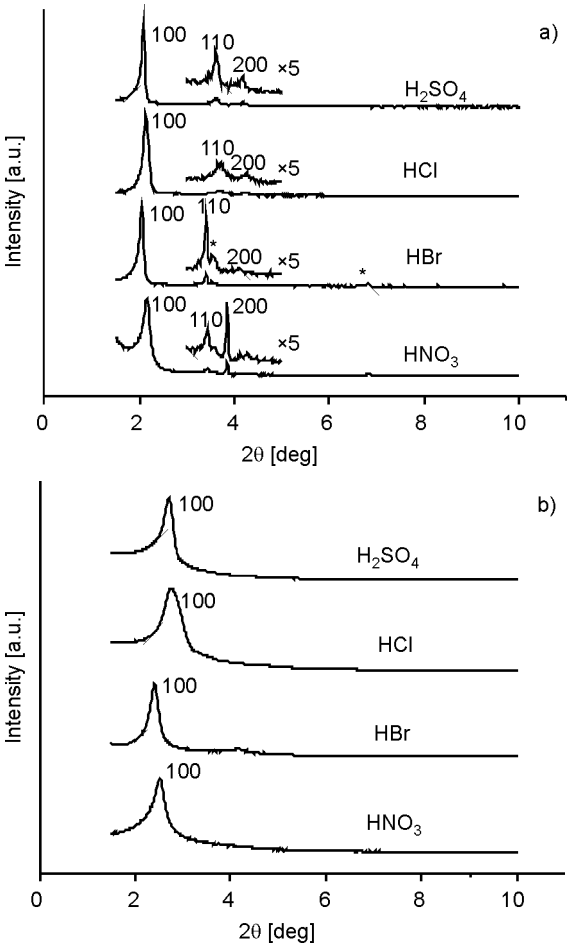

Fig. 4. SXRD patterns of the samples synthesized using various acid sources: a) before calcination (the illustration is locally magnified), b) after calcination

Figure 4 shows the SXRD patterns of the crystallized product at 30 °C before and after calcination. It was found that the synthesis using HBr acid leads to the appearing

a diffraction peak of the template (denoted with the asterisk in Fig. 4a). That is due to poor solubility of the template CTAB in HBr (aq.). Even when CTAB was dissolved in HBr (aq.) under stirring for a long time, there were still some white deposits in the solution, so that a small quantity of undissolved template was mixed with the as-made products. As can be seen from Fig. 4a, all the SXRD patterns of the as-made products display a strong well-defined (100) diffraction peak, and several medium-sized or small peaks in the range of 3–5°, indicating the inorganic framework of the as-made products, which is typical for a hexagonally symmetric channel structure of mesoporous MCM-41.

The order degree of mesoporous materials can be measured from the peak intensity and the half-peak width in low-angle diffraction. As shown in Fig. 4a, when HNO_3 is used as the acid source, the SXRD pattern of the as-made product exhibits a strong, well-defined (100) diffraction peak, and two medium-sized peaks in the range of 3–5°. If HBr is used as the acid source, the resulting product material exhibits a medium-sized peak and a small peak in the range of 3–5°, which are both less intense than those corresponding to HNO_3. If H_2SO_4 is the acid source, a medium peak and a small one are observed beside one strong diffraction peak, showing the low mesoporous order of the product, compared with the HBr sample. However, using HCl acid results in two small peaks in the range of 3–5°, as compared to three products using HNO_3, HBr and HCl. Therefore, the order degree of the mesoporous materials is observed to decrease in the following order: $HNO_3 > HBr > H_2SO_4 > HCl$, which points to unusual anion response, different from the so-called Hofmeister series (from most ordered to least ordered): $NO_3^- > Br^- > Cl^- \sim SO_4^{2-}$ [10].

According to Huo et al. [3, 7], the chief driving force governing self-assembly in an acidic medium is an electrostatic interaction between the positive charged silicon species (I^+) and the cationic micelles (S^+X^-) with the attached counterions (X^-), which can catalyze the condensation of positive-charged silicon species. The higher is the constant of association of counterions with a cationic surfactant, the stronger the association between the (S^+X^-) micelles and the silicon species (I^+), and thus more stable micelles are formed, leading to the formation of more ordered products.

As reported by Lin, at 30 °C the association constants of NO_3^-, Br^- and Cl^- on the CTAB micelles are 0.220, 0.122 and 0.018 respectively [11]. Based on these results, we can conclude that the order degree of our products decreases in the following order: $HNO_3 > HBr > HCl$. It is reasonable and consistent with the above analysis. Unlike three different monovalent anions, the sulfate anions SO_4^{2-}, simple tetrahedral oxoanions, can adopt a number of coordination modes, such as monodentate, bidentate bridging, bidentate chelating, tridentate, and even tetradentate bridging, etc., contributing to the structural diversities of the final networks [12]. In contrary to Cl^- anions, they can act as ligands to form hydrogen bonds with the micelle S^-N^+ and silicates species I^- in several ways, and thus promote growth and stability of micelles, leading to forming more ordered products than those fabricated using HCl.

Figure 4b shows the SXRD pattern of the calcined products by using various acid sources HX (HCl, HBr, HNO_3, H_2SO_4). One can clearly observe that nearly all these products possess one main diffraction peak at (100) crystal face, except the product obtained using HCl. It shows more broadening than the corresponding peak for the as-made product. It probably occurs because a large number of templates are removed when the products are calcined, causing the pore wall of the product obtained with HCl to collapse. Another explanation for the peak-broadening might be asymmetrical condensation of the residual silicon species, resulting from the presence of Cl^- anions and high temperature calcination.

In synthesis, when each initial reactant mole ratio was fixed, the products that had been synthesized using various acid sources had rather rich morphologies. Thus, we can use SEM to compare and study these different morphologies.

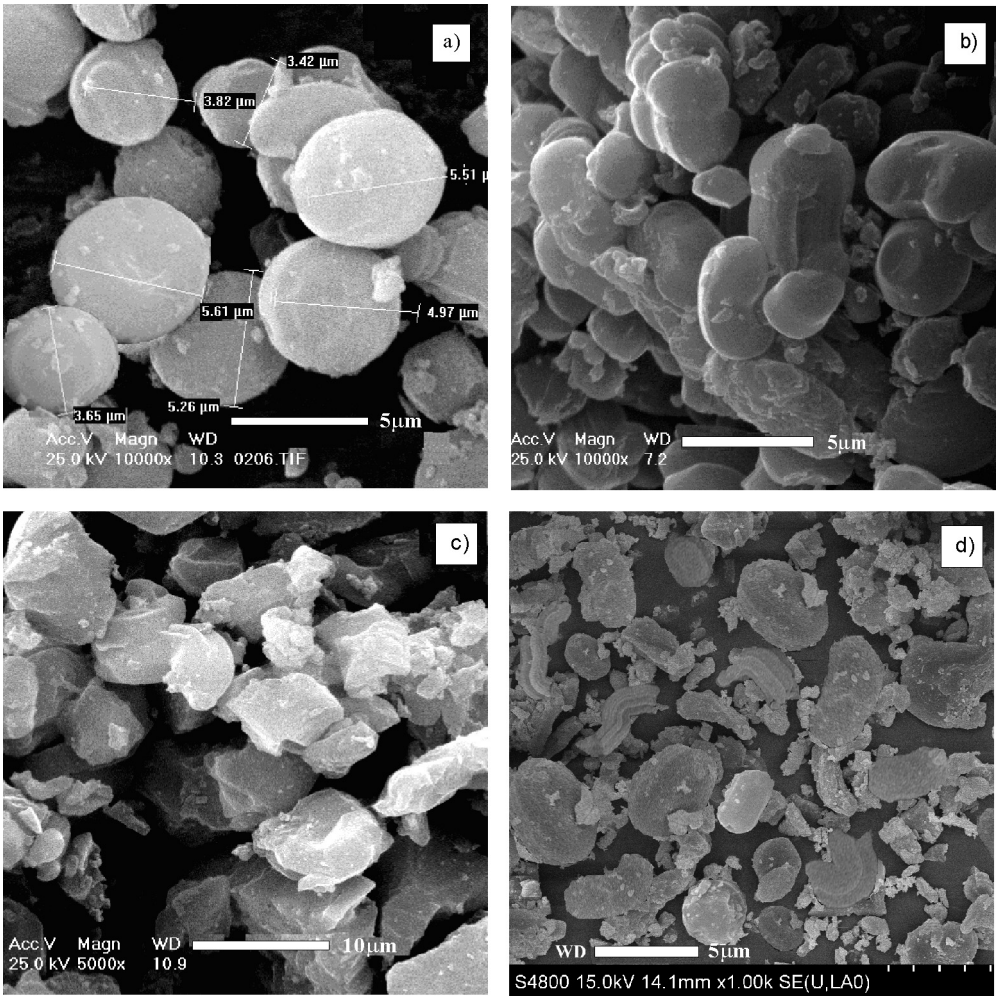

Fig. 5. SEM of the samples synthesized using various acid sources a) HNO_3 b) HBr c) HCl d) H_2SO_4

As we can see from the SEM images shown in Fig. 5, the surface curvature of the products decreased in the following order: $NO_3^- > Br^- > SO_4^{2-} > Cl^-$. For HNO_3, the resulting product consisted of micrometer-sized gyroidal spheres. When HBr was used as the acid source, the product was observed to consist of cashew-like particles. When HCl was used as the acid source, the resulting product appeared the least ordered among all the products obtained with an acid source; Figure 5c shows a disordered block-like structure. When the acid source was H_2SO_4, the resulting product appeared less ordered than the two products obtained with HNO_3 and HBr. The images of the product derived with H_2SO_4 are shown in Fig. 5d: they exhibit a mixture of spherical, ellipsoidal and caterpillar-like shapes of various sizes and non-uniform distributions.

So far, the formation mechanism of incredible morphologies has not been clarified yet, but it is certain that all these morphologies discussed above maybe related to the formation process of interior ordered mesostructures which can be controlled by acidic anionic ions [13]. The following anions are listed in increasing order of their ionic radii: $NO_3^- < Br^- < Cl^- < SO_4^{2-}$. Acidic anions having smaller ionic radii make more associations between the surfactants and the silicates, compared with those having larger anionic radii, so more charges are neutralized, ultimately leading to a more ordered morphology [14].

With HNO_3 as the acid source, NO_3^- ions have the smallest ionic radii among four anionic ions used in the experiment. Therefore, the association of NO_3^- between surfactants and silicates is strongest. The largest amount of charges neutralized would in turn help the formation of gyroidal spheres. By careful observations, we also find that spiral distortion occurs on the surface of the spherical shapes, as shown in Fig. 5a. Maybe because large steric hindrance during the process of micelle formation of NO_3^- induces strong space repulsion between adjacent two layers of micelles, spiral distortion helps to reduce the repulsive effect.

With HCl as the acid source, Cl^- ions have relatively large ionic radii, leading to weak association of Cl^- between surfactants and silicates, and thus less of charge neutralized. As a result, the micelle surface has large charges left, and the lower surface curvature cause the formation of disordered, block-like structures.

According to existing literature, NO_3^- and Br^- anions have stronger binding strength to the surfactant, in comparison with SO_4^{2-} and Cl^- anions. However, the ionic radius of Br^- lies between the ionic radii of NO_3^- and Cl^-. Therefore, during the process of association with surfactants and silicates, the surface charges are partly neutralized, which determines the formation of a cashew-like morphology.

With H_2SO_4 as the acid source, the divalent SO_4^{2-} anions adsorbed on the pore wall preferentially bind with free hydroxyl ions of mesoporous silica. This effectively reduces the number of free hydroxyl ions on the pore wall, and thus prevents the pore structure from collapsing as a result of bonding and dehydration of free hydroxyls. And to certain degree, it also plays a role of structure direction agent. Simultaneously,

space occupation of SO_4^{2-} can play a supporting role on pore structure in several ways due to its different coordination modes, leading to formation of mixture of spherical, ellipsoidal and caterpillar-like structures.

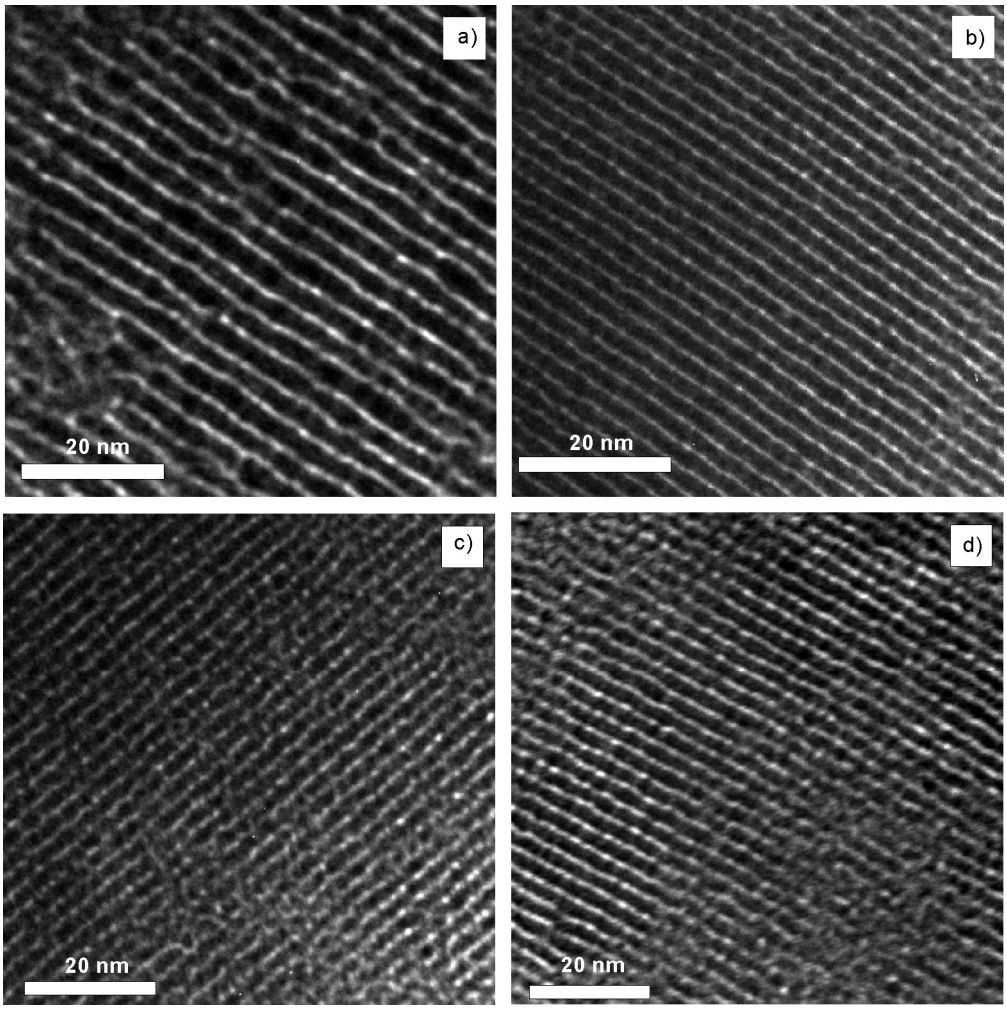

Fig. 6. TEM of the products synthesized using various acid sources a) HNO_3 b) HBr c) HCl d) H_2SO_4

Figures 6a and 6b show that with HNO_3 and HBr, the resulting products all have hexagonal structures. The TEM image shown in Fig. 6 clearly illustrates an ordered arranged pore channel structure with a bend or kink. In the top right hand corner of Fig. 6a, a non-parallel pore channel with kink helices can be observed, which may lead to the formation of micrometer sized gyroidal spheres, shown in Fig. 5a. When HBr is the acid source, the product exhibits a well ordered parallel oriented pore channel structure can be observed along the [110] direction, as the image shown in Fig. 6b

the image clearly shows a large number of hexagonal structure channels and packing along the axis of parallel channel. In a word, the products synthesized with HNO_3 and HBr both present regularly, well-ordered parallel arranged pore channel structure. It is because the strong association interaction between NO_3^-, Br^- and cationic surfactant that favors the stability of the micelles forming.

As shown in Fig. 6c, the TEM image of the product with HCl shows only discontinuous pore channels, indicating low order degree of these samples. But when using H_2SO_4 as acid sources, an ordered parallel pore channel can be seen in Fig. 6d, except for a part of discontinuous channels shown in the lower right corner. It thus leads to a conclusion that the order degree of our products decreases as follows: $HNO_3 > HBr > H_2SO_4 > HCl$, in a good agreement with the conclusion based on XRD and SEM analyses.

To investigate the effect of the acid source on the pore size of the products and the shrinkage of cells in the product after calcination, nitrogen adsorption–desorption measurements at 77.4 K were carried out on an ASAP2405 volumetric adsorption analyzer from Micromeritics. The adsorption capability and pore structure of calcined mesoporous silica were calculated from the adsorption isotherms obtained by the BJH method.

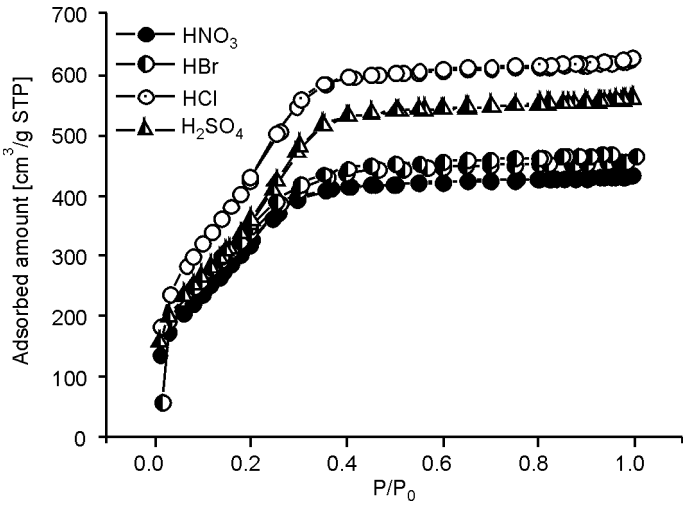

Fig. 7. Sorption isotherms of the products synthesized using various acid sources

In Figures 7 and 8, N_2 sorption isotherms of the products are shown, using various acid sources, all belonging to standard type IV at the relative pressure P/P_0 of 0.01–0.99, showing the presence of mesopores. The measured Brunauer–Emmett –Teller surface areas (S_{BET}) of the products derived with HNO_3, HBr, HCl and H_2SO_4 as acid sources are 1297, 1309, 1661 and 1466 m^2g^-, respectively. Their pore volumes (V_p) are 0.9021, 0.6901, 0.9598 and 0.8571 $cm^3 \cdot g^{-1}$, respectively.

The physisorption isotherm of the products derived with HNO_3, HBr, H_2SO_4 and HCl all show hysteresis loops. The two branches in the isotherm remain nearly horizontal and parallel over a wide range of relative pressures between 0.30 and near saturation, indicating inkbottle type mesopores. Rapid change in the amount of N_2 sorption causes only minor variation in the corresponding relative pressure, indicating a relatively narrow distribution of pore sizes in the three products.

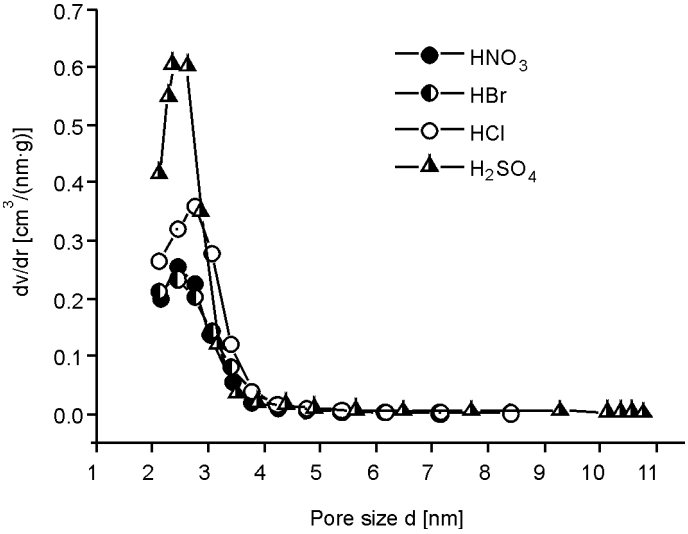

Fig. 8. Pore size distributions of the products synthesized using various acid sources

As can be seen in Fig. 7, the capillary condensation occurred in the pore channel of product with HNO_3, HBr, H_2SO_4 and HCl was located at various middle parts of adsorption isotherms, the location of them moved from low to high values of P/P_0 in the incremental order: $HNO_3 \approx HBr < H_2SO_4 < HCl$, so the product derived with HCl showed a large hysteresis loop at high P/P_0, which is generally indicative of a large pore size.

As can be seen in Fig. 8, the product derived with H_2SO_4 exhibits the strongest peak among all products derived from the four considered acid sources. The product derived with HCl shows a stronger peak than for the products derived with HNO_3 or HBr, near the 2.70 nm radius. This indicates that the product derived with H_2SO_4 has the highest percentage of small pores, and that the product derived with HCl, and the second highest percentage small pores. The percentages of pores of most probable sizes in the products with HNO_3 and HBr were calculated about 71.3% and 68.4% respectively, while the percentage in products with HCl and H_2SO_4 were calculated about 85.6% and 91.6%, respectively.

It was also found that the pore diameter of the product derived with HCl is 2.74 nm, thus it is larger than the pore diameters of the products derived with other

acids, namely 2.44 nm, in the case of HNO_3 and HBr, and 2.52 nm for the product derived with H_2SO_4.

Thus it can be seen that the pore sizes and pore volumes of synthesized products are different for various acid sources. The detailed parameters of pore structure measured by N_2 sorption-desorption isotherms are given in Table 2, where D is the pore size, L – pore wall thickness ($L = a_0 - D$), a_0 – the unit cell constant ($a_0 = 2d_{100}/3^{1/2}$), d_{100} is the interplanar spacing of the synthesized products after calcination. The Δd_{100} value shows shrinkage of a cell after calcination due to template removal and silicon species polycondensation in the pore wall. When polycondensation degree of silicon species is low in mesoporous material formation, a looser pore wall tends to be formed, and thus results in a larger Δd_{100} value.

Table 2. Porous properties of synthesized products on pore size, surface area and pore wall thickness with various acid source

Product identifier	Before calcination		After calcination		$\Delta d100$ [nm]	a_0 [nm]	S_{BET} [m^2/g]	V_P [cm^3/g]	D [nm]	L [nm]
	2θ [deg]	d_{100} [nm]	2θ [deg]	d_{100} [nm]						
HNO_3	2.142	4.121	2.487	3.549	0.572	4.098	1297	0.9022	2.440	1.658
HBr	2.018	4.374	2.413	3.658	0.716	4.224	1309	0.6901	2.440	1.784
HCl	2.119	4.166	2.786	3.169	0.997	3.659	1661	0.9598	2.740	0.919
H_2SO_4	2.096	4.211	2.684	3.289	0.922	3.798	1466	0.8571	2.523	1.275

Basically, we find that all of these mesoporous materials exhibit large surface areas (ca. 1300 m^2/g) and uniform pore sizes. Furthermore, the pore sizes can be adjusted by changing the acid source used in the synthesis. The d spacings vary with the choice of the acid source; by comparing the decrement in the d_{100} value after calcination at 550 °C, one can observe that the decrement, (Δd_{100}), in the d_{100} value for the HNO_3 product is only about 0.572 nm smaller than the corresponding decrements for the other acids (about 1.0 nm). While the pore wall thickness (L) for the HNO_3 product appears to be large, as presented in Table 2, it indicates that the strongly adsorbed NO_3^- ion catalyzes more effectively condensation of silicon species and facilitates the formation of a stronger wall for the hexagonal structure in mesoporous silica. It was also found that Δd_{100} for the HBr product is about 0.716 nm smaller than for HCl and H_2SO_4 ones, indicating that the negative species Br^- binds more strongly to the surfactant than either Cl^- or HSO_4^-. The Δd_{100} for the HCl product shows the largest value, yet the pore wall thickness of the HCl product apparently decreases, further demonstrating that Cl^- binds the most weakly to the surfacant.

The parameter Δd_{100} of the H_2SO_4 product is slightly lower than for the HCl product. The pore wall thickness for the H_2SO_4 product appears to be larger than for the HCl product. This indicates a stronger binding of the negative species SO_4^{2-} to the

surfactant, compared with the binding of Cl^- to the surfactant, and it is in very good agreement with the SXRD results.

In order to study the coordination properties of SO_4^{2-} and Cl^- anions to the silicate species I^-, we also performed IR experiments on the products made with HCl and with H_2SO_4. The spectra of these two as-made products are shown in Fig. 9.

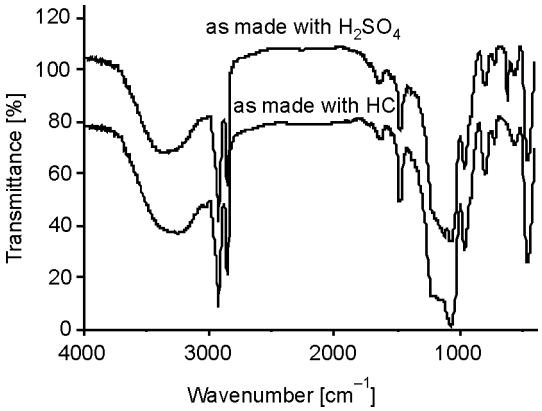

Fig. 9. Infrared spectrum of two as-made products

The IR spectra of the two as-made products are relatively similar and broad bands corresponding to stretching vibration of the Si–OH group at 3371 cm^{-1} and sharp bands to asymmetric Si–O–Si stretching vibrations at 1073 cm^{-1} occur in both spectra. The symmetric Si–O–Si stretching vibrations occur at 801 cm^{-1}, whereas the Si–O–Si bending modes at 458 cm^{-1}. Thus, the IR spectra indicate that the products must be the silica.

As can be seen in Fig. 9, the two as-made products also display two distinct peaks corresponding to CH_2 and CH_3 groups of CTAB at 2930 cm^{-1} and 2852 cm^{-1}, and to three stretching vibrations of CH_2 at 1633 cm^{-1}, 1482 cm^{-1} and 728 cm^{-1}. Also, a weak band at 564 cm^{-1} can be attributed to the Br^- of CTAB, indicating the presence of surfacant in the as-made product. In contrast to the IR spectra of the as-made product with HCl, the as-made product with H_2SO_4 also displays two weak bands of SO_4^{2-} occurring at 1129 cm^{-1} and 620 cm^{-1}, which illustrates that SO_4^{2-} acidic anions were actually involved in a templated self-assembly process of mesoporous material. But there is no evidence of Cl^- bands in Fig. 9; perhaps this is because only a very small number of Cl^- acidic anions participated in the actual formation of the mesoporous material, a number so small that their presence is not detectable by the infrared sensor. The results demonstrate that SO_4^{2-} acidic anions show stronger binding to the as-made product than the Cl^- acidic anions.

According to Huo and Yokoi et al. [3, 15], quaternary cationic surfactants CTAB can associate the acidic anions (X^-) to form S^+X^- micelles in an acidic environment, which can catalyze the condensation of the positive-charged cationic silicate species

(I^+). Thus the mesostructure formation of S^+X^-–I^+ mesoporous intermediates is driven by the electrostatic interaction of the positive-charged silicate species (I^+) and micelle association of the S^+X^- in this paper. The divalent anions SO_4^{2-} can act as ligands, to form hydrogen bonds with the micelle S^+ as well as the silicates species I^+, which perhaps enhances the interaction between I^+ and S^+X^-. However, the Cl^- anions as negative counter-ions, are different from the SO_4^{2-} anions; they have a shielding effect for the positive charge on the S^+ micelle surface due to the polarizability of Cl^- anions [16]. This causes the strength in counter-ion binding of Cl^- to S^+ micelles less than that in counter-ion binding of SO_4^{2-} to S^+ micelles. On the other hand, the anions SO_4^{2-}, as negative counterions, also have a shielding effect for the positive charge on the S^+ micelle surface [17], leading to weaker binding of the negative species SO_4^{2-} to surfactant than that of NO_3^- and Br^- to surfactant. Now, this leads to conclusion that the series orders ions with increasing the strength in counter-ion binding to micelles of CTAB from left to right under the same acid concentration, and is as follows: Cl^-, SO_4^{2-}, Br^-, NO_3^-, instead of so-called Hofmeister series orders SO_4^{2-}, Cl^-, Br^-, NO_3^-.

Next, we investigated the influence of various acid contents on the products. We studied the acid systems HNO_3 and HBr for they all have the strongest binding tendency. At a HA/TEOS molar ratio between 1 and 3, the influence of acid contents is more apparent. The N_2 adsorption studies were performed with the same instrumentation to investigate the influence of the acid content on pore size of the products.

3.5. Role of acid contents

As can be seen from Figs. 10 and 11, the crystallinity degree and structure ordering of two products using HA (HNO_3, HBr) all increase as the molar ratio of HA to TEOS ranges from 1 to 3 in the low-angle region, which is in accordance with the report of Zhang et al [18]. In this study, we also found that increase of the HNO_3 content resulted in an enlargement of the *d* spacing of the X-ray d_{100} peak. This enlargement corresponds to the two strong peaks, related by hexagonal symmetry, which appear in the SXRD pattern. But incremental addition of HBr content resulted in a decrease in *d* spacing of the X-ray d_{100} peak, whereas low HBr content resulted in an apparent broadening (100) peak with a peak packet in a low-angle region. This is because various anions in HA can interact with TEOS to modify the rates of hydrolysis and particle nucleation, affecting the final particle size and the extent of cationic silicate species condensation in the materials, leading to different properties of surfaces and morphologies of the final products [19].

Nnitrate anions possess a higher charge density than bromide anions [10] and they also are characterized by π electronic structure, forming hydrogen bonds with the micelle S^-N^+ and silicon species I^- by bidentate bridging [16]. Consequently they can reduce the repulsion between the surfactant headgroups, and thus affect contraction of

micelle in solution. This leads to decreasing radii of micelles as the HA/TEOS ratio increases. However, bromide anions, as heavier halogen ions, show correspondingly stronger π back-donation [20, 21], they can form the d-pπ back-donation, accepting the electron from nitrogen element in the $(CH_3)_3\overset{+}{N}-$ groups of micelle S^-N^+, which makes the surfactant headgroups more positive. This may produce more repulsive force between head groups, and thus affects expandability of micelle in solution, leading to radius of micelle increasing as HA/TEOS ratio increases. The results shown in Tables 3 and 4 can confirm these conclusions.

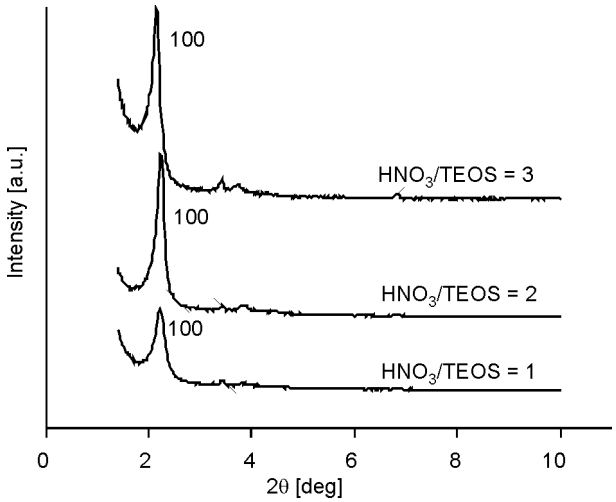

Fig. 10. SXRD patterns of the samples with HNO_3 at various HA/TEOS ratios

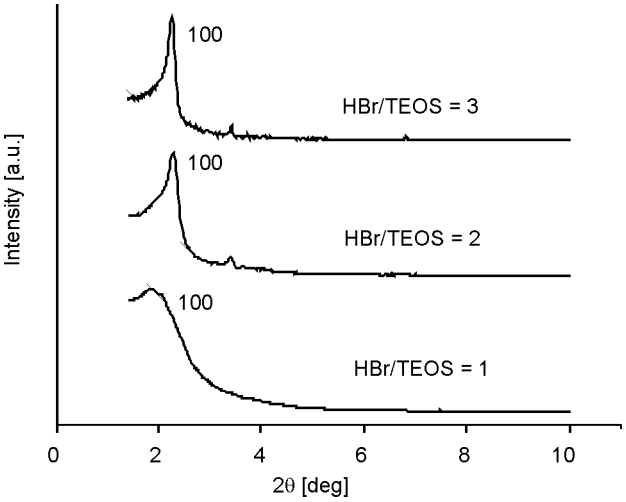

Fig. 11. SXRD patterns of the samples with HBr at various HA/TEOS ratios

Table 3. Porous properties of the samples with HNO_3 at various HA/TEOS ratio

HNO_3 /TEOS	Before calcination		After calcination		Δd_{100} [nm]	a_0 [nm]	S_{BET} [m^2/g]	V_P [cm^3/g]	D* [nm]	L* [nm]
	2θ [deg]	d_{100} [nm]	2θ [deg]	d_{100} [nm]						
3	2.141	4.123	2.514	3.511	0.612	4.054	1691	0.9297	2.555	1.499
2	2.210	3.994	2.560	3.448	0.546	3.981	1782	0.9410	2.493	1.488
1	2.278	3.875	2.611	3.381	0.494	3.904	1316	0.7462	2.820	1.084

Table 4. Porous properties of the samples with HBr at various HA/TEOS ratio

HNO_3 /TEOS	Before calcination		After calcination		Δd_{100} [nm]	a_0 [nm]	S_{BET} [m^2/g]	V_P [cm^3/g]	D [nm]	L [nm]
	2θ [deg]	d_{100} [nm]	2θ [deg]	d_{100} [nm]						
3	2.266	3.896	2.588	3.411	0.485	3.939	1119	0.7950	2.693	1.125
2	2.263	3.901	2.514	3.511	0.390	4.054	1388	0.7275	2.456	1.598
1	1.838	4.802	1.979	4.460	0.342	5.150	1302	0.7224	2.507	2.643

By comparing the decrement of the d_{100} value (Δd_{100}) of the product before and after calcination in Tables 3 and 4, one may conclude that its value does not depend on the acid type but only on the acid content. Because the decrease of the unit cell before and after calcination is originated from condensation of silicate species in pore wall, thus the higher the condensation degree of the product before calcination, the more compact the pore wall is, and thus the lower the value of Δd_{100}. It leads to conclusion that decreased acid content favours the condensation of the inorganic species. As is known, in the acid synthesis system, the acidic medium plays a dual role. It not only promotes the hydrolysis of TEOS, and protonation of oligomeric silicate species but also produces anions of X^- in the surface layer of the electrical double layer structure. For these reasons, when the acid content is decreased, the electric charge density of oligomeric silicate species decreases, leading to static electric repulsion decreasing between the silicate species. This favors crosslinking and condensation between them, resulting in a compact pore wall, and a decrease of Δd_{100}. On the other hand, a decrease of concentration of anions of the electrical double ayer structure can decrease drive force of the silicate species aligning along template micelles, and this goes against assembly of organic-inorganic interface. In short, the two factors make self-condensation rate of inorganic species apparently higher than the assembly rate along the template surface, thus this results in a considerable amount of SiO_2 high polymer producing among the assembled template micelles, even the amorphous products being formed. Consequently, the quality and the ordering degree of the product decrease inevitably.

4. Conclusion

Increase of the crystallization temperature and the crystallization time are beneficial for the condensation of silica species, but have no effect on improving the order of products in acid conditions. The order degree of mesoporous materials with various acids is as follows: $HNO_3 > HBr > H_2SO_4 > HCl$, which seems to be different from the Hofmeister series NO_3^-, Br–, Cl–, SO_4^{2-}. The products consist of micrometer sized gyroidal spheres, cashew like, and disordered block like structures, corresponding to the products derived with HNO_3, HBr, and HCl. However, SO_4^{2-} anions can enhance the pore structure in several modes, leading to the formation of a product which consists of a mixture of spherical, ellipsoidal and caterpillar like structures. Various acid contents are another key factor affecting the order and pore size of products. With increasing acid contents, the ordering of products increases, but the pore size of product with HNO_3 decreases, while with HBr increases accordingly.

Acknowledgements

The authors are grateful for the financial support provided by the National Natural Science Foundation of China (Grants Nos. 20971043, 50772075), the Open Project Program of State Key Laboratory of Inorganic Synthesis and Preparative Chemistry, Jilin University.

References

[1] KRESGE C.T., LEONOWICZ M.E., ROTH W.J., VARTULI J.C., BECK J.S., Nature, 359 (1992), 710.
[2] BECK J.S., VARTULI J.C., ROTH W.J., LEONOWICZ M.E., KRESGE C.T., SCHMITT K.D., CHU C.T.W., OLSON D.H., SHEPPARD E.W., J. Am. Chem. Soc., 114 (1992), 10834.
[3] HUO Q., MARGOLESE D.I., CIESLA U., FENG P., GIER T.E., SIEGER P., LEON R., PETROFF P.M., SCHFITH F., STUCKY G.D., Nature, 368 (1994), 317.
[4] TANEV P.T., PINNAVAIA T.J., Science, 267 (1995), 865.
[5] HUO Q., MARGOLESE D.I., CIESLA U., DEMUTH D.G., FENG P., GIER T.E., CHMELKA B.F., SCHUTH F., STUCKY G.D., Chem. Mater., 6 (1994), 1176.
[6] ILER R.K., *The Chemistry of Silica*, Wiley, New York, 1979, pp. 489, 644, 651, 674.
[7] YANG Y., ZHANG J., YANG W., WU J., CHEN R., Appl. Surf. Sci., 206 (2003), 20.
[8] GAO X.H., MAO X.W., TANG R.R., ZHANG Y.M., SHEN S.K., Acta Petrolei Sinica (Petroleum processing section), 14 (1998), 17.
[9] WANG J., VINU A., COPPENS M.-O., J. Mater. Chem., 17 (2007), 4265.
[10] LEONTIDIS E., Curr. Opinion Coll. Inter. Sci., 7 (2002), 81.
[11] LIN H.P., KAO C.P., MOU C.Y., LIU S.B., J. Phys. Chem. B, 104 (2000), 7885.
[12] SUNA Y.-Q., YANG G.-YU, Dalton Trans., 34 (2007), 3771.
[13] LIN H.P., MOU C.Y., Accounts Chem. Res., 35 (2002), 927.
[14] XU R.R., PAN W.Q., *Chemistry. Zeolites and Porous Materials*, Science Press, 2004, p. 614.
[15] YOKOI T., YOSHITAKE H., YAMADA T., KUBOTA Y., TATSUMI T., J. Mater. Chem., 16 (2006), 1125.
[16] YANG Y.-X., HUANG Z., DENG W.-J., SHAO J.-G., CHEN Y.-R., LIU X.-N., Microp. Mesopor. Mater., 116 (2008), 267.
[17] YANG Y.-X., ZHANG J.-B., LIU X.-N., CHEN Y.-R., JIA X.-C., J. Amer. Ceram. Soc., 90 (2007), 2050.
[18] ZHANG Z.R., SUO J.S., ZHANG X.M., LI S.B., Acta Phys.-Chim. Sin., 14 (1998), 243.

[19] PALMQVIST A.E.C., Curr. Op. Coll. Int. Sci., 8 (2003), 145.
[20] GREENWOOD N.N., EARNSHAW A., *Chemistry of the Elements*, 2nd Ed., Butterworth-Heinemann, Jordan Hill, Oxford, 1984, pp. 195–196.
[21] MIESSLER G.L., TARR D.A., *Inorganic Chemistry*, 3rd Ed., Pearson, Prentice Hall, Upper Saddle River, NJ, 1991, pp. 154–157.

Received 20 January 2010
Revised 16 September 2010

Materials Science-Poland, *Vol. 28*, *No. 3*, *2010*

Atomic layer deposition of HfO_2 investigated in situ by means of a noncontact atomic force microscopy

K. KOLANEK*, M. TALLARIDA, D. SCHMEISSER

Brandenburg University of Technology, Department of Applied Physics and Sensors,
Konrad-Wachsmann-Allee 17, 03046 Cottbus, Germany

An ultra high vacuum atomic force microscope operating in a noncontact mode has been employed to investigate *in situ* atomic layer deposition (ALD) of HfO_2. Tetrakis-di-methyl-amido-Hf and H_2O were used as precursors and the deposition process was performed on $Si(001)/SiO_2$ substrate maintained at 230 °C. The relation between the film growth and the root mean square surface roughness was studied after each ALD cycle. The histograms of the initial stages of the ALD process have been compared in terms of the surface height data as a way of characterizing the growth process. Parameter values corresponding to HfO_2 layer thickness and coverage were calculated. A detailed analysis of the surface height histograms allowed one to construct a simplified growth model and confirm the completion of the first HfO_2 layer after four ALD cycles.

Keywords: *atomic layer deposition; high-k dielectric thin films; atomic force microscopy*

1. Introduction

High-*k* hafnium based gate dielectric materials are the main components allowing improvement in the miniaturization of advanced integrated circuits, particularly complementary metal oxide semiconductor devices [1–3]. Fabrication of high-*k* layers with thicknesses that measure just a fraction of a monolayer can be achieved by the atomic layer deposition (ALD) technique [4, 5]. ALD is a repeated deposition and oxidation process allowing conformal, homogeneous, controlled growth of ultrathin films [6]. The evolution of surface texture occurring in the initial stages of the ALD process is still not known, although several growth models exist [7–9].

In most cases, experimental data obtained *ex situ*, may suffer from sample contamination that may significantly distort properties of materials. We recently proposed An *in situ* technique has been proposed for measuring the early stages of ALD growth by means of synchrotron radiation photoelectron spectroscopy [10]. For the study

*Corresponding author, e-mail: kolanek@tu-cottbus.de

demonstrated in this paper, the ALD reactor was attached to an ultra high vacuum (UHV) atomic force microscope (AFM). By means of this setup, the substrate was transferred into an AFM measurement chamber without breaking the vacuum and the surface topography was measured in the cycle by a cycle routine.

Outstanding resolution in real space is routinely achieved by a powerful technique of frequency-modulation (FM) AFM [11–14]. In this paper, the application of FM -AFM has been applied to topography measurements of the initial stages of ALD growth. The deposition process was started on SiO_2/Si(100) substrate and 4 ALD cycles were completed. Both the root mean square (RMS) surface roughness and surface height histograms were used to analyze the growth process. Based on the surface height histogramdata fitted with Gaussian functions, it was shown that RMS surface roughness is closely related to the standard deviation of the surface height. The RMS surface roughness measured in early stages of the ALD process can be correlated with existing models [15, 16]. Upon undertaking a detailed analysis of the surface height histograms, it was possible to develop a simplified model of the HfO_2 growth.

2. Experimental

Sample preparation. Chemically oxidized Si(001) p-type substrate with a 2.2 nm SiO_2 layer was used for sample preparation. The sample was sonicated in spectrophotometric grade water for 120 s and dried with pure nitrogen. Then it was immersed in commercially available diluted 0.1 M HF solution for 120 s, again cleaned in spectrophotometric grade water for 20 s and dried in nitrogen. Subsequently, within one minute, the substrate was placed in the UHV chamber, via the fast-entry loadlock. Synchrotron radiation photoelectron spectroscopy tests of the samples revealed that after etching the mean thickness of the SiO_2 layer was reduced to ca. 0.5 nm (not shown).

The ALD reactor was equipped with valves for introducing the Hf-precursor and the oxygen source, with a current feed-through for the direct heating of the sample, and a manipulator for transferring the sample into the AFM measurement chamber. During the growth process, the substrate temperature was maintained at 230 °C and the whole ALD reactor was heated to 60 °C. The pulse duration for tetrakis-di-methyl -amido-Hf (TDMAHf) was 1 s, under the pressure of 1×10^{-3} mbar, and for H_2O 2 s, at 1×10^{-2} mbar. During the process, TDMAHf was heated to 60 °C. After each exposure to TDMAHf and H_2O, the chamber was purged for 1 s with N_2 under the pressure of 1×10^{-2} mbar. The duration of one complete cycle was 45 s.

Noncontact AFM measurements and topography analysis. Omicron large sample beam deflection UHV/AFM operated in a FM mode was used for topography measurements at ambient temperature. Silicon cantilevers, with typical tip radius-of-curvatures of less than 7 nm, were utilized. The average spring constant and resonance frequency were about 42 N/m and 320 kHz, respectively. The images were recorded

under the scan frequency of 1 Hz with the resolution of 256×256 pixels. For each ALD cycle, we measured 3 AFM images at various positions, and also with various scan areas. The scanning probe image processor (SPIP, Image Metrology, Denmark) was used for the AFM data analysis.

For AFM data analysis, the most commonly applied parameter is the RMS surface roughness S_q, which equals the standard deviation of the surface height, and thus it describes the spread of the surface height histogram, also called the height distribution (HD), around the mean value. A Gaussian or near-Gaussian surface HD is expected to result from an entirely random ALD process. An analysis of the HD can be applied to extract additional information about ultrathin film growth in ALD process. This is especially valid in the early stages of ALD growth before the completion of the first HfO_2 layer.

A multi-normal probability procedure that finds the parameter values of the Gaussian peaks in the surface topography was proposed by Cogdell [17]. The procedure can be used for surface characterization, once it has completed the task of HD data-fitting Gaussian functions. For instance, in the so called dual process, one can distinguish between two surface textures even when one surface lies on top of the other. Nevertheless, there is no established method of HD data fitting in the case of ALD processes. The authors propose a data-fitting strategy based on the Levenberg –Marquardt least square algorithm using Gauss functions. It is a well known fact that ALD does not produce a complete layer after one cycle, due to steric hindrance [18]. Consequently, in the surface height histogram, two contributions are observable before the completion of the first layer; one is attributed to the substrate and the other to the deposited material. A dual process is relevant for the data study, because a layer of HfO_2 on a SiO_2 substrate is deposited, resulting in two distinguishable Gaussian peaks in the HD data.

3. Results and discussion

Figure 1 shows the surface topography, obtained by NC-AFM measurement, before the ALD process cycle (0) and after each subsequent ALD cycle (1–4). From the topography, RMS surface roughness was calculated, and surface height histograms were obtained (Fig. 2, left column).

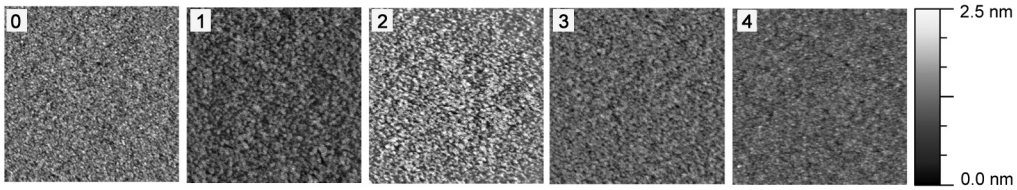

Fig. 1. Results of NC-AFM investigations in the first four ALD cycles performed with TDMAHf and H_2O as precursors. Each number corresponds to a completed ALD cycle. Cycle (0) depicts SiO_2 substrate before deposition. Image size: 400×400 nm

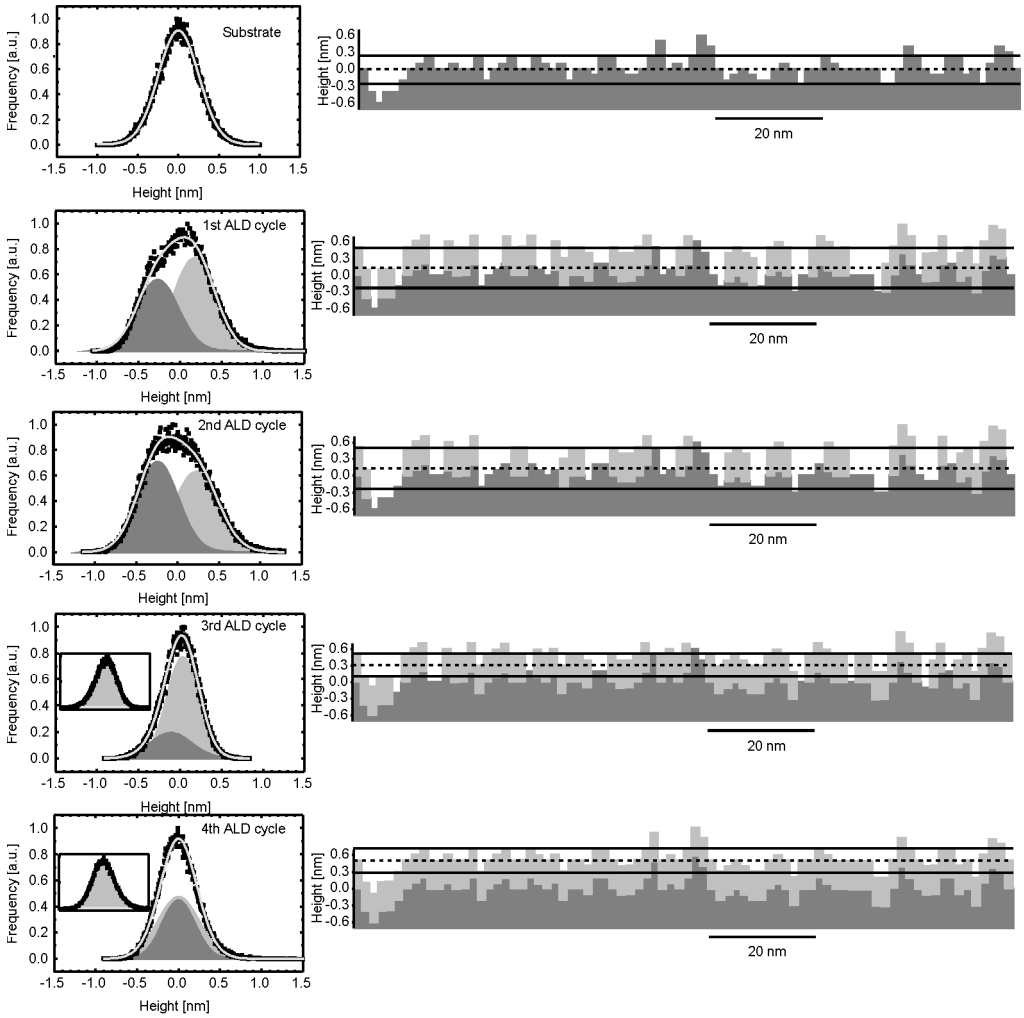

Fig. 2. Left column: surface height histograms calculated from topography images. For each ALD cycle the raw height data is leveled using the plane correction in order to set the arithmetic mean value μ of the image to zero. The curves are normalized to the same maximum level. Fit performed with a fixed width of the substrate peak taken from cycle 0. Dark grey peaks represent SiO_2 substrate, and light grey – deposited HfO_2. Right column: proposed model of the ALD growth. For each cycle HfO_2 coverage was calculated from the area ratio of the peaks present in the height histograms

In general, AFM measurement produces a model of the surface as a discrete two dimensional function $z(x,y)$ with $M \times N$ elements. However, in most cases, AFM images are square matrices with $M = N$ and 256×256 or 512×512 elements. For calculating the RMS surface roughness, we applied the equation

$$S_q = \left(\frac{1}{MN} \sum_{k=0}^{M-1} \sum_{l=0}^{N-1} \left(z(x_k, y_l) - \mu \right) \right)^{1/2} \tag{1}$$

where $z(x_k,y_l)$ is the height of the surface model at the point with coordinates k and l with μ being the arithmetic mean of the height of the surface model. We set the μ value of the surface to zero by applying the plane correction in the SPIP software. Equation (1) is identical with the definition of standard deviation, thus the S_q parameter can also be considered as the standard deviation of the surface height.

In principle, it is possible to calculate RMS surface roughness from the surface height histograms. For such calculations, we fit the surface height histogram with one Gaussian peak, and RMS surface roughness is then equal to the half of the width of the peak. We use the Gaussian function of the form:

$$h(x) = h_0 + \frac{A}{w\left(\frac{\pi}{2}\right)^{1/2}} \mathrm{e}^{\frac{-2(x-\mu)^2}{\mathrm{w}^2}} \tag{2}$$

where h_0 and A are the values of the baseline and peak area, respectively, w is the width of the peak, $\sigma = w/2$ is the standard deviation of the surface height. With the μ parameter set to zero, we can directly compare the surface height histograms, as in general the arithmetic mean is different for each ALD cycle and this causes the Gaussian peaks to shift. As all the surface histograms have Gaussian or near-Gaussian distributions, the RMS surface roughness S_q and the standard deviation σ of the surface height should be closely related, and this fact is evident in Table 1, as well as the associated data plot shown in Fig. 3. Throughout this paper the standard deviation of the surface height will be used as calculated from Eq. (1), as an RMS surface roughness parameter.

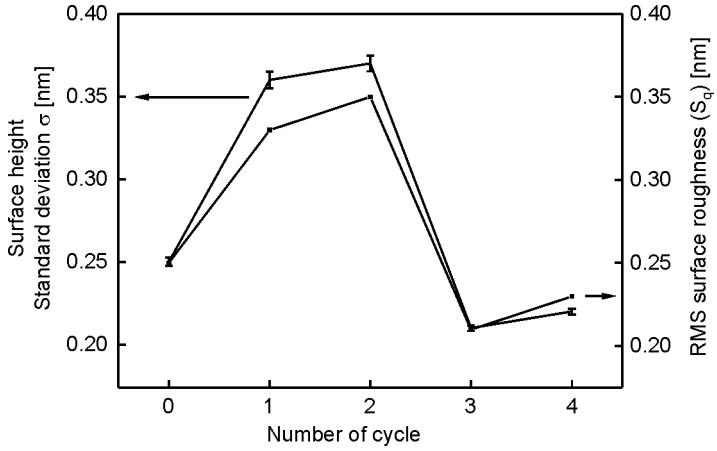

Fig. 3. Evolution of the RMS surface roughness during the ALD growth. The error bars for the plot of the standard deviation of the surface height σ are derived from the fit error of the Gaussian peak width

From the calculated data, we see that, after the first ALD cycle, S_q increases from 0.25 nm to about 0.33 nm and reaches a maximum value of 0.35 nm in the second

cycle. In the third and fourth cycle S_q equals 0.21 nm and 0.23 nm, respectively. As a result of HfO_2 deposition, starting from the third cycle, S_q decreases. After the fourth ALD cycle, S_q is close to the surface roughness observed before the start of the ALD process (cycle 0). The RMS surface roughness behaviour is in agreement with the ALD growth model developed by Nilsen et al. [16, 18]. The model predicts that at the beginning of the ALD process, the surface roughness initially increases, reaches a maximum value, and then subsequently decreases as a result of amorphous material deposition.

Table 1. Evolution of the RMS surface roughness during the ALD growth. For not perfectly Gaussian surface the S_q and σ parameters differ.

Cycle number	RMS surface roughness (S_q) [nm]	Surface height standard deviation (σ) [nm]	σ error [nm]
0	0.25	0.249	0.003
1	0.33	0.360	0.005
2	0.35	0.374	0.005
3	0.21	0.208	0.002
4	0.23	0.223	0.002

Surface height histograms (Fig. 2, left column) can be used to calculate how the HfO_2 coverage changes dynamically with the deposition cycle, i.e. during the ALD growth. Clear evolution of the surface height histograms from a single Gaussian (substrate) to a near-Gaussian, especially evident in the first and second cycle is observed. The height histogram turns again into a Gaussian, for the third and fourth ALD cycles, which was also confirmed by a single Gaussian fit (Fig. 2, left column insets). For the calculations of the surface coverage, the surface height histograms are fitted with two Gaussian peaks of the form stated in Eq. (2): the first Gaussian peak is attributed to the SiO_2 surface, whereas the second is attributed to the HfO_2 deposited material. In the data-fit, we used fixed width of the SiO_2 peak assuring that we deal with conformal, efficient ALD growth that is not modifying the RMS surface roughness of the substrate. However, we do see alerting of the substrate already form the fist ALD cycle as the SiO_2 Gaussian distribution is not perfectly fitted to the left tail of the surface height histogram. There are two explanations for this. Firstly, it is not possible to measure exactly the same area with an AFM tip after each ALD cycle and, secondly, the substrate surface is somehow modified during the ALD growth. Table 2 presents the relevant data describing the evolution of the HfO_2 coverage during the initial deposition cycles.

The presented results allowed us to construct a mathematical model of the HfO_2 growth in the early stages of the ALD process (Fig. 2, right column). The model shows only the SiO_2/HfO_2 interface profile. The profile roughness R_q is derived from the S_q parameter and, for the purpose of simplification, we assumed $R_q = S_q$. The initial roughness of the SiO_2 surface is connected with the Si roughness. Much research was

performed in the field of very thin SiO_2 layers and it is now established that the roughness of the SiO_2 is duplicating the roughness of the Si substrate [19, 20], although this may not necessarily be true for a native oxide [21].

Table 2. HfO_2 coverage calculations

Cycle number	SiO_2 peak area	HfO_2 peak area	SiO_2/HfO_2 ratio	HfO_2/SiO_2 ratio	HfO_2 coverage [%]
0	–	–	–	–	0
1	0.35	0.46	0.76	1.32	62
2	0.44	0.47	1.02	0.98	49
3	0.12	0.37	0.32	3.08	84
4	0.30	0.22	1.36	0.73	100

The mathematical model of the SiO_2 surface is based on real measurement data. The numerical values of the raw data for the cross-section were rounded off and recompiled to form a discrete grid of height values. The mesh spacing of the grid corresponded to a sampling distance of 0.1 nm. The entire substrate is represented as a discrete collection of 80 vertical columns lying in a grid. Based on the number of grids, the HfO_2/SiO_2 coverage ratio was estimated from the height histograms. In the calculations, we assumed that the area ratio equal to 1 reflects 50% of the surface coverage. Height of each element of HfO_2 grid was 0.5 nm as this value is in agreement with the literature [22–24].

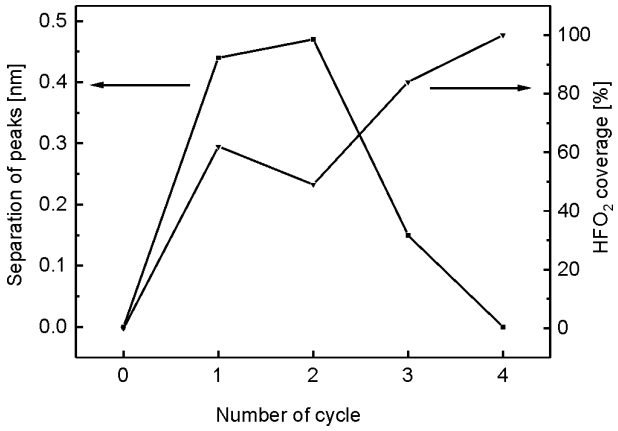

Fig. 4. Separationof peaks and HfO_2 coverage in the initial stages of the ALD growth. For the coverage around 50%, the separation of peaks reflects the height of the incomplete HfO_2 layer

With some assumptions, the peak separation presented in Fig. 4 can be interpreted in terms of an incomplete HfO_2 layer, having non-uniform thickness. Three different fitting procedures were used and up to the second cycle the peak separation equal to (0.46±0.02) nm was obtained (average value taken from 6 data fits) [25]. For the sur-

face coverage of approximately 50%, where the AFM tip refers to both the SiO_2 and HfO_2 surfaces in approximately equal amount, the peak separation faithfully reflects the true height of deposited HfO_2 material. For the HfO_2 surface coverage exceeding 84%, the SiO_2 surface no more can serve as a height reference. In that case, the AFM tip detects more HfO_2 surface, and due to observed conformal growth, the deposited high-*k* surface roughness duplicates the SiO_2 substrate roughness, thus as a result the mean peak separation is reduced. In consequence, after completion of the first HfO_2 layer, the separation of the peaks equals zero.

Black horizontal lines reflect the standard deviation of the surface height and may be directly connected to RMS surface roughness. The middle dashed line is the arithmetic mean value of the height data and shifts (approximation) to positive values of the height vs. ALD cycles.

The presented model is more accurate in terms of the height than in horizontal direction as the correlation length was not taken into account. In a rough estimation, the model reflects the behaviour of the surface skewness correctly. Due to the fixed substrate roughness, the obtained model is an approximation. From the height histogram data, clearly substrate changes vs. the ALD cycles can be seen. This is most evident in the second ALD cycle in which the HfO_2 coverage is smaller than in the first ALD cycle and the peak separation slightly increases. The first possible explanation for substrate modification might be the interfacial layer growth between the deposited HfO_2 and the SiO_2 substrate [26–29]. A small increase in peaks separation between the first and second cycle may indicate that underneath the deposited HfO_2 (and only there) the HfO_2/SiO_2 interface increases. However a very small difference equal to 0.03 nm, being at the limits of AFM sensitivity, cannot be reflected on the model picture. In another explanation we may state that, the SiO_2 substrate is so rearranged in the second cycle that the SiO_2 surface is larger. Third possibility may be connected with slightly different measurement positions between first and second ALD cycle. As the presented possibilities are hard to reflect in the model, the HfO_2 coverage was simply lowered in the model picture. In the third ALD cycle, the HfO_2 coverage reaches 84% and finally in the fourth cycle the layer is complete when the peak separation equals zero.

In the first four cycles, the ALD process follows substrate morphology, meaning that the starting SiO_2 surface influences HfO_2 growth in the initial phase of the deposition [30]. High quality surface fabricated by properly chosen etching procedures might be desirable when performing the ALD process [31].

As a general rule, AFM measurements suffer from the tip sample convolution effect, due to the tip shape and mainly to finite tip radius [32–34]. Most particularly, this effect strongly depends on the height and aspect ratio of the features present on the surface and the tip radius. Nevertheless, in the presented measurements, this effect is lowered due to the small surface roughness and low aspect ratio of the observed features.

4. Conclusions

We showed that the FM-AFM technique is sensitive to surface changes induced by the ALD process from the very beginning of the deposition. RMS surface roughness increases during the first two ALD cycles. From the third ALD cycle and onwards, the surface becomes smoother as a result of amorphous HfO_2 deposition. We have illustrated that the study of surface height histograms is very helpful to gain additional information about the ALD growth. By detailed analysis of the peaks appearing in the surface height histograms, it was possible to calculate the HfO_2 coverage in the early stages of the ALD process, and confirm that the first high-k layer was complete after four ALD cycles. The completion of the first HfO_2 layer after four ALD cycles was also confirmed by synchrotron radiation photoelectron spectroscopy (not shown). The surface coverage calculations were helpful for developing a simplified model of the HfO_2 growth in the initial phase of the ALD process. Forthcoming experiments with more ALD cycles will reveal additional details about HfO_2 the nanoscale dynamics of HfO_2 deposition on SiO_2/Si(001) substrate.

Acknowledgements

The authors acknowledge the assistance with experiments provided by Guido Beuckert and Konstantin Karavaev (Brandenburg University of Technology). This work was supported by the Bundesministerium für Bildung und Forschung (BMBF) and Deutsche Forschungsgemeinschaft (DFG) within priority program 1157.

References

[1] WILK G.D., WALLACE R.M., ANTHONY J.M., J. Appl. Phys., 89 (2001), 5243.
[2] GENG H., HWAIYU G., *Semiconductor Manufacturing Handbook*, Mcgraw-Hill Professional, 2005.
[3] LOCQUET J., MARCHIORI C., SOUSA M., FOMPEYRINE J., SEO J.W., J. Appl. Phys., 100 (2006), 051610.
[4] RITALA M., KUKLI K., RAHTU A., RÄISÄNEN P.I., LESKELÄ M., SAJAVAARA T., KEINONEN J., Science, 288 (2000), 319.
[5] PUURUNEN R.L., J. Appl. Phys., 97 (2005), 121301.
[6] ROBERTSON J., Rep. Prog. Phys., 69 (2006), 327.
[7] GREEN M.L., HO M., BUSCH B., WILK G.D., SORSCH T., CONARD T., BRIJS B., VANDERVORST W., RAISANEN P.I., MULLER D., BUDE M., GRAZUL J., J. Appl. Phys., 92 (2002), 7168.
[8] PUURUNEN R.L., VANDERVORST W., J. Appl. Phys., 96 (2004), 7686.
[9] PUURUNEN R.L., J. Appl. Phys., 95 (2004), 4777.
[10] TALLARIDA M., KARAVAEV K., SCHMEISSER D., J. Appl. Phys., 104 (2008), 064116.
[11] ALBRECHT T.R., GRUTTER P., HORNE D., RUGAR D., J. Appl. Phys., 69 (1991), 668.
[12] GIESSIBL F.J., HEMBACHER S., BIELEFELDT H., MANNHART J., Science, 289 (2000), 422.
[13] GARCÍA R., PÉREZ R., Surf. Sci. Rep., 47 (2002), 197.
[14] GIESSIBL F.J., Rev. Mod. Phys., 75 (2003), 949.
[15] PUURUNEN R., Chem. Vap. Deposition, 10 (2004), 159.
[16] NILSEN O., MOHN C.E., KJEKSHUS A., FJELLVAG H., J. Appl. Phys., 102 (2007), 024906.
[17] COGDELL J.D., Precis. Eng., 32 (2008), 34.
[18] ROBERTSON J., Eur. Phys. J. Appl. Phys., 28 (2004), 265.
[19] TSAI V., WANG X., WILLIAMS E.D., SCHNEIR J., DIXSON R., Appl. Phys. Lett., 71 (1997), 1495.

[20] GOTOH M., SUDOH K., ITOH H., KAWAMOTO K., IWASAKI H., Appl. Phys. Lett., 81 (2002), 430.
[21] MAEDA T., KUROKAWA A., SAKAMOTO K., ANDO A., ITOH H., ICHIMURA S., J. Vac. Sci. Technol. B, 19 (2001), 589.
[22] WANG J., LI H.P., STEVENS R., J. Mater. Sci., 27 (1992), 5397.
[23] YLILAMMI M., Thin Solid Films, 279 (1996), 124.
[24] ZHAO X., VANDERBILT D., Phys. Rev., B 65 (2002).
[25] KOLANEK K., TALLARIDA M., SCHMEISSER D., unpublished results.
[26] CALLEGARI A., CARTIER E., GRIBELYUK M., OKORN-SCHMIDT H.F., ZABEL T., J. Appl. Phys., 90 (2001), 6466.
[27] CHO M., ROH Y.S., WHANG C.N., JEONG K., NAHM S.W., KO D., LEE J.H., LEE N.I., FUJIHARA K., Appl. Phys. Lett., 81 (2002), 472.
[28] OSHIMA M., TOYODA S., OKUMURA T., OKABAYASHI J., KUMIGASHIRA H., ONO K., NIWA M., USUDA K., HIRASHITA N., Appl. Phys. Lett., 83 (2003), 2172.
[29] LU J., AARIK J., SUNDQVIST J., KUKLI K., HÍRSTA A., CARLSSON J., J. Cryst. Growth, 273 (2005), 510.
[30] KOLANEK K., TALLARIDA M., KARAVAEV K., SCHMEISSER D., Thin Solid Films, 518 (2010), 4688.
[31] KARAVAEV K., KOLANEK K., TALLARIDA M., SCHMEISSER D., ZSCHECH E., Adv. Eng. Mater., 11 (2009), 265.
[32] WESTRA K.L., THOMSON D.J., J. Vac. Sci. Technol. B, 13 (1995), 344.
[33] SEDIN D.L., ROWLEN K.L., Appl. Surf. Sci., 182 (2001), 40.
[34] CHEN Y., HUANG W., Meas. Sci. Technol., 15 (2004), 2005.

Received 4 April 2010

Materials Science-Poland, *Vol. 28*, *No. 3*, *2010*

Morphology and characterization of cockloft-like ZnO/morin hybrid

Y. LI*, Y.-L. ZOU

College of Science, Civil Aviation University of China, Tianjin, 300300 P.R. China

Morin modified multilayer ZnO with a cockloft-like morphology was fabricated in alcohol solution, using hydrothermally synthesized ZnO nanodisks and morin as the precursors. The samples were characterized by field emission scanning electron microscopy, X-ray diffractometry, Fourier transform infrared spectroscopy and fluorescence spectroscopy. The results show that the cockloft-like ZnO hybrid, having hexangular morphology with the diameter of 1.5–2 μm and the thickness of ca. 1 μm, is composed of a multilayer flatform stacked by numerous ZnO nanodisks in its middle and a meshlike muffle made up of countless morin nanoparticles with the diameter of ca. 40 nm. The UV emission of the as-fabricated product is obviously attenuated by morin nanoparticles assembling on the surface of the ZnO nanodisks.

Keywords: *zinc oxide; morin; modification; morphology; cockloft; disk*

1. Introduction

ZnO, a n-type II–VI compound semiconductor with a direct band gap energy of 3.37 eV at ambient temperature and strong exciton binding energyof 60 meV, has currently attracted intensive interest in optics, electronics, catalysis, etc. Many papers focused on the synthesis of various ZnO nanostructures with particular morphologies, such as nanowires [1, 2], nanobelts [3], nanorods [4], nanotubes [5–7] and nanodisks [8]. Furthermore, various elements and compounds were doped into ZnO structure to improve its properties, such as Pt [9], titanate [10], CdS [11] and PbS [12]. The fabrication and the toluene sensing properties of TiO_2-doped ZnO nanostructures have been reported. It was found that a TiO_2-doped ZnO sensor exhibits remarkably enhanced responsiveness to 100 ppm toluene [13]. A colloidal Fe-doped ZnO nanocrystal was synthesized and its distinct ferromagnetic resonance signal at room temperature was revealed [14]. On the other hand, organic dyes such as cationic azobenzene dye [15] and rhodamine [16] are increasingly used as dopants and modifiers of inorganic nanomaterials. Among all the organic dyes, morin is usually used as a useful

*Corresponding author, e-mail: Liyan01898@163.com

dopant or modifier, especially as a fluorescent reagent. The photoluminescence of porous anodized aluminum oxide impregnated with morin was investigated [17]. A SiO_2-morin nanocomposite was successfully synthesized and the reactivity of the nano SiO_2, in terms of selective binding and extraction of heavy metal ions was greatly improved by morin modification [18]. The interaction between morin and TiO_2 was investigated by analyzing the UV-vis absorption, UV-vis diffuse reflectance spectrum [19]. Morin was also intercalated into NaY zeolite, as a modified electrode material [20]. The synthesis and the photocatalytic property of the dye-sensitized ZnO have been reported [21]. ZrO_2/morin nanocomposite was fabricated by a simple heat refluxing method and the enhancement of its photoluminescence was disclosed [22]. To our knowledge, there have been no reports on morin modified ZnO. Therefore, it is necessary to research the fabrication and characterization of morin modified ZnO structure. In this paper, we report a cockloft-like structure of morin modified multilayer ZnO, and its properties are characterized via X-ray diffractometry, field emitting scanning electron microscopy, Fourier transform infrared spectrometry and fluorescence spectrometry.

2. Experimental

Materials. All reagents such as zinc chloride ($ZnCl_2$, 98%), ammonia ($NH_3 \cdot H_2O$, 25%), and N,N,N-trimethyl-1-hexadecanaminium bromide (CTABr, $C_{19}H_{42}BrN$, 99%), morin hydrate ($C_{15}H_{10}O_7 \cdot xH_2O$, 99.5%) and absolute ethanol (C_2H_5OH, 99.7%), purchased from Kewei Company of Tianjin University, were analytical grade, and were used without further purification.

Fabrication. The fabrication of morin decorated ZnO disks was carried out according to the following procedure. In the first step, 6 g of $ZnCl_2$ and 0.05 g of CTABr were dissolved into 90 cm^3 of distilled water, and then 6.5 cm^3 of ammonia was slowly dropped into the former solution under vigorous stirring to form the reactant mixture. Subsequently, the solution was loaded in a 250 cm^3 beaker placed in a water bath and was hydrothermally treated, first at 95 °C for 3 h and then at 50 °C for 1 h. The resulting white precipitate was washed several times with distilled water and alcohol, and dried at 60 °C for 10 h in an oven to obtain ZnO products. In the second step, the as-synthesized ZnO particle was mixed with 10 cm^3 of morin solution, using alcohol as a solvent, and the mixture was thoroughly mixed until it was dried by natural evaporation in atmosphere to obtain the products.

Characterization. The morphologies of the as-synthesized samples were investigated by 1530VP model field emission scanning electron microscopy (FESEM). The X-ray diffraction (XRD) pattern of the obtained particles was identified on a DX-2000 X-ray diffractometer with CuK_α radiation (λ = 0.1542 nm). Photoluminescence (PL) spectra of these samples were measured with a WGY-10 fluorescence spectrophotometer with a Xe lamp (150 mW). The excitation wavelength was fixed at 230 nm.

The spectrum of these samples at ambient temperature was observed in the wavelength range of 350–600 nm. Fourier transform infrared spectroscopy (FTIR) measurements of the samples were undertaken on a Nicolet 380 spectrometer with the spectral resolution of 1 cm^{-1}. The samples were mixed with KBr, in the weight ratio of sample-to-KBr of 1:100, and were then pressed into pellets for characterization.

3. Results and discussion

FESEM images and XRD spectra. Figure1 shows the images of the as-prepared ZnO disks and the mesh-like morin masked multilayer ZnO. In Figure 1a, a very large number of nanodisks 1.5 μm in diameter and ca. 50–100 nm thick can be observed, which can be easily indexed to a wurtzite ZnO structure (Fig. 2a) and has an unclear hexagon shape.

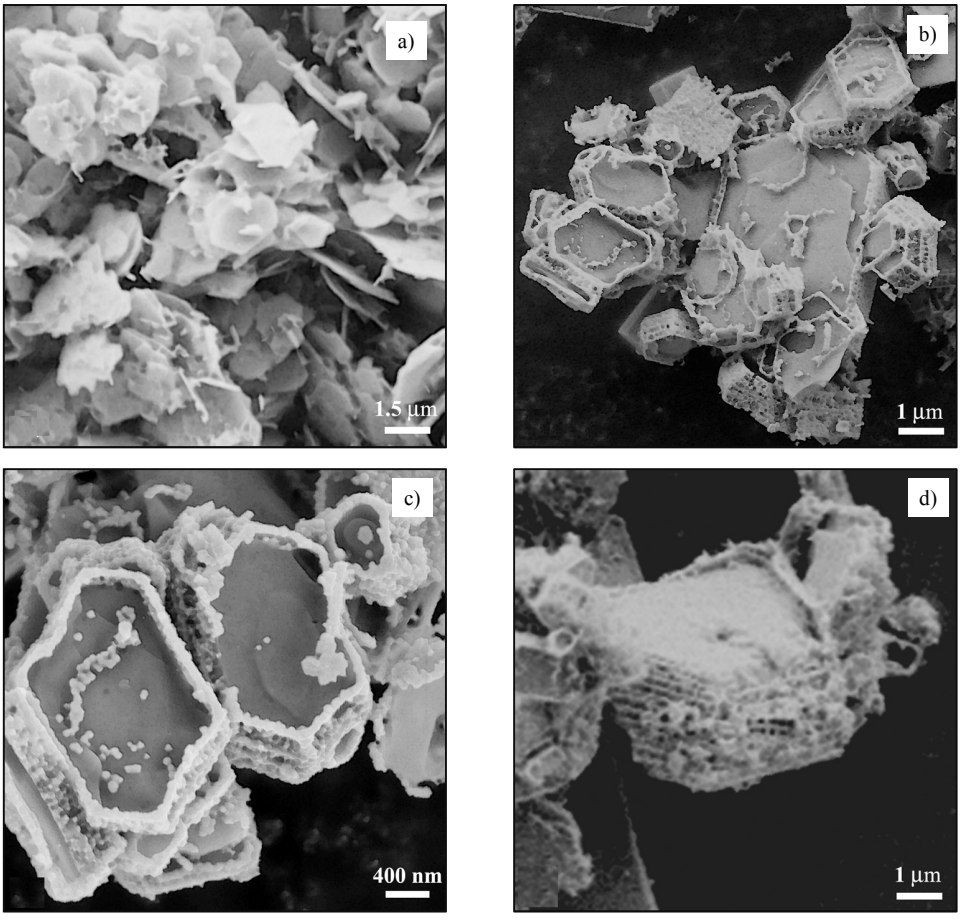

Fig. 1. FESEM images of the fabricated ZnO nanodisks (a) and the cockloft-like ZnO -- formed in morin solution with a concentration of 0.005 mol/dm^3 (b, c, and d)

Here, the synthesis of the as-prepared product was carried out hydrothermally at a relatively low temperature (95 °C) and under magnetic stirring, using zinc chloride and ammonia as the starting materials. But it was reported that the morphologies of ZnO synthesized materials produced under the same conditions usually appear as rods, tubes and particles etc., not disk like shapes. Compared with other synthesis conditions of nano ZnO, the main difference is that continuous stirring was undertaken during the hydrothermal synthesis in this paper. This implies that the dynamic growth mechanism is possibly changed by stirring. In Figure 1b, a particular structure can be clearly observed, which looks like some very regular cockloft type structure. This special structure has hexagular morphology with the diameter of 1.5–2 μm and the thickness of about 1 μm. Further details can be observed in Figure 1c, the cockloft is composed of two components: the middle part of the cockloft is a multilayer flatform made up of ZnO nanodisks and a meshlike muffle composed of morin nano particles with the diameter of about 40 nm. In every single layer of this structure, numerous morin nanoparticles, adsorbing to the fringes of the hexangular ZnO disks, quite orderly form a necklace around the multilayer ZnO flatform. Observing the profile of the outboard surface of the cockloft in Fig. 1d, there are numerous morin particles self-assembled into a nanomesh with pores of ca. 40–100 nm in diameter in a good order.

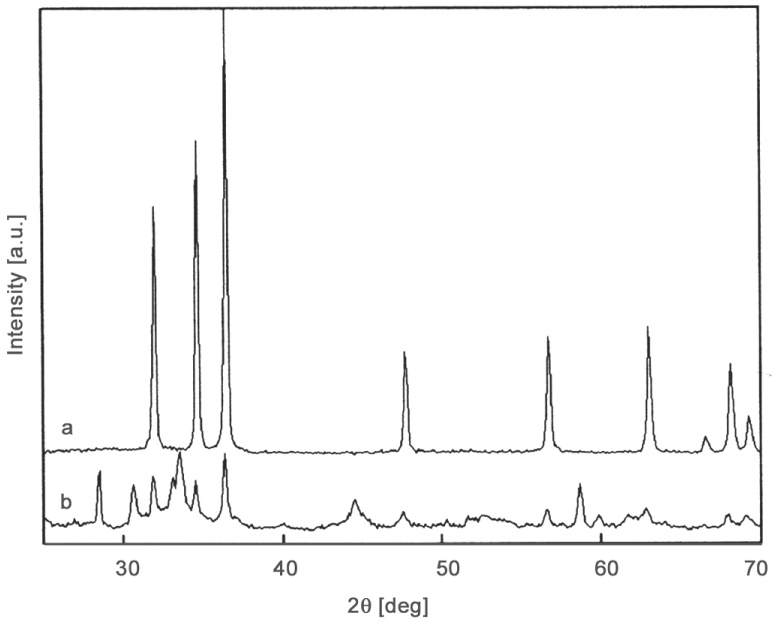

Fig. 2. XRD spectra of the fabricated ZnO nanodisks (a) and the cockloft-like ZnO formed in morin solution with a concentration of 0.005 mol/dm^3 (b)

The outstanding change of the XRD patterns of the prepared samples can be caused by the self-assembled structure of morin particle to multilayer ZnO. Except

XRD peaks at 31.84°, 34.81° and 36.33°, all XRD diffraction peaks of the multilayer ZnO in Fig. 2, spectrum a almost disappear and several peaks related to morin appear in spectrum b, due to the dispersion and the absorption of X-ray by morin particles. The XRD measurement results reflect the morphology of the ZnO multilayer masked by morin mesh in a visible manner.

Based on the results above, the assembly mechanism of morin-modified ZnO can be proposed as follows. ZnO nanodisks come out under stirring in hydrothermal system during the first step of the synthesis. In the second step, morin nanoparticles crystallized from the alcohol solution preferentially adsorb on the fringe of these nanodisks to form a laciness round ZnO nanodisks. Then, the nanodisks stack together along plane (0001) by the dipolar force of ZnO, and meanwhile morin nanoparticles belonging to the neighbouring laciness combine with each other to form a meshlike muffle. In this way, the cockloft-like ZnO/morin composite structure is achieved.

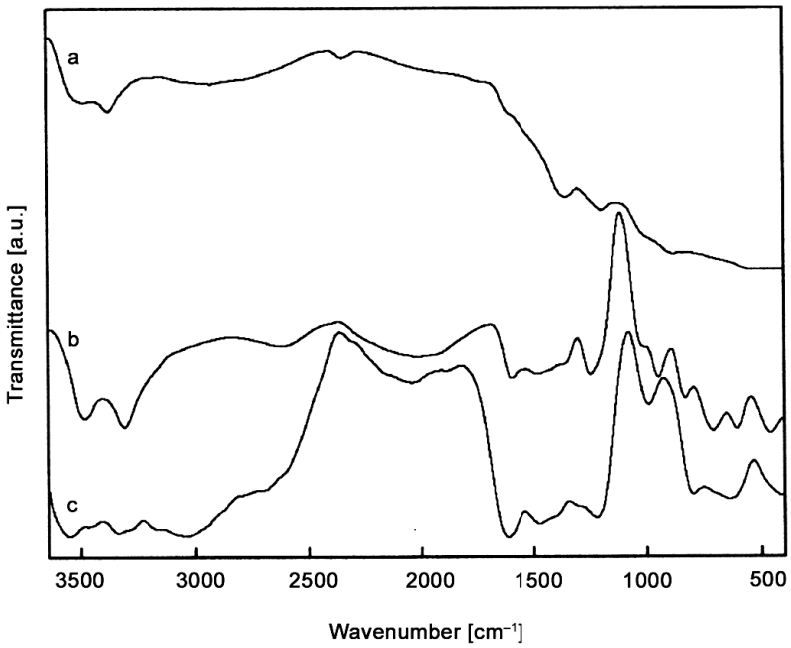

Fig. 3. FTIR transmittance spectra of the fabricated ZnO nanodisks (a), the cockloft-like ZnO formed in morin solution with a concentration of 0.005 mol/dm^3 (b) and pure morin (c)

FTIR spectra. Figure 3 shows the FTIR spectra of ZnO disks (spectrum a), morin-modified ZnO (spectrum b) and morin (spectrum c). In spectrum a, the absorption peaks of ZnO nanodisks located at 560 and 902 cm^{-1} can be attributed to the bend vibration and the stretching vibration of Zn–O, respectively. The peaks at 1196 cm^{-1} and 1340 cm^{-1} are assigned to the C–O bond of CTABr remains. The peaks at 1613 cm^{-1} and 2359 cm^{-1} are assigned to OH^- and CO_3^{2-}. The peaks at 1620, 1460 and 1216 cm^{-1} in the spectra of morin (Fig. 3, curve c) can be assigned to the C=C vibration in benzene rings and

asymmetric stretching vibration of C–O–C, respectively. The bands between 993 and 630 cm^{-1} are assigned to the stretching vibration of –C–OH [19]. Comparing the IR spectrum of ZnO nanodisks and morin with that of the as-fabricated morin modified ZnO, the bands at 993, 797 and 630 cm^{-1} disappeared with the appearance of new bonds at 951, 832, 714, 609 and 463 cm^{-1}. Weak bands at 902 and 560 cm^{-1} corresponding to Zn–O were concealed by strong ones. It implies that some new chemical bonds were formed between ZnO disks and morin particles.

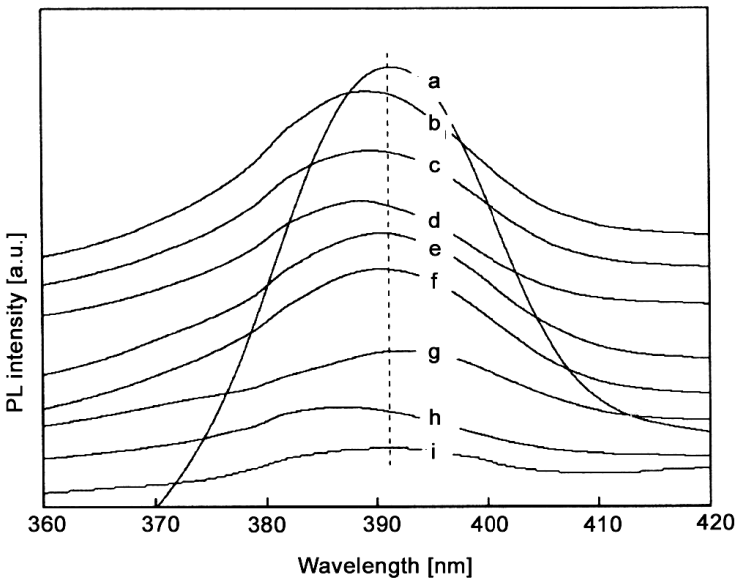

Fig. 4. Room temperature PL spectra of the fabricated ZnO nanodisks (a), the cockloft-like ZnO formed in morin solution using alcohol as the solvent with the concentration of: b) 0.003 mol/dm^3, c) 0.005 mol/dm^3, d) 0.007 mol/dm^3, e) 0.009 mol/dm^3, f) 0.011 mol/dm^3, g) 0.013 mol/dm^3, h) 0.015 mol/dm^3 and i) 0.017 mol/dm^3

PL spectra. Figure 4 shows the room temperature PL spectra of ZnO nanodisks and morin modified ZnO nanodisks. It is clearly observed that the intensity of the UV emission at about 396 nm [23, 24] evidently decreases as the dosage of morin increases in the fabrication process of the morin modified ZnO nanodisks. In general, the intensity of the UV emission of the reported morin doped inorganic oxide is usually strongly enhanced by introducing an appropriate dosage of morin into oxide [19]. Here, the attenuation of the UV emission is caused by absorption of the exciting light by morin and the emittion from nano ZnO. The fact is that ZnO particles are muffled by numerous morin particles, which reduces the intensity of the excitation light arriving at the surface of ZnO and the emission emitted from the ZnO surface. The radical of morin does not integrate into ZnO structure and does not change the energy band structure, and therefore the emission mechanism of ZnO nanodisks cannot be changed.

4. Conclusion

A well ordered structure of morin modified multilayer ZnO with a cockloft-like morphology can be successfully fabricated via a simple adsorption process in alcohol solution, using ZnO nanodisks synthesized in a hydrothermal system and morin as the precursor. The cockloft-like ZnO composite, having a wurtzite structure and a hexangular morphology with the diameter of 1.5–2 μm and the thickness of about 1 μm, is composed of two parts: a multilayer flatform stacked by numerous ZnO nanodisks in its middle and a meshlike muffle made up of a very large number of morin nanoparticles with diameters of ca. 40 nm. Comparing the IR spectrum of the ZnO nanodisks and morin with that of the as-fabricated cockloft type composite, it can be observed that the bands at 993, 797 and 630 cm^{-1} disappear with the occurrence of the new bands at 951, 832, 714, 609 and 463 cm^{-1}, which implies that some new chemical bonds are formed between ZnO disks and morin particles. The UV emission of the as-fabricated product is obviously attenuated by morin nanoparticles assembling on the surface of ZnO nanodisks.

Acknowledgements

This work was supported by the National Natural Science Foundation of China (Grant No. 51002183), and jointly supported by the National Natural Science Foundation of China and the Civil Aviation Administration of China (Grant No. 61079010).

References

[1] AHSANULHAQ Q., KIM S.H., HAHN Y.B., J. Phys. Chem. Solids, 70 (2009), 627.
[2] GAO H., ZHOU M.Y., JI H., WANG X.Z., ZHANG Z.G., J. Alloy Compd., 464 (2008), 234.
[3] LIN C.F., LIN H., ZHUANG D.T., LI J.B., J. Nanosci. Nanotechn., 9 (2009), 1976.
[4] ZHU H.L., YANG D.R., ZHANG H., Inorg. Mater., 42 (2006), 1210.
[5] LIU J.P., HUANG X.T., J. Solid State Chem., 179 (2006), 843.
[6] LI Y., FENG H., ZHANG N., LIU C., Mater. Sci.-Poland, 27 (2009), 551.
[7] LI Y., LIU C., ZOU Y., Chem. Pap., 63 (2009), 698.
[8] GAO P., YING C., WANG S.Q., YE L.N., GUO Q.X., XIE Y., J. Nanopart. Res., 8 (2006), 131.
[9] DJINOVIC V.M., MANCIC L.T., BOGDANOVIC G.A., VULIC P.J., ROSARIO G., SABO T.J., MILOSEVIC O.B., J. Mater. Res., 20 (2005), 102.
[10] LIU G., LI G.S., QIU X.Q., LI L.P., J. Alloy Compd., 481 (2009), 492.
[11] LUO Y.L., Colloid J., 71 (2009), 370.
[12] NTWAEABORWA O.M., KROON R.E., KUMAR V., DUBROCA T., AHN J.P., PARK J.K., SWART H.C., J. Phys. Chem. Solids, 70 (2009), 1438.
[13] ZENG Y., ZHANG T., WANG L.J., KANG M.H., FAN H.T., WANG R., HE Y., Sensor Actuat B. Chem., 140 (2009), 73.
[14] SINGHAL A., ACHARY S.N., TYAGI A.K., MANNA P.K., YUSUF S.M., Mater. Sci. Eng. B. Adv. Funct. Solid State Mater., 153 (2008), 47.
[15] WAN T., XU H., YUAN Y., HE W., J. Wuhan Univ., Tech.-Mater. Sci. Ed., 22 (2007), 466.
[16] COSTELA A., GARCÍA-MORENO I., GÓMEZ C., GARCÍA O., SASTRE R., Appl. Phys. B., Lasers Opt., 75 (2002), 827.

[17] SHEN Y., JIA R.P., LUO H.Q., CHEN X.G., XUE D.S., HU Z.D., Spectrochim Acta. A. Mol. Biomol. Spectr., 60 (2004), 1007.
[18] ZOU X.J., CUI Y.M., ZHU X.B., HU Z., CHANG X.J., J. Sol-Gel Sci. Techn., 50 (2009), 35.
[19] ZHOU Q.H., ZHANG H.M., WANG Y.Q., ZHOU X.D., Spectrochim Acta. A, 72 (2009), 110.
[20] ZENDEHDEL M., BABAEI A., ALAMI S., J. Incl. Phenom Macr., 59 (2007), 345.
[21] YANG G., CHAN S., J. Nanopart. Res., 11 (2009), 221.
[22] LIU X.L., LI Y., WANG X.Y., Mater. Lett., 60 (2006), 1943.
[23] WANG L.J., GILES N.C., J. Appl. Phys., 94 (2003), 973.
[24] WANG H.Q., WANG G.Z., JIA L.C., TANG C.J., LI G.H., J. Phys. D.Appl. Phys., 40 (2007), 6549.

Received 12 February 2010

Materials Science-Poland, *Vol. 28*, *No. 3*, *2010*

Coordination properties of diethyl (pyridyn-2-ylmethyl)phoshate ligand with chloride transition metal salts

B. ŻUROWSKA[1*], U. KALINOWSKA-LIS[2], J. OCHOCKI[2]

[1]Faculty of Chemistry, University of Wroclaw, 14 F. Joliot- Curie St., 50-383 Wroclaw, Poland

[2]Department of Bioinorganic Chemistry, Faculty of Pharmacy, Muszyńskiego 1, Medical University, 90-151 Łódź, Poland

A new series of chloride transition metal complexes containing a diethyl (pyridyn-2-ylmethyl) phosphate (2-pmOpe) ligand, of the general formula $[M(2\text{-pmOpe})_2Cl_2]$ (M = Cu, Ni, Mn) and $[M(2\text{-pmOpe})Cl_2]$ (M = Co, Zn), were synthesized and studied. The stoichiometry and stereochemistry of the compounds were confirmed by elemental analysis, spectroscopic and magnetic studies. The ligand containing two donor atoms, heterocyclic pyridyl nitrogen and phosphoryl oxygen atoms, binds in a didentate chelate manner in all complexes. The octahedral (Cu, Ni, Mn) and tetrahedral (Co, Zn) coordination sphere complete chloride ions included in coordination. The magnetic behaviour (for paramagnetic centres) and spectroscopic analyses of the complexes indicate a mononuclear structure and suggest existence of a very weak exchange coupling between the metal centres in the crystal lattice.

Keywords: *transition metal complexes; N,O-donor ligand; spectroscopy; magnetism*

1. Introduction

The title compounds have been synthesized and investigated as a part of the program of research regarding metal complexes of the N-heterocyclic phosphonate and phosphate ligands. Recently, much attention has been focused on the synthesis of phosphonate and phosphate diesters, derivatives of pyridine or quinoline and their platinum(II) and palladium(II) complexes, because of their potential [1] and significant [2–14] anti-tumour activity. In previous studies, the authors have demonstrated high reactivity of pyridyl- and quinolyl-substituted phosphate diesters to transition metal ions [15–26]. However, the interaction of the new class of organophosphorous compounds, i.e. phosphate esters, derivatives of pyridine, with transition metal ions is

[*]Corresponding author, e-mail: zurowska@wchuwr.pl

still little known. Studies on the structure and biological activity of platinum(II) and palladium(II) complexes with diethyl (pyridin-2,-3- and -4-ylmethyl)phosphate (2-pmOpe, 3-pmOpe and 4-pmOpe, respectively) have been published [1, 14]. Recently, we reported the coordination properties of 2- and 4-pmOpe ligand with perchlorate metal(II) salts [25, 26] and chloride zinc(II) [27]. Further investigation of the reactivity of the N-heterocyclic phosphate ligands to transition metal salts concern the interaction of 2-pmOpe ligand (Fig. 1) with chloride transition metal salts.

In this paper, interactions of chloride metal(II) salts with 2-pmOpe ligand have been analysed, and stoichiometries as well as geometrical arrangements of the resulting species have been proposed. Physicochemical properties of the compounds and their possible structures were discussed based on their spectral properties (infrared, ligand field spectra) and magnetism analyses.

2. Experimental

Reagents and physical measurements. The starting materials and solvents for the syntheses obtained commercially were used as received. The compositions of the metals were determined using a Carl Zeiss Jena atomic absorption spectrophotometer and an ARL Model 3410 ICP spectrometer. Elemental analyses were carried out using a Perkin-Elmer elemental analyzer 2400CHN. Solid state electronic spectra (28 000 –4000 cm^{-1}) were obtained on a Cary 500 spectrophotometer. Magnetic measurements were carried out with a Quantum Design SQUID magnetometer (MPMSXL-5 type). The measurements were recorded at the magnetic field strength of 0.5 T in the temperature range 1.8–300 K. Corrections for diamagnetic contributions were based on subtracting the sample holder signal and estimating the contribution χ_D from the Pascal constants [26]. The effective magnetic moments were calculated from $\mu_{eff} = 2.83(\chi_M T)^{1/2}$ using temperature independent paramagnetism of 60×10^{-6} $cm^3\cdot mol^{-1}$ for Cu(II) ions, of 500 type 10^{-6} $cm^3\cdot mol^{-1}$ for Co(II) ions and of 220×10^{-6} $cm^3\cdot mol^{-1}$ for Ni(II) ions [29].

Synthesis of 2-pmOpe ligand. The diethyl (pyridyn-2-ylmethyl)phosphate (2-pmOpe) (Fig. 1) ligand was prepared according to the procedure described elsewhere [1].

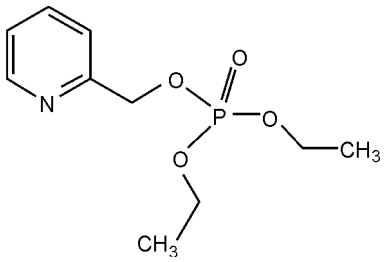

Fig. 1. Formula of the 2-pmOpe ligand

Syntheses of 2-pmOpe complexes. The chloride complexes were synthesized by dissolving an appropriate hydrated metal chloride (1 mmol) in ethanol (10 cm^3) and adding to a solution of the ligand (1 or 2 mmol) in ethanol (20 cm^3). The resulting solutions were filtered and left to evaporate slowly at room temperature. Attempts to obtain monocrystals so suitable for X-ray identification were unsuccessful.

Anal. Calc. for $C_{20}H_{32}Cl_2CuN_2O_8P_2$ (**1**): C, 38.44; H, 5.17; N, 4.48; Cu, 10.17. Found: C, 37.85; H, 5.62; N, 4.44; Cu, 10.31 %.

Anal. Calc. for $C_{20}H_{32}Cl_2NiN_2O_8P_2$ (**2**): C, 38.74; H, 5.21; N, 4.52; Ni, 9.46. Found: C, 38.55; H, 5.82; N, 4.34; Ni, 9.13 %.

Anal. Calc. for $C_{10}H_{16}Cl_2CoNO_4P$ (**3**): C, 32.05; H, 4.31; N, 3.73; Co, 15.71. Found: C, 32.48; H, 4.33; N, 3.42; Co, 15.23 %.

Anal. Calc. for $C_{10}H_{16}Cl_2ZnNO_4P$ (**4**): C, 31.48; H, 4.23; N, 3.67; Zn, 17.41. Found: C, 31.78; H, 4.33; N, 3.42; Co, 17.23 %.

Anal. Calc. for $C_{20}H_{32}Cl_2MnN_2O_8P_2$ (**5**): C, 38.97; H, 5.24; N, 4.55; Mn, 8.91. Found: C, 38.55; H, 5.32; N, 4.34; Mn, 9.13 %.

3. Results and discussion

A series of M(II) (M = Cu, Ni, Co, Mn and Zn) chloride complexes with diethyl (pyridin-2-ylmethyl)phosphate ester (2-pmOpe) have been synthesized. The stoichiometry of the complexes was identified from the elemental analysis and metal determination data. Results of analyses showed that the 2-pmOpe ligand is able to form coordination compounds with M(II) chloride salts in a 2:1 or 1:1 molar ratio, resulting in the following stoichiometries: $[M(2\text{-pmOpe})_2Cl_2]$ (M = Cu, Ni, Mn) and $[M(2\text{-pmOpe})Cl_2]$ (M = Co and Zn). All the studied compounds are stable in solution when exposed to air.

3.1. Spectroscopic properties

In the IR spectra of the complexes under study, the absorption bands were assigned to C=C and C=N stretching modes of a pyridine molecule, and were observed in the 1600–1500 cm^{-1} range for a free ligand. These absorption bands are not shifted appreciably, whereas characteristic bands corresponding to out-of-plane and in-plane ring deformation of the 2-substituted pyridine ring (observed at ca. 400 and 600 cm^{-1}, in a free ligand, respectively) are shifted to higher frequencies by ca. 20 cm^{-1} and 13 cm^{-1}, respectively. This suggests coordination of the pyridyl nitrogen donor atom [30, 31].

A strong absorption band at 1270 cm^{-1} which corresponds to P=O stretching vibrations of a free ligand, in the spectra of all complexes is shifted by ca. 40 cm^{-1} towards lower frequencies, indicating coordination of the phosphoryl oxygen to the metal ions.

The far-IR frequencies of the ν(M–Cl) stretching vibrations corresponding to copper, nickel and manganese compounds are observed at 316, 236 and 317 cm^{-1}, respec-

tively. The ν(M–Cl) symmetric and asymmetric vibrations in [Zn(2-pmOpe)Cl_2] (302, 329 cm^{-1}) and [Co(2-pmOpe)Cl_2] (310, 324 cm^{-1}) are consistent with a pseudotetrahedral environment [32]. It is worth emphasizing that the IR spectrum of Zn(II) complex presented here exhibits significant differences in line shapes, relative intensities and position of the bands, compared with the spectrum of the complex obtained earlier, namely [Zn(2-pmOpe)Cl_2]$_2$ [27], in which the ligand acts as an N,O-bridge, indicating some differences in ligand conformation.

In the ligand field spectrum of the Cu(II) compound, only one band is seen at 13 870 cm^{-1}. It is associated with the $^2E_g \rightarrow {}^2T_{2g}$ transition in O_h symmetry, which indicates that the coordination sphere $N_2O_2Cl_2$ produces a weak ligand field [32, 33]. The position, as well as the shape, of this band suggests that CuN_2O_4 chromophore has a tetragonally elongated octahedral geometry.

The ligand field spectrum of the Ni(II) compound displays bands (at 24 450, 14 840, 8290 cm^{-1}) corresponding to the $^3A_{2g} \rightarrow {}^3T_{1g}(P)$, $^3A_{2g} \rightarrow {}^3T_{1g}(F)$ and $^3A_{2g} \rightarrow {}^3T_{2g}$ transitions. Asymmetric bands in the near-IR region show that the Ni(II) ion is in an N_2O_4 octahedral tetragonally distorted [34, 35]. The calculated [34] spectrochemical parameters D_q and B for Ni(II) are 830 and 960 cm^{-1}, respectively. A rather high value of B may suggest a distorted octahedral geometry arising from the different nature of organic and chlorido ligands. The 10Dq value shows that the nearest coordination sphere $N_2O_2Cl_2$ produces a weak ligand field [33].

The ligand field spectrum of a blue cobalt(II) compound is typical of compounds having pseudotetrahedral geometry [36]. The compound shows triply split bands, one in the visible region and the other in the near infrared, with the centre at 16 300 cm^{-1} and about 4000 cm^{-1}. The parameters D_q (370 cm^{-1}) and B (745 cm^{-1}), calculated using the secular equation for tetrahedral cobalt(II) the transition energies [36, 37], are based on the centres of gravity of the respective multiplets. These values are consistent with those reported for tetrahedral Co(II) complexes and are typical of ligands which differ significantly in strength [38].

Extremely low values of the intensities of the bands for the octahedral manganese(II) complex are not unusual [34]. The spectrum shows bands as shoulders on a high-energy ligand or CT band at ca. 25 000 cm^{-1} and ca. 19 000 cm^{-1}, which can be assigned to $^6A_{1g} \rightarrow {}^4A_{1g}$, ^4E_g and $^6A_{1g} \rightarrow {}^4T_{1g}(G)$ transitions, respectively. Other characteristic bands of d-d transitions are masked by UV absorption and are difficult to recognize in the complex, and thus the ligand field parameters cannot be calculated.

3.2. Magnetic properties

The EPR spectrum of Cu(II) compound is of axial type, with g values of $g_{\|} = 2.28_7$, $g_{\perp} = 2.06_4$ normal for copper in a octahedral environment. A high value for $g_{\|}$ suggests a planar geometry with relatively strong axial bonding. The spectrum is independent of the temperature. The EPR spectrum of the octahedral Co(II) compound shows no lines at room temperature, but one broad line at 77 K with g = 5.62. The

nickel(II) compound does not exhibit an X-band spectrum. The EPR spectrum of the manganese(II) displays a hyperfine structure that is typical of ^{55}Mn(II).

Effective magnetic moments of copper(II), nickel(II) and manganese(II) complexes at room temperature (1.92, 3.12, 6.02 μ_B, respectively) are within the usually observed ranges of experimental values for Cu(II), and high-spin Ni(II) and Mn(II) complexes in octahedral configuration [39], and are characteristic of uncoupled metal centres. The magnetic moment of [Co(2-pmOpe)Cl_2] (μ_{eff} = 4.37μ_B) is consistent with tetrahedral stereochemistries [39]. Variable temperature (77–300 K) magnetic susceptibility data were collected for all the studied paramagnetic complexes.

The negative values for the Weiss constants (θ), obtained from the equation $\chi_M = C/(T - \theta)$] were within the measured temperature range and were found to be –0.24, –0.63, –6.73, –0.12 K for Cu(II), Ni(II), Co(II) and Mn(II) complexes, respectively. They may suggest the possibility of a very weak magnetic interaction between magnetic centres at lower temperatures. Temperature dependences of magnetic susceptibilities $\chi_M T$ for all investigated complexes are shown in Fig. 2.

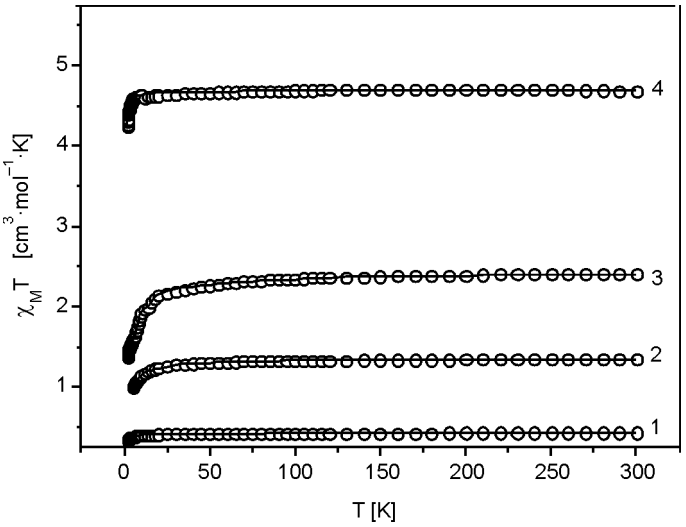

Fig. 2. Temperature dependences of $\chi_M T$ for [Cu(2-pmOpe)$_2$$Cl_2$] (**1**), [Ni(2-pmOpe)$_2$$Cl_2$] (**2**), [Co(2-pmOpe)$Cl_2$] (**3**) and [Mn(2-pmOpe)$_2$$Cl_2$] (**4**)

For all considered complexes, constant values of $\chi_M T$ are observed, decreasing only at the lowest temperatures (Fig. 2). This suggests the possibility of very weak magnetic interactions between magnetic centres inside crystal lattice at lower temperatures. The plot of $\chi_M T$ vs. T for cobalt(II) compound indicates a small contribution of the orbital moment, which is typical of the $^4A_{2g}$ ground state of Co(II) in a slightly distorted tetrahedral site [39].

Assuming all the complexes have monomeric structures**,** the data were analyzed using a molecular exchange field model based on the following equations[40]:

$$\chi_M = \frac{N\beta^2 g^2}{3kT} S(S+1) \tag{1}$$

$$\chi_M^{\text{corr}} = \frac{\chi_M}{1 - \frac{2zJ'}{N\beta^2 g^2}\chi_M} \tag{2}$$

where χ_M is the magnetic susceptibility of a paramagnetic centre, χ_M^{corr} is the measured experimental susceptibility, zJ' is exchange between magnetic ions belonging to different molecules, z is the number of nearest neighbours, and the other symbols have their usual meanings. In the context of this model, the parameter values obtained by least squares fitting are as follows: $zJ' = -0.35$, -0.28, -0.48 and -0.36 cm^{-1} for Cu(II), Ni(II), Co(II) and Mn(II), respectively. The results obtained for the compounds under investigations confirm their monomeric structures and indicate that a very weak antiferromagnetic exchange interaction occurs between magnetic centres in the crystal lattice.

4. Summary

The results described in the present paper have shown that the 2-pmOpe ligand with the Co(II), Ni(II) and Zn(II) chloride salts acts as an N,O-bonded chelate ligand through pyridyl nitrogen and phosphoryl oxygen atoms. Chloride complexes of Cu(II), Ni(II) and Mn(II) are six coordinated ($MN_2O_2Cl_2$ chromophore). The Zn(II) and Co(II) compounds are four coordinated ($MNOCl_2$ chromophore). The results presented here and earlier [27] suggest that in the reaction of $ZnCl_2$ with 2-pmOpe two polymorphic forms are formed. All the studied compounds are stable in solution exposed to air. The magnetism results (for paramagnetic centres) indicate the complexes have monomeric structures, and suggest the possibility of a very weak antiferromagnetic interaction between paramagnetic centres in the crystal lattice.

Acknowledgement

The work was supported by the by the Polish Ministry of Science and Higher Education, Grant No. N405 303236 (JO).

References

[1] KALINOWSKA U., CHĘCIŃSKA L., MAŁECKA M., ERXLEBEN A., LIPPERT B., OCHOCKI J., Inorg. Chim. Acta, 358 (2005), 2464.
[2] ARANOWSKA K., GRACZYK J., CHĘCIŃSKA L., PAKULSKA W., OCHOCKI J., Pharmazie, 61 (2006), 5.
[3] ZIĘBA R., MALINOWSKA K., WIEWIÓROWSKI M., GRACZYK J., Acta Pol. Pharm., 57 (2000), 136.
[4] CHĘCIŃSKA L., MAŁECKA M., OCHOCKI J., ARANOWSKA K., Acta Cryst., E59 (2003), m350.
[5] BRZEZIŃSKA-BŁASZCZYK E., MIŃCIKIEWICZ M., J. OCHOCKI J., Eur. J. Pharmacol., 298 (1996), 155.
[6] KOSTKA B., OCHOCKI J., Pharmazie, 51 (1996), 990.
[7] KAJMAN-BRONŻEWSKA L., OCHOCKI J., Pharmazie, 52 (1997), 198.

[8] ZHAO G., LIN H., YU P., SU H., ZHU S., SU X., CHEN Y., J. Inorg. Biochem., 73 (1999), 145.
[9] IAKOVIDOU Z., PAPAGEORGIOU A., DEMERTZIS M.A., MIOGLOU E., MOURELATOS D. KOTSL S.A., NATH YADA V.P., KOVALA-DEMERTZI D., Anti-Cancer Drugs, 12 (2001), 65.
[10] ĆURIĆ M., TUŠEK-BOŽIC L., VIKIĆ-TOPIĆ D., SCARCIA V., FURLANI A., BALZARINI J., DE CLERCQ E., J. Inorg. Biochem., 63 (1996), 125.
[11] TUŠEK-BOŽIĆ L., ĆURIĆ M., BALZARINI J.E., DE CLERCQ E., Nucleos, Nucleot., 14 (1995), 777.
[12] TUŠEK-BOŽIĆ L., MATIJAŠIĆ J., BOCELLI P., SGARBOTTO P., FURLANI V., SCARIA V., PAPAIOANNOU A., Inorg. Chim. Acta, 185 (1991), 229.
[13] TUŠEK-BOŽIĆ L.J., MATIJAŠIĆ J., BOCELLI G., CALESTANI G., FURLANI A., SCARCIA V.A., PAPAIOANNOU J., Chem. Soc., Dalton Trans,. 195 (1991).
[14] KALINOWSKA U., MATŁAWSKA K., CHĘCIŃSKA L., DOMAGAŁA M., KONTEK R., OSIECKA R., OCHOCKI J J., Inorg. Biochem., 99 (2005), 2024.
[15] ŻUROWSKA B., MROZIŃSKI J., CIUNIK Z., OCHOCKI J., J. Mol. Struct., 843 (2007), 26.
[16] ŻUROWSKA B., MROZIŃSKI J., OCHOCKI J., Mater. Sci., 25 (2007), 4.
[17] OCHOCKI J., ŻUROWSKA B., MROZIŃSKI J., REEDIJK J., Proc. III Symp. Inorganic Biochemistry and Molecular Biophysics, VI Int. Scientific School on Biological Macromolecules, Wrocław–Karpacz, Poland, 1991, p. 212.
[18] ŻUROWSKA B., MROZIŃSKI J., CIUNIK Z., OCHOCKI J., J. Mol. Struct., 79 (2006), 98.
[19] OCHOCKI J., KOSTKA K., ŻUROWSKA B., MROZIŃSKI J., GAŁDECKA E., GAŁDECKI Z., REEDIJK J., J. Chem. Soc. Dalton Trans., (1992), 2955.
[20] OCHOCKI J., ŻUROWSKA B., MROZIŃSKI J., KOOIJMAN H., SPEK A.L., REEDIJK J., Eur. J., Inorg. Chem., (1998), 169.
[21] ŻUROWSKA B., OCHOCKI J., MROZIŃSKI J., CIUNIK Z., REEDIJK J., Inorg. Chim. Acta, 357 (2004), 755.
[22] ŻUROWSKA B., BIAŁOŃSKA A., OCHOCKI J., Mater. Sci.-Poland, 27 (2009), 987.
[23] ŻUROWSKA B., KOTYŃSKI A., OCHOCKI J., Mater. Sci.-Poland, 27 (2009), 999.
[24] ŻUROWSKA B., ŚLEPOKURA K., LIS T., OCHOCKI J., Inorg. Chim. Acta, 2 (2009), 733.
[25] ŻUROWSKA B., KALINOWSKA-LIS U., BIAŁOŃSKA A., OCHOCKI J., J. Mol. Struct., 889 (2008), 98.
[26] ŻUROWSKA B., KALINOWSKA-LIS U., BRZUSZKIEWICZ A., OCHOCKI J., Inorg. Chim. Acta, 362 (2009), 1435.
[27] ŻUROWSKA B., KALINOWSKA-LIS U., OCHOCKI J., J. Coord. Chem.,63 (2010), 3764.
[28] KÖNIG E., *Magnetic Properties of Coordination and Organometallic Transition Metal Compounds*, Springer, Berlin, 1966.
[29] CARLIN R.L., *Magnetochemistry*, Springer, Heidelberg, 1986.
[30] WITTEVEEN H.T., REEDIJK J., J. Solid State Chem., 10 (1974), 151.
[31] CLARK R.J.H., WILIAMS C.S.W., Inorg. Chem., 4 (1965), 350.
[32] NAKAMOTO K., [In:] *Infrared and Raman Spectra of Inorganic and Coordination Compounds*, Wiley, New York, 1986, p. 191.
[33] WEST D.X., HARTLEY R.J., J. Inorg. Nucl. Chem., 42 (1980), 1141.
[34] LEVER A.B.P., *Inorganic Electronic Spectroscopy*; Elsevier, Amsterdam, 1986.
[35] REEDIJK J., VAN LEEUWEN P.W.N.M., GROENEVELD W.L., Recl. Trav. Chim. Pays Bas, 87 (1968), 129.
[36] LEVER J.A.B., Chem. Ed., 45 (1968), 711.
[37] KOKOSZKA G.F., GORDON G., Trans. Met. Chem., 5 (1969), 181.
[38] EL DISSOUKY A., REFAAT L.S., Inorg. Chim. Acta, 87 (1984), 213.
[39] FIGGIS B.N., LEVIS J., Prog. Inorg. Chem., 6 (1964) 37.
[40] SMART J.S., *Effective Field Theories of Magnetism*, Saunders W. B. Comp., Philadelphia, 1966, p. 24.

Received 28 September 2010

Contents

GUIDELINES FOR AUTHORS

Manuscripts can be sent by conventional mail or by e-mail. Submission of a manuscript to *Materials Science-Poland* implies that it is not being considered for the publication elsewhere, and the authors have a necessary authorization to publish the material contained in the paper. **The manuscripts should conform to the formal standards of the Journal which may be found in the first issue of each volume and on the web page.**

Authors are encouraged to submit electronic versions of the manuscript by e-mail, to the address of the Journal. A single PDF file should be sent, containing text, references, figures, tables etc. Alternatively, the authors can submit the manuscript by conventional mail, sending a CD with the PDF file mentioned above, to the Editor-in-Chief at his address given below.

Each submitted manuscript will be reviewed, the final decision concerning its acceptance resting with the editors. Upon acceptance, the corresponding author will be requested to submit the following material (via e-mail or by conventional mail, on CD)

- A DOC or RTF file containing the final version of the text, references, tables and figure captions. The content of the file should be identical with that of the hard copy, and should exactly match the version seen and accepted be the referee(s).
- File(s) in appropriate formats containing figures. The required formats of the drawings (plots, schemes of technological processes) must be vector files such as XLS, OPJ, cdr (Excel, Origin, CorelDraw) which may also be exported as EPS, EMF or WMF files. Drawings submitted in tiff or jpg formats (bitmaps, raster graphics), even if exported as EPS, EMF or WMF files, will not be accepted. **Bitmaps are acceptable only in the case of photographs**. The photographs (only in grayscale) should have the resolution not lower than 300 dpi (estimated for the size in which they are expected to be reproduced).
- A PDF file containing the complete manuscript (text, literature, tables, figures, etc). The file should be carefully checked as it will serve as a hard copy in case of doubts. **The contents of the PDF file should exactly match the material in other files.**

Irrespective of whether the final version is submitted by e-mail or by conventional mail, the authors should also send **via conventional mail** a signed copy of the Copyright Transfer Agreement (available on the web page of the Journal).

For detailed information consult the first issue of each volume or the web page of the Journal.

The mail should be addressed to:

Professor Juliusz Sworakowski
Editor-in-Chief, Materials Science-Poland
Politechnika Wrocławska, W-3
Wybrzeże Wyspiańskiego 27
50-370 Wrocław, Poland

Electronic correspondence should be sent to: MatSci@pwr.wroc.pl
Web page of Materials Science-Poland: www.MaterialsScience.pwr.wroc.pl

The Publisher reserves the right to make necessary alterations to the text. Each corresponding author will be supplied with one free copy of the journal. Orders for additional offprints can be placed with the Publisher.